

UNCLASSIFIED

AD NUMBER

AD908924

LIMITATION CHANGES

TO:

Approved for public release; distribution is unlimited.

FROM:

Distribution authorized to U.S. Gov't. agencies only; Test and Evaluation; JAN 1973. Other requests shall be referred to Air Force Avionics Laboratory, Attn: Wright-Patterson AFB, OH 45433.

AUTHORITY

AFWAL Itr, 9 May 1980

THIS PAGE IS UNCLASSIFIED

THIS REPORT HAS BEEN DELIMITED
AND CLEARED FOR PUBLIC RELEASE
UNDER DOD DIRECTIVE 5200.20 AND
NO RESTRICTIONS ARE IMPOSED UPON
ITS USE AND DISCLOSURE.

DISTRIBUTION STATEMENT A

APPROVED FOR PUBLIC RELEASE;
DISTRIBUTION UNLIMITED.

7
AFAL-TR-73-21

AD908924

ACQUISITION AND TRACKING PERFORMANCE EVALUATION

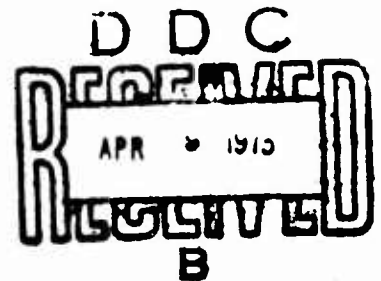
Final Report

C. E. McClellan, G. R. Chippendale, R. C. Ohlmann
Lockheed Missiles & Space Company, Inc.

R. O. Waddoups, L. G. Horn, G. R. Hostetter
ITT Gilfillan

Lockheed Missiles & Space Company, Inc.
Research and Development Division

Technical Report AFAL-TR-73-21
MARCH 1973



Distribution is limited to U. S. Government agencies only,
by reason of inclusion of test and evaluation data; applied
January 1973. Other requests for this document must be
referred to AFAL/TEL, Wright-Patterson AFB, Ohio, 45433.

Air Force Avionics Laboratory
Air Force Systems Command
Wright-Patterson Air Force Base, Ohio

NOTICE

When Government drawings, specifications, or other data are used for any purpose other than in connection with a definitely related Government procurement operation, the United States Government thereby incurs no responsibility nor any obligation whatsoever; and the fact that the government may have formulated, furnished, or in any way supplied the said drawings, specifications, or other data, is not to be regarded by implication or otherwise as in any manner licensing the holder or any other person or corporation, or conveying any rights or permission to manufacture, use, or sell any patented invention that may in any way be related thereto.

Copies of this report should not be returned unless return is required by security considerations, contractual obligations, or notice on a specific document.

ACQUISITION AND TRACKING PERFORMANCE EVALUATION

Final Report

C. E. McClellan, G. R. Chippendale, R. C. Ohlmann
Lockheed Missiles & Space Company, Inc.

R. O. Waddoups, L. G. Horn, G. R. Hostetter
ITT Gilfillan

Lockheed Missiles & Space Company, Inc.
Research and Development Division

Distribution is limited to U. S. Government agencies only,
by reason of inclusion of test and evaluation data; applied
January 1973. Other requests for this document must be
referred to AFAL/TEL, Wright-Patterson AFB, Ohio, 45433.

FOREWORD

This Final Technical Report (Lockheed Report LMSC-D313251) on "Acquisition and Tracking Performance Evaluation" describes and summarizes the results obtained in the performance of Air Force Contract F33615-72-C-1941. This evaluation was performed for the Avionics Laboratory Wright-Patterson Air Force Base, Ohio, by Lockheed Missiles & Space Company, Inc. (LMSC), Palo Alto Research Laboratory, Palo Alto, California, with the assistance of subcontractor ITT Gilfillan, San Fernando, California. The work was performed from May 1972 to December 1972. Captain Thomas W. W. Hewlett, Jr. (AFAL/TEL) was the Project Engineer for the Avionics Laboratory. The work was supported by the Advanced Development Program 405B.

Except for analytical work performed at ITT Gilfillan, the work was performed by both LMSC and ITTG personnel in the LMSC Palo Alto Communications Sciences Laboratory, headed by Dr. R. C. Ohlmann. The equipment used in the evaluation was supplied by LMSC and ITTG from prior Independent Research programs at the two companies. The project leaders were C. E. McClellan for LMSC and Dr. R. O. Waddoups for ITTG. Other principal contributors to the evaluation were G. R. Chippendale, D. S. Oppenheimer, and Dr. A. F. Sklensky of LMSC and W. D. Burch, J. C. Dillman, L. G. Horn, and G. R. Hostetter of ITTG.

The report was submitted in January 1973 and has been reviewed and is approved for publication.



PAUL M. FREEDMAN, MAJ USAF
Program Manager
405B Advanced Development Program

ABSTRACT

The significance of this research and development to the Air Force is that the performance evaluation has provided major benefits for ensuring the capability to perform acquisition and tracking for satellite laser communication. The evaluation revealed some subsystems in which improvements were required or desirable and other subsystems in which tolerances could be relaxed or requirements reduced. Convenient hardware configurations and operating techniques were devised. The results of the acquisition and tracking performance evaluation provide a base of information and experience upon which an operational system can be developed with increased reliability and minimum cost.

Experimental evaluation has been made of tracking and pointing performance of an optical communication system employing a separate laser for each of these functions. The optical beam diameters were scaled down to 7/8 in. from larger diameters which would be employed for an operational space communication system. The tracking system and pointing laser were mounted on an oscillating table in simulation of vehicle limit cycle motion. Experimental results confirmed theoretical predictions of performance and demonstrated the feasibility of tracking and pointing laser beams with accuracy suitable for practical communication systems in space.

TABLE OF CONTENTS

Section		Page
I	INTRODUCTION	1
II	SUMMARY	3
	1. General Considerations	3
	2. Measurement Results	5
	a. Acquisition	5
	b. Tracking Accuracy as Function of Signal-to-Noise Ratio	5
	c. Tracker AGC Sensitivity	6
	d. Image Size Effects	6
	e. Mirror Control Loops	6
	f. Pointing Accuracy	7
	g. Gimbal Friction and Bearing Inertia	7
	h. Effects of Vehicle Motion	8
	i. Mapping of Image Dissector Photocathode Sensitivity	8
	j. Air Turbulence Effects	8
III	DESCRIPTION OF EQUIPMENT AND TEST FACILITIES	9
	1. Background	9
	2. Facilities	9
	a. Laboratory	9
	b. Air-Cushioned Optical Table	9
	c. Rate-Table	12
	3. Beacon and Pointing Detector Terminal	12
	a. Optical Bench	12
	b. Beacon Laser	16
	c. Beam-Expander	16
	d. Beam-Splitter	16
	e. Pointing Focusing Lens	16
	f. Pointing Detector	16
	g. Calibration Wedges	17

Section	Page
4. Tracking Terminal	22
a. Gimballed Mirror	22
b. Telescope	22
c. Fine-Steering Mirrors	22
d. Beam-Splitter	29
e. Image Dissector and Tracker Circuit	29
f. Optical Attenuators	36
g. Pointing Laser	36
h. Boresighting	37
i. Point-Ahead	40
j. Gimbal Servo	40
k. Test Instrumentation	46
IV EVALUATION TESTS	47
1. Acquisition, Fine Tracking Subsystem - Test 1	47
a. Test Objectives	47
b. Results	47
c. Comparison With Theory	49
2. Tracking Accuracy as Function of Signal-to-Noise Ratio - Test 2	49
a. Test Objective	49
b. Test Program	49
c. Test Configurations and Plan	50
d. Results	52
3. Tracker AGC Sensitivity	55
a. Laboratory Tests	55
b. Results and Comparison With Predicted Performance	58
4. Image Size Effects on Tracking Accuracy	58
a. Test Objectives	58
b. Test Methods	58
c. Test Data	61
d. Results and Conclusions	64

Section		Page
	5. Mirror Control Loops	68
	a. Fast Steering Mirror Control Loop Frequency Response	68
	b. Fast Steering Mirror Control Loop Transient Response	68
	c. Gimballed Mirror Response, Stability and Effect on Tracking - Test 5.3	71
	6. Pointing Accuracy, Boresighting and Point-Ahead - Test 6	77
	a. Discussion of Error Sources	77
	b. Noise Spectra	82
	c. Pointing Accuracy Measurement	82
	d. Boresighting	91
	e. Point-Ahead	91
	7. Gimbal Inertia and Bearing Friction	93
	a. Tests Conducted	93
	b. Static Tracking Accuracy	93
	c. Dynamic Tracking Accuracy	93
	d. Effect of Bearing Friction	95
	e. Effect of Mirror Inertia	96
	f. Effect of Servo Amplifier Gain	96
	g. Influence of the Gimbal Loop on Tracking Error	96
	8. Effects of Vehicle Motion	98
	9. Image Dissector Photocathode Sensitivity Mapping - Test 9	98
	a. Mapping Program	98
	b. Results	100
	10. Atmospheric Turbulence Effects	100
V	CONCLUSIONS, ERROR ANALYSIS, AND SCALING FACTORS	106
	1. Conclusions	106
	2. Error Analysis	106
	3. Scaling Factors	108
VI	COMMENTS AND RECOMMENDATIONS	109
	1. General Comments	109
	2. Recommendations	110

Section	Page
Appendix ANALYSIS	113
1. Goals	113
2. Tracker Performance	113
a. Error Detector	114
b. Noise Density	119
c. Tracking Control Loop Response	121
d. AGC and Aperture Size Corrections	125
e. Tracking Efficiency	131
3. Beam Steering System Performance and Noise	137
a. System Performance	137
b. Noise	140
4. System Errors - Magnetic Fields	146
5. System Errors - Photocathode Granularity and Photocathode Ageing	146
REFERENCES	149

LIST OF ILLUSTRATIONS

Figure		Page
1	Acquisition and Tracking Evaluation Subsystem – Planned Construction	10
2	Equipment as Actually Assembled (Tubes Shielding Light Beam From Air Turbulence Removed for Greater Clarity)	11
3	Vehicle Limit Cycle and Rate Simulator	13
4	Beacon Terminal Configuration	14
5	Beacon Terminal	15
6	Measurement of Pointing Angle With Crossed Roof Prisms and a Quadrant Detector	18
7	Pointing Detector Circuits	19
8	Deviation of Optical Beam Passing Through a Thin Optical Wedge	20
9	Wedge Deviation Data From Diffraction Optics	21
10	Turntable Layout – Tracking Terminal	23
11	Acquisition and Tracking Terminal	24
12	Gimballed Mirror	25
13	Beamsteerer Open-Loop Response	27
14	Fine Steering Gimballed Mirrors	28
15	Image Dissector Tracker – Block Diagram	31
16	Optics and Sensor of Image Dissector	33
17	Video From a Conical Scan of an Image in a Square Aperture	34
18	Fine Acquisition Tracking and Pointing – Optical Components	38
19	Boresighting Method	39
20	Fine Steering and Gimbal Loops	41
21	AGC Circuit Performance Evaluation – Block Diagram	56
22	AGC Dynamic Range	57
23	AGC Frequency Response	59
24	Measurement of Spot Diameter Using Image Dissector Aperture	60

Figure		Page
25	Variation of Image Size With Beam Diameter	62
26	Tracking Noise as a Function of Iris Diameter	65
27	Spot Size as a Function of Iris Diameter	67
28	Frequency Response of Fast-Steering Mirrors	69
29	Mirror Response to Square Wave Input (50 Hz)	70
30	Mirror Response to Square Wave Input (20 Hz)	70
31	Component Relationship in Tracking Mode	73
32	Frequency Response of Torquer Driver Circuit Used With Full Inertia Mirror Assembly	74
33	Closed Loop Gimballed Mirror Frequency Response With Full Inertia Mirror Assembly	75
34	Accelerometer Output Voltage During Table Reversal	76
35	Pointing and Tracking Errors and Torque Motor Current With Table Rotation and 0.3 oz.-in.-sec ² Inertia	78
36	Pointing and Tracking Errors in an Expanded Time Scale	79
37	Effect on Pointing Due to External Disturbances - No Tracking Operation	81
38	Pointing Noise Spectrums	83
39	Tracking Noise Spectrum	84
40	Tracking and Pointing Errors With All Mirrors and Table Off - Signal Current of 1.8×10^{-5} A	86
41	Tracking and Pointing Signals With Gimballed Mirror and Table Motionless and With Fast Tracking Mirror First Off and Then On - Anode Current 1.8×10^{-5} A	87
42	Pointing and Tracking Signals With All Systems Operational - Signal Current of 1.1×10^{-5} A at ID Anode	88
43	Pointing and Tracking Errors and Gimballed Mirror Current With Full Inertia, Weight, and Gain	89
44	Pointing and Tracking Signals With Table Not Running But With Fine Steering and Gimballed Mirrors Operating	99
45	Map of Photocathode Response as a Function of Spot Position	101
46	Pointing and Tracking Detector Outputs With Generated Atmospheric Turbulence	102
47	Power Spectra of Tracker Horizontal Output With High-Frequency Turbulence (Heat and Air)	103
48	Power Spectrum of Pointing Detector Output With Beam Steerers Off and On (Vertical and Horizontal Scales are Logarithmic)	105

Figure		Page
49	Block Diagram for Tracker Performance	113
50	Tracking Error Generation	116
51	Model for Error Signal Generator	116
52	Tracking Loop Block Diagram	122
53	AGC Block Diagram	126
54	Noise Error as a Function of Background Power	130
55	Velocity Error as a Function of Background Power	130
56	Noise Error as a Function of AGC Threshold	132
57	Velocity Error as a Function of AGC Threshold	132
58	Error Signal as a Function of Position Error	134
59	Correction Factor for Received Optical Power	135
60	Relative P_{rms} Versus Ratio at Various Background Light Illumination Levels	136
61	Beam Steerer Loop	137
62	Bode Plot of Steering Loop	139
63	Steering Loop Response	139
64	Block Diagram of the Tracking Loops	141
65	Beam Steerer Response	143
66	Block Diagram for Transfer Function of O/I_2	143
67	Bode Plot of Transfer Functions of Elements	145
68	Bode Plot of Transfer Functions of O/I_2	145

LIST OF TABLES

Table		Page
1	Noise Components in Pointing and Tracking	4
2	Comparison of Measured Pointing Errors With Expected Error	5
3	Wedge Deviation Data (Microradians)	17
4	Average Time Required to Acquire	48
5	Results of Acquisition Probability Measurements	48
6	Signal and Noise Measurements Data – Test 2.1	51
7	Image Dissector Sensitivity Calibration	52
8	Tracking Error Measurement Data	53
9	Theoretical and Measured Tracking Error	54
10	AGC Dynamic Range	55
11	Image Dissector Sensitivity Calibration	61
12	Tracking Error Signal as Function of Beam Diameter	63
13	Signal-to-Noise Ratios for Various Beam Diameters	63
14	Measured Image Spot Sizes	64
15	Transient Response of Fast Steering Mirrors	71
16	Summary of RMS Pointing and Tracking Errors	90
17	Gimbal Inertia, Bearing Friction, and Gain Effects	94
18	Summary of Effects of Friction, Inertia, and Servo Gain	95
19	Extrapolated Friction Error – Final System Configuration	97
20	Effects of Vehicle Motion	98
21	Comparison of Measured Pointing Errors With Expected Error	107
22	Component Parameters	112
23	Anode Noise Level	120

Section I

INTRODUCTION

A design study for a Space Data Relay Subsystem was previously conducted by LMSC and a Final Report, SAMSO TR-272 (Ref. 1), was submitted. This study included the design of the acquisition, tracking, and pointing components to be used with laser communication systems between satellites and between satellites and ground or aircraft.

The work reported herein was performed for the purpose of experimental evaluation of some of the critical concepts put forth in the design study. The acquisition and tracking performance evaluation was conducted by means of a tracking and pointing test system which had been assembled jointly by LMSC and ITTG through their Independent Research programs. The optics were smaller, by a factor of seven, than those previously planned for a communication system. Thus appropriate scaling was required to convert evaluation data to communication system performance expectations. The equipment largely simulated the tracking and pointing functions of the two terminals of an operating laser communication system. There was a tracking detector, a tracking system, and a pointing laser at one terminal, and a laser beacon and a pointing detector at the other terminal. Both terminals were mounted on a single air-supported slab of concrete to provide high relative stability of the two terminals, to isolate them from ground motions, and to permit precision control of their angular relationship.

The objectives of the proposed program were as follows:

- Demonstrate that state-of-the-art components and techniques could suitably point a narrow optical beam under conditions simulating typical path losses, backgrounds, and vehicle motion
- Determine, by experimental test, evaluation, and theoretical analysis, the performance of the design concept and suitable techniques for further optimization of performance
- Recommend to the Air Force the development effort required to obtain a complete acquisition, tracking, and pointing subsystem that will meet the requirements of the Space Data Relay Subsystem

The tests conducted included the following:

- Tests of signal and noise combinations at various power levels
- Automatic Gain Control
- Image size variations

- Scanning mirror friction and inertia
- Vehicle motions
- Minimum and maximum slew rates as defined in the SDRS study

The performance evaluation has provided major benefits for ensuring the capability to perform acquisition and tracking for satellite laser communication. The evaluation revealed some subsystems in which improvements were required or desirable and other subsystems in which tolerances could be relaxed or requirements reduced. Convenient hardware configurations and operating techniques were devised. The results of the acquisition and tracking performance evaluation provide a base of information and experience upon which an operational system can be developed with increased reliability and minimum cost.

In the report following is first a summary of the tests and their results, followed by a description of the equipment and the testing after which are given the detailed write-ups for the various tests. At the end is a discussion of conversion factors and errors and recommendations for further directions of effort.

Section II

SUMMARY

1. GENERAL CONSIDERATIONS

An acquisition, tracking and pointing system was evaluated to determine its capabilities. The functions available were those essential to the determination of performance in the areas listed above. The acquisition function began at the stage where the tracker image dissector automatically searched for, acquired, and tracked a beacon source which was illuminating the tracker aperture. The tracker was mounted on an oscillating turn-table which simulated the limit-cycle oscillation of a space vehicle.

Tracking and pointing performance were measured as functions of a number of parameters as well as the best performance being determined. The results of all of the measurements provided information from which the performance of a larger operational type optical communication system was estimated.

The key measurements made were of tracking and pointing, but these need to be defined in order to properly assess their significance. Tracking error was measured as the output of the image dissector angular error detector in the frequency band below 300 Hz, the response band of the fine steering mirrors. The noise above 300 Hz was almost entirely shot-noise and therefore would not, if measured, truly represent any error in tracking. On the other hand shot-noise or any other noise below 300 Hz was largely tracked out by the fine steering mirrors which utilized the output of the image dissector as their driving error signal. Consequently, it was possible for the fine steering mirrors to be inaccurately positioned, to compensate for noise, and yet for the tracking error signal to be small or even much smaller than the mirror error. There was no way to determine, in the tracker, how much of the mirror motion was true tracking motion and how much compensation for noise.

The measurement of pointing accuracy became the crucial data. Pointing accuracy was defined as the output of a pointing detector which measured the direction of arrival of the pointing laser with respect to an arbitrary reference axis fixed with respect to the beacon laser. This measurement was also made in a bandwidth below 300 Hz. The error measured was a relatively true measure of pointing error since the pointing detector noise contributed negligible error. Pointing error contained all errors originating in either the tracking or the pointing functions. It was the vital measure of performance since it included the contributions of tracker sources, which, if not for pointing requirements, could be much larger.

Table 1 identifies the noise components in tracking and pointing. Some were measured in the course of the evaluation; some were observable but not measurable; and others could not be detected with the available sensitivity and resolution. Table 2 gives the values of the important pointing errors that were measured.

Table 1. Noise Components in Pointing and Tracking

Configuration	I. D. (Tracking) Output	Pointing Detector
Image Dissector -- Tracking Beam Steerers -- Off	Beacon laser noise Atmospheric turbulence noise Mechanical vibration noise Shot noise at image dissector Electrical pick-up Spurious light on image dissector	Pointing laser noise Atmospheric turbulence noise Mechanical vibration noise Shot noise at pointing detector Electrical pick-up Spurious light on detector
Image Dissector -- Tracking Beam Steerers -- On	<u>Components Above 300 Hz</u> Beacon laser noise Atmospheric turbulence noise Mechanical vibration noise Shot-noise at image dissector Electrical pick-up Spurious light on image dissector Fine steering mirror position transducer noise Beam steerer friction noise Gimbal friction noise <u>Components Below 300 Hz</u> Same as above but greatly attenuated by action of the beam-steerers moving so as to null the I. D. output in this frequency range, i. e., the bandwidth of the beam-steerers	<u>All Components:</u> Pointing laser noise Atmospheric turbulence noise (to extent not tracked out) Mechanical vibration noise Shot noise at pointing detector Electrical pick-up Spurious light on pointing detector Fine steering mirror position transducer noise Beam steerer friction noise Gimbal friction noise Boresight error <u>Plus Under -300-Hz Components of Following:</u> Beacon laser noise Mechanical vibration noise in tracker Shot noise in image dissector Electrical pick-up in tracker Spurious light on tracking detector

Table 2. Comparison of Measured Pointing Errors
With Expected Error (Gimbal Axis Only)

Pointing Error Component	Expected Errors	
	SDRS Final Report (Microradians)	Scaled To 7/8 In. (Microradians)
Shot-Noise At Image Dissector	0.2	1.37
All Other Sources	0.2	0.2
Total (RSS)	0.28	1.38
Measured Error	—	1.8

NOTES: Measured with fast steering and table in operation. Pointing error measured in the horizontal plane only, that of the turntable motion. Shot-noise at the image dissector has been scaled inversely proportional to beam diameter. Pointing error components from all other sources have been taken at the same total value as in design study. This results in an excessive requirement for the demonstration since one would expect less incidental error with an optimally designed tracking and pointing system than with the more casual breadboard employed in the demonstration.

2. MEASUREMENT RESULTS

The results of the various measurements are summarized below in terms of several aspects.

a. Acquisition

Fine gimbal automatic acquisition took place speedily and dependably. Since there was no automatic coarse acquisition, the image dissector acquisition field of view was greater than for a space system and the acquisition time was proportionately longer. During initial testing, spurious images formed by multiple reflections in the optics caused false acquisitions. These problems either were solved or would be eliminated in an operational quality optical system.

b. Tracking Accuracy as Function of Signal-to-Noise Ratio

Tracking accuracy, measured as the error output of the image dissector below 300 Hz, should be less than 1 microradian. A value of 0.8 microradian rms was measured when noise sources were reduced to the minimum possible. The residual value was found to be due primarily to the inherent noise in the electronic position pickups on the fine steering mirrors. This led to the consideration of a much quieter technique to be used in the future. Meanwhile, tracking measurements were made with this noise as an ever-present background. Even with such noise, the measured horizontal axis tracking error with the turntable running and a 0-dB margin S/N ratio was only

1.45 microradians rms with optimum adjustments. This compares with a goal of 1.37 microradians rms. The 1.45 is about 1/20 of the 28 microradian beamwidth expected for the 7/8-in. diameter beam. At higher signal-to-noise ratios the tracking error became smaller, as predicted by theory.

c. Tracker AGC Sensitivity

Tracker AGC sensitivity was measured by inputting a modulated signal of variable amplitude to the AGC circuits and measuring the error signal generated. The AGC held the output constant to a fraction of 1 percent over an input amplitude range of 189 to 1, starting from a signal slightly smaller than the lowest signal anticipated in an operational system. The frequency response of the AGC was measured and was flat at low frequencies, allowed 0.7 of the modulating voltage through at 70 Hz, and had no effect beyond 100 Hz. This response was about 30 Hz narrower than had been planned but was satisfactory in performance.

d. Image Size Effects

It had been planned to obtain tracking data of sufficient accuracy and over a wide enough range of beam diameters, i.e., 1/2 in. to 1-3/4 in., that a reasonable extrapolation could be made to estimate the performance of a 6-in. diameter beam. Although data were obtained, a number of factors combined to limit the accuracy and hence the possibility of such great extrapolation. With the smaller diameter beams there was insufficient power to operate the AGC in its flat range. In calculating the expected noise, a correction had to be made for the fact that the falling off of gain with the small beams and signals resulted in a reduction of bandwidth. At the larger diameters, the energy density in the beam fell off so rapidly with diameter that the calculation of spot size from measured diameter was in significant error. Consequently the data points closest together in the center of the range—1/2 inch and 1 inch—were the most significant. They did not, however, have sufficient accuracy to permit extrapolation to 6 in. Nevertheless, greater beamwidths gave smaller errors. In the center of the range of diameters where accuracy was the best, the agreement between the measured and calculated noise was best, with a difference of about 30 percent, probably within the limited accuracy of the measurement.

e. Mirror Control Loops

The closed loop frequency response of the fine steering mirrors was found to be 270 Hz for vertical and 350 Hz for horizontal. Both values are within acceptable limits from the design intention of 300 Hz at the 3-dB down points. Transient responses to step inputs were measured and found to have less than 5-percent overshoot and a damping ratio of 0.7. These are indicative of a stable system. The closed frequency response of the gimballed mirror was taken and found to peak at 25 Hz and to be 3 dB down at 50 Hz for a typical gain setting. These values are higher than planned, and it is apparent that a lower bandwidth could be used although the effect on performance would be very slight since the fast steering mirrors correct for noise in the mirror gimbal loop.

Tracking accuracy during reversals of the turntable had been a matter of concern and speculation. However, even though the rate table produced acceleration peaks on the order of 100 times that of a typical space vehicle, the peaks rose only about 1 micro-radian at reversal. This additional error might as likely be due to mechanical disturbance of the components as to the dynamics of the tracking system in this test configuration. Fortunately, when scaled down to an appropriate acceleration value, the error introduced would be so small that determination of the chief cause is unimportant.

f. Pointing Accuracy

It was found early in the tests that the pointing system was extremely sensitive to mechanical disturbances, and, on occasion, to acoustic disturbances, and was always highly sensitive to air turbulence. Considerable effort was taken to shield the optical paths reasonably well from air currents. There was no way to tell how much of the minimum pointing noise was due to residual air turbulence. The minimum pointing error was 1.1 microradians for horizontal and 0.9 microradians for vertical. This is the sum of all of the contributors to pointing error in a static condition. Table 1 indicates a listing of error factors. When tracking was implemented and the rate table put in operation, the horizontal error increased to 1.8 microradians rms. This was compared with the expected pointing error on one axis of 1.38 microradians rms. (See Table 2.)

This rms pointing error exceeds the expected value by 30 percent. Possibly the difference is accounted for by having taken all pointing error sources, except shot noise at the image dissector, at the same value as for the design study. Atmospheric turbulence and noise in the fast tracking loop were degrading the performance by undetermined amounts.

g. Gimbal Friction and Bearing Inertia

Friction effects were so small that it was not possible to get definitive data on them. The axial loading of the bearings was run at two different values - 39 oz and 13 oz. It was not possible to determine how the load was distributed between the two bearings. When the greater load was applied, the torque motor current to overcome friction was increased from 5 to 9 ma representing 0.006 oz-in. of friction torque. This was a change in the direction expected and a pleasingly small torque. An anomaly occurred in the tracking error, however, in that it became smaller with the heavier load. No certain explanation for this phenomenon has been found but, possibly, one of the bearings was initially too lightly loaded and was "loose" until the heavier load was applied. The change in tracking error was modest, reducing from 1.2 microradians rms to 1.0.

Two values of gimbal inertia were used. One was the nominal inner gimbal inertia of a communications package which is 0.3 oz-in.-sec². The other was made one tenth of this, a much more difficult case, but one designed to make errors visible that are not apparent with heavier gimbals. As expected the light gimbal had greater tracking error, increasing from 1.2 microradians rms on the horizontal axis to 1.6 microradians. The increase is not in as great a proportion as might be expected, but the total error contains errors from static sources adding up to 0.8 microradian rms so that the true increment is greater than the 1.6:1.2 ratio, being closer to 1.56:1. The significance of the inertia tests is to demonstrate that there is a tradeoff between weight and tracking error and that the preliminary design for the SDRS probably has sufficient inertia and does not need to be made heavier.

h. Effects of Vehicle Motion

Simulated vehicle motion at a rate just slightly less than anticipated vehicle motion caused a slight increase from 0.85 to 1.0 microradian rms in the measured horizontal tracking noise. Performance at lower speeds was observed, and a possible increase in tracking error due to a stick-slip model of friction was not detected. As noted earlier, the effects of possible vehicle acceleration were measured to be negligible.

i. Mapping of Image Dissector Photocathode Sensitivity

The sensitivity of the photocathode was measured by tracking a spot which was scanned across the image dissector in a raster scan. The intensity of the signal was constantly monitored as an indication of the surface sensitivity. The sensitivity is flattest in the central portion of the photosurface where it is most important. Even so, variations of up to 35 percent in distances that are not large compared with the diameter of the image spot could have been contributors to the basic tracking noise. They probably were not, however, since this noise would be proportional to signal level and would be prominent at high signal levels where, in fact, the S/N ratio became very large.

j. Air Turbulence Effects

It was noted early in the tests that the static (no fine steering) image dissector errors and the simultaneous pointing errors appeared very much alike as recorded on the strip chart. It was further noted that the static errors could be greatly reduced by shielding the light beams from air turbulence. When the fine steering mirrors were implemented, the tracking noise would virtually disappear, and the pointing noise would be reduced. Later experiments showed that if the pointing and tracking beams were adjusted to the same diameter and to similar spatial energy distribution, and were made reasonably colinear, then the tracker took out more of the turbulence noise in the pointing beam. Under special conditions as set up for tests on Contract F33615-72-C-1938 the tracking-out of turbulence noise in pointing was accomplished to a high degree.

Section III

DESCRIPTION OF EQUIPMENT AND TEST FACILITIES

1. BACKGROUND

The equipment tested in the Acquisition and Tracking Evaluation was provided by LMSC and ITT Gilfillan from work done on their Independent Research programs. The equipment provided the functions of beacon transmission, fine acquisition, tracking, and pointing. The optical beams were 7/8 in diameter, smaller by a factor of seven than a typical operating system. This required scaling certain expected performance errors by a factor of seven greater. The purpose of the research programs was to obtain data on acquisition, tracking, and pointing performance and to provide helpful information relative to the design of a full-scale system.

The initial design is shown in Figure 1. The final configuration of the working equipment is shown in a view from the other side in Figure 2 and conforms to the initial design except in minor details. A listing of the optical parameters is given on page 112.

2. FACILITIES

a. Laboratory

The laboratory had convenient control of ambient light levels and was convenient to a supply of optical parts and instruments and to electronic test equipment. Temperature control was by a conventional room thermostat located in the room. Due to turning off the building air conditioning on many evenings and on week-ends during the summer, the equipment was subject to thermal cycles of as large as 15°F. It is not believed that this had any significant effect on results since many components were not in high-precision mounts and were adjusted for each test run.

b. Air-Cushioned Optical Table

To provide a rigid and isolated table for mounting the equipment, a reinforced concrete slab 10 ft x 3 ft by 10 in. thick was made. This was floated on four partially inflated inner tubes resting on masonry piers. (See Figure 2.) The table provided noticeable isolation from floor vibrations. Damping was provided by the friction in the inner tubes which was sufficient to hold ringing to a few cycles upon receipt of an impulse. Flexure mode bending of the table was not of sufficient amplitude to be observed during tests. For the accuracies being sought, this construction proved to be entirely satisfactory. However, the slightest jar to the table while operating the system resulted in observable errors in pointing.

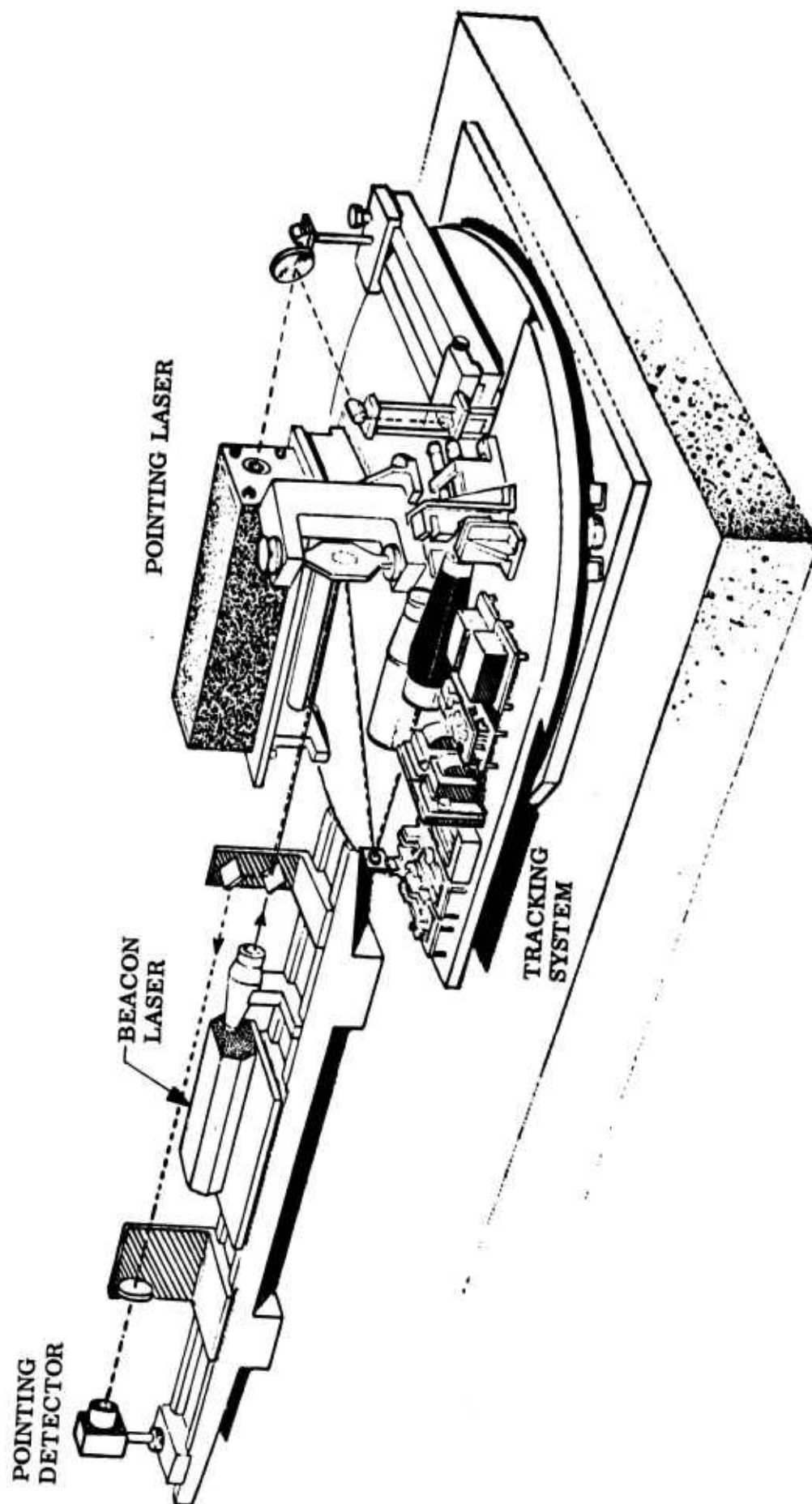


Figure 1 Acquisition and Tracking Evaluation Subsystem - Planned Construction

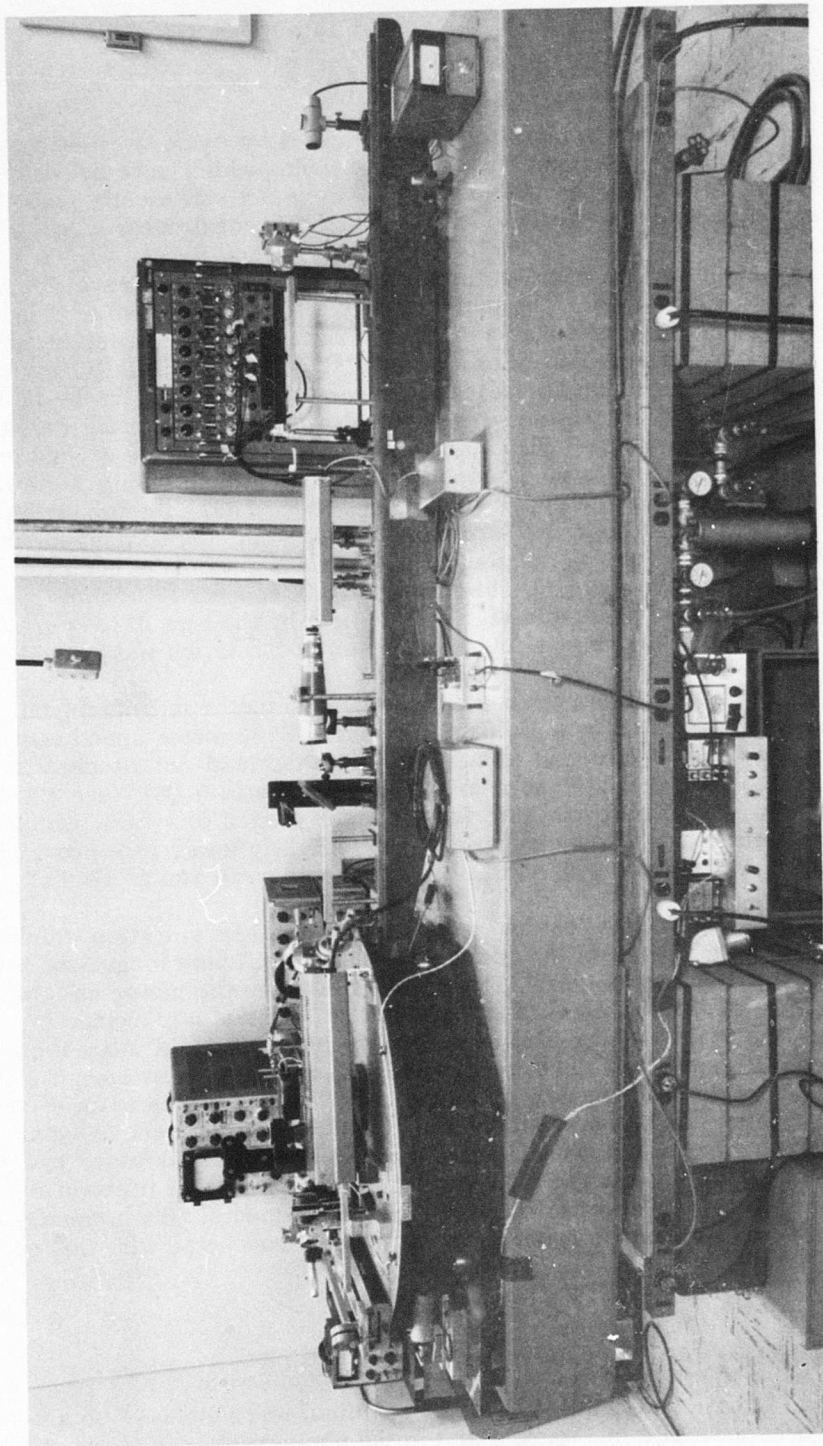


Figure 2 Equipment as Actually Assembled (Tubes Shielding Light Beam From
Air Turbulence Removed for Greater Clarity)

c. Rate-Table

To provide mechanical motion in simulation of vehicle limit cycle oscillations, a limited range rate-table (Figure 3) was constructed. Rate tables which were available within LMSC either did not have the slow rates required, were not sufficiently smooth running, or were impractical to move to the Palo Alto Research Laboratories.

Inasmuch as limit cycle motion requires only a very small angular travel, it was possible to use a simple design approach. The table top was a 3-ft-diam. disc of 1-in. -thick aluminum tooling plate. The base was a slightly larger piece of similar material. The top rotated on three precision 1-in. -diam. chrome steel balls. Initially, standard ball-bearing 1-in. balls were used but they caused perceptible roughness in the table motion so precision balls made as gauge standards were obtained. The bearing races were 3/4-in. -square carbide tool tips. These are extremely hard and are ground to a very fine finish. Their surfaces were made coplanar by placing them on a granite surface plate, applying epoxy resin to the upper surface and then placing the top or bottom of the table upon the tool tips. Upon the hardening of the resin, the bearing surfaces of the carbide plates were in a precision plane. The table top was kept centered at the bottom by a Bendix flex-pivot bearing which provided an essentially smooth and frictionless pivot. Since the travel allowable was limited both by the size of the carbide plates and the nature of the pivot bearing, a mechanical stop for rotation was provided.

The rate-table drive system was powered by a d-c servo motor manufactured by Electrocraft. It was speed-controlled by a Motomatic series E500 motor speed control. The motor drove a gear-box which turned a fine worm with the lead-nut attached to the table top. The ratios were such that at 2500 rpm the table rate was $0.064^\circ/\text{sec}$ (1120 microradians/sec). The limit cycle rate for the inner gimbal of a LOS, which is 1,200 microradian/sec, max. Most tests were run at the slightly lower rate provided by the motor at 2500 rpm. Amplitude was adjustable, and tests were run at $\pm 7/8$ of a degree.

Normal imbalance in the drive motor rotor resulted in a slight vibration which was detectable in pointing measurements but not considered of sufficient magnitude to justify a search for a better balanced motor. The coupling between the motor and the table top had observable backlash and a slight flexibility so that, upon a step change in direction of table rotation, the table top was excited to vibrate in a rotational mode for several cycles of ringing. The peak acceleration produced by reversals was around 1 radian/sec² for a reversal with motor speeds of 2500 rpm. This compares to an operational value 0.01 radian/sec² maximum acceleration. An attempt was made to obtain this latter value but the motor would not run as slow as 25 rpm. In addition, it was found that the motor had a large speed transient during reversals so that it produced a greater peak acceleration than if the reversal in speed had been smooth. Since the system was able to track under these adverse conditions, tests were conducted with this configuration.

3. BEACON AND POINTING DETECTOR TERMINAL

a. Optical Bench

Components of the beacon and pointing detector terminal were mounted on a 2-m optical bench as shown schematically in Figure 4 and in the photograph of Figure 5. This provided a convenient means of mounting components in an adjustable manner. Sensitivity to

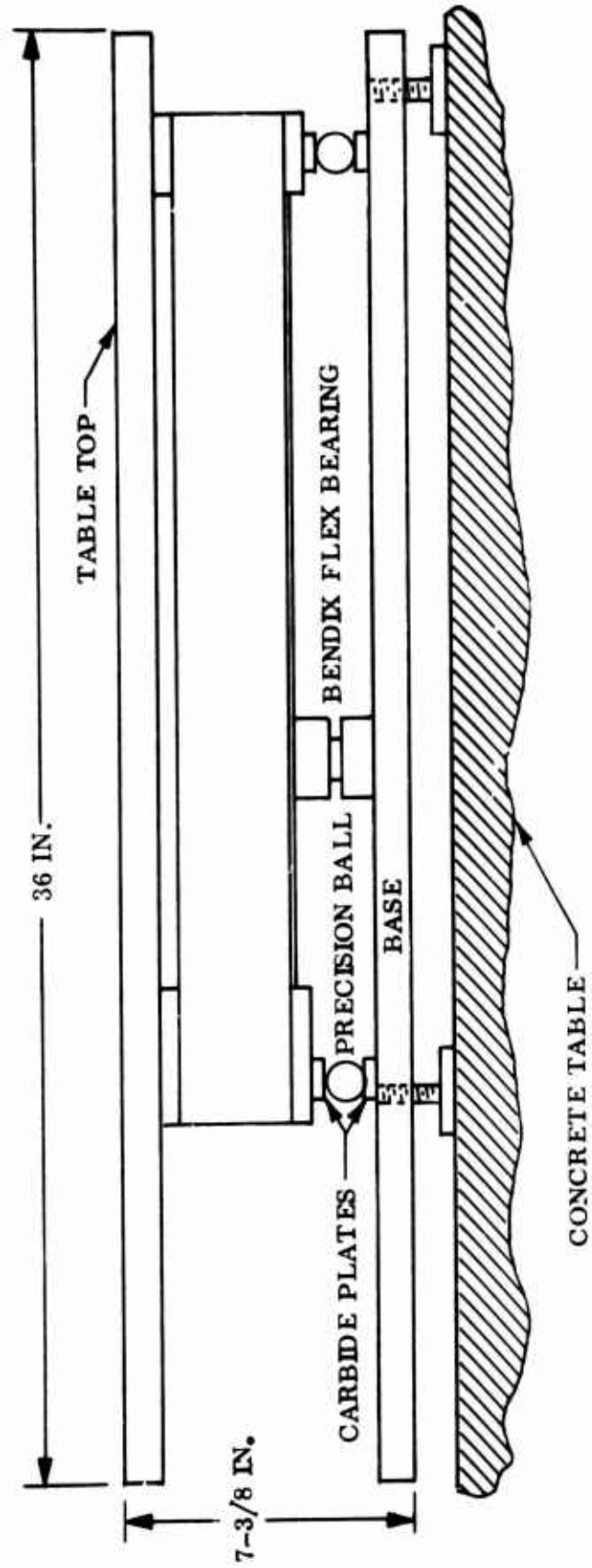


Figure 3 Vehicle Limit Cycle and Rate Simulator

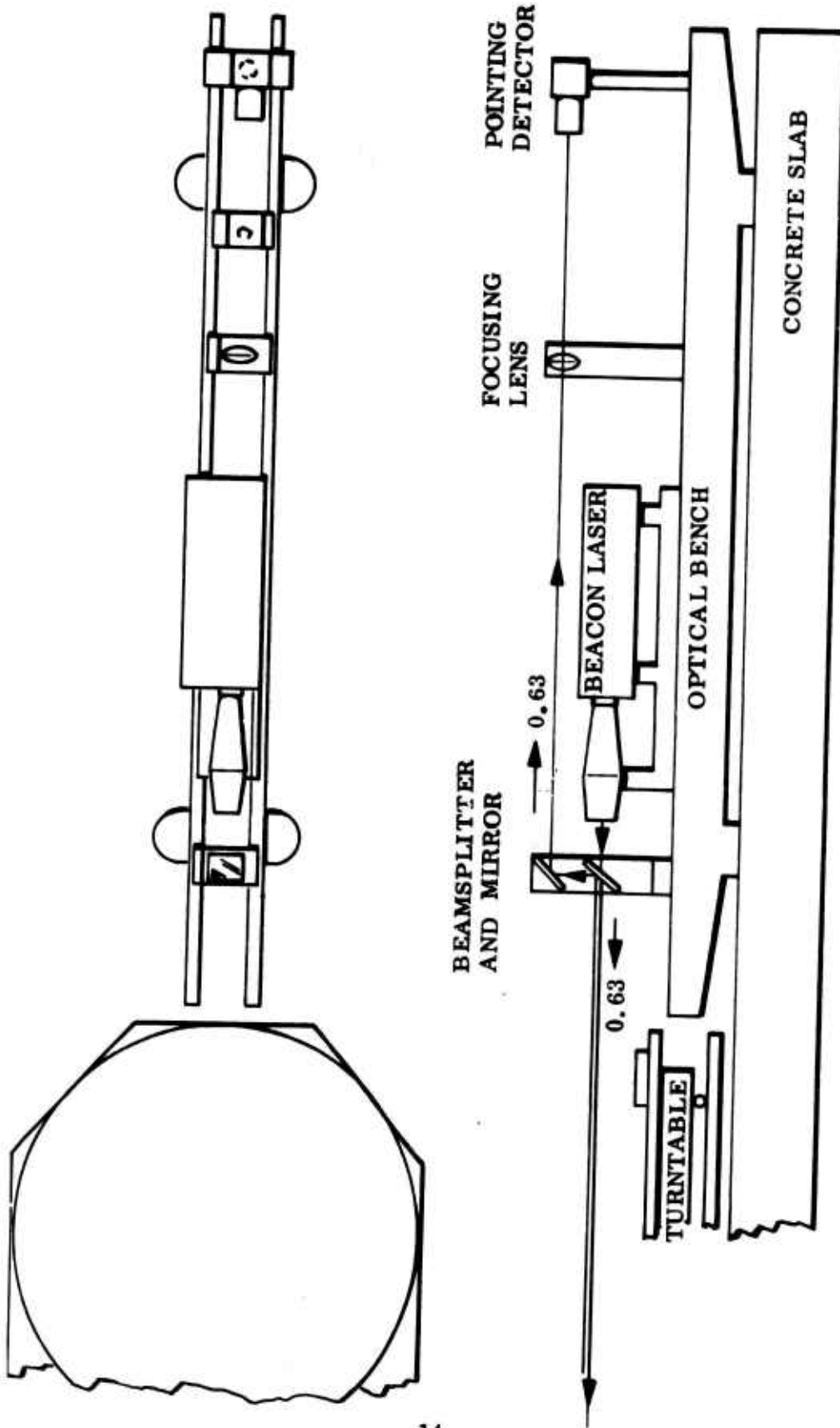


Figure 4 Beacon Terminal Configuration

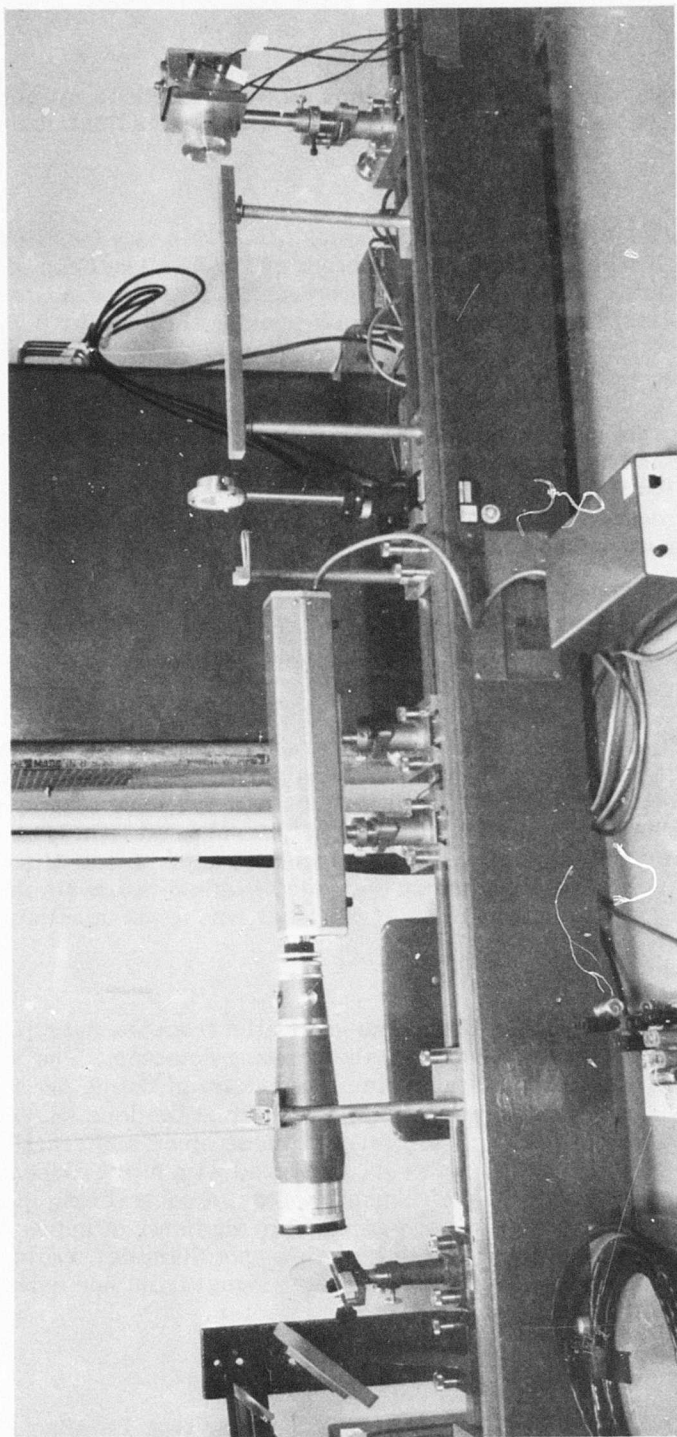


Figure 5 Beacon Terminal

hand forces was apparent when any of the mounts were touched. A more accurate test system would require more rigid, stable mounts with finer adjustments.

b. Beacon Laser

The beacon laser was a Spectra-Physics Model 133. This is a HeNe gas laser with a wavelength of 0.6328μ and a rated power output of 1 mW. The beam diameter is 0.8 mm at the $1/e^2$ points. The power through the spatial filter was measured at 0.5 mW near the end of the test program with 0.35 mW passing through the 0.87-in. aperture.

c. Beam-Expander

The beacon laser beam was expanded to nearly 2 in. in diameter by means of a Spectra-Physics spatial filter and beam-expander. The beam was expanded as a truncated gaussian beam so that the edges were less intense than the center. Since other optical components were restricted to a nominal 1-in. aperture, the beam was usually stopped down to 0.87-in. -diam. at the beam expander.

d. Beam-Splitter

A beam-splitter in front of the beam-expander served to separate the incoming pointing beam from the outgoing beacon beam.

This beam-splitter, and a similar one for separating the beacon from the pointing beam at the tracking terminal, was a Spectra-Physics partially reflecting precision mirror. Earlier, beam-splitting cubes were used, but these were found optically imperfect to the extent that diffraction limited spots could not be obtained, and both astigmatism and image distortion were present. These cubes had been used as substitutes for the initial beam-splitters, which were high quality dichroic beam-splitters for the separation of HeNe and argon laser beams, until the argon laser was found unsuitable.

e. Pointing Focusing Lens

After the incoming pointing laser beam was separated from the outgoing beacon beam, it was folded to a lens which focused it on the pointing detector. The lens was a simple thin lens, but quality was required to avoid astigmatism at the detector. The focal length used was 61 cms. The pointing beam diameter at the lens was about 10 mm. Precision determination of the spot size was not made since a diffraction-limited spot was not essential. The spot was, however, observed with a microscope and found to be free from coma and to be falling off smoothly from a central bright disc. For this beam a diffraction limited spot would have an angular diameter of approximately 126 microradians. For a 61-cm focal length lens this spot diameter would be 0.08 mm. This amount of motion would take the angle output signal from one extreme to the other and is the total operating range of the pointing detector.

f. Pointing Detector

The pointing detector was a United Detector Technology type PIN-Spot/4 silicon quadrant Schottky photodiode. The four detector elements are each 0.050 in. on a side with a 0.005 in. gap between the quadrants. The pointing detection system does not have direct comparison with the SDRS design since it takes the place of a second tracking detector.

In space, it is necessary to have tracking capabilities at both ends and, if the laser from either terminal should have a pointing error greater than 1/10 the beamwidth, tracking at the other terminal would be poor or difficult because little or no signal would be received. In the evaluation setup, due to the near-field intimate closeness of the two terminals, the pointing laser could be detected over pointing angles of many beamwidths.

The received energy was divided among the four detection diodes by a pair of thin roof-prisms, loaned by the Perkin-Elmer Corporation. These prisms have very fine corners, 1- μ in width, and the pair are placed at right angles, with their apexes crossing at the focal point of the lens. When the image is bisected by each apex, it is divided into four equal parts which diverge at equal angles from the focal point as shown in Figure 6. When they have diverged to 0.05 in. separation in both planes, a collimating lens then bends them into four parallel beams which fall upon the four quadrants of the photodetector. When the division of the beam is equal to all quadrants, they develop equal currents. However, as the spot moves on the prisms, the light goes more to some quadrants than to others, which produces unbalanced currents in the diodes. The outputs of the diodes were combined in a resistor network and are amplified by amplifiers as shown in Figure 7.

The prisms are mounted independently and each may have an error in orientation about the optical axis that will result in cross-talk between axes. The cross-talk is proportional to the sine of the angle of orientation error. This is estimated to be within $\pm 3^\circ$ so that the cross-talk would not exceed 5 percent.

g. Calibration Wedges

Calibration of the pointing and tracking detectors was accomplished by introducing precision glass wedges of known deviation into the beams in the collimated section (Figure 8). Available wedges had deviation of 4.8, 20.8, 41.7, and 60.3 microradians for 0.6328 μ m wavelength light from the HeNe laser. The smallest wedge (± 4.8 microradians) was used in calibrations since errors measured were seldom greater than 2 microradians although the 20.8 wedge was used as a check. The largest wedge was for point ahead, first in the tracking beam to set in a point-ahead angle of 60.3 microradians and then in the pointing beam to check that it had indeed been deviated 60.3 microradians from the beacon beam. A calibration of the deviation of the wedges was supplied by the vendor, as shown in Figure 9.

Table 3 presents the wedge deviation data shown in Figure 9 as converted to microradians from the measured wedge angle and index of refraction by the formula: deviation = wedge angle \times (n-1).

Table 3. Wedge Deviation Data (Microradians)

Wavelength (microradians):		Ref. 0.588	0.51	0.53	0.63
	Wedge ∞	n = 1.517	n = 1.52077	n = 1.51958	n = 1.51519
<u>Part No.</u>					
3275950-01	9.36	4.84	4.87	4.86	4.82
-02	40.5	20.9	21.1	21.03	20.8
-03	81.0	41.9	42.2	42.1	41.7
-04	117.0	60.5	60.9	60.8	60.3

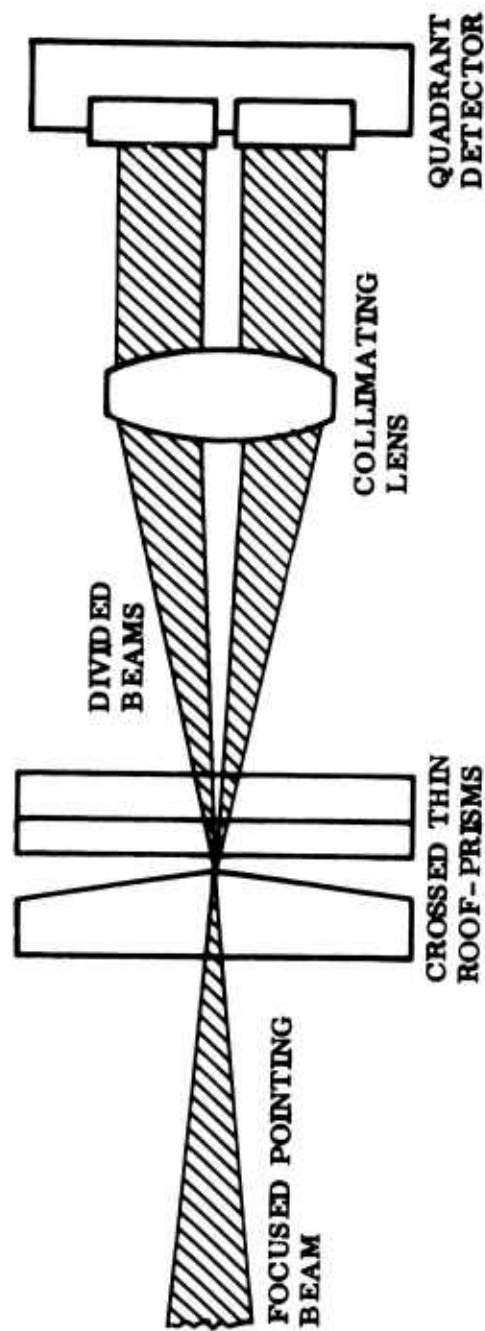
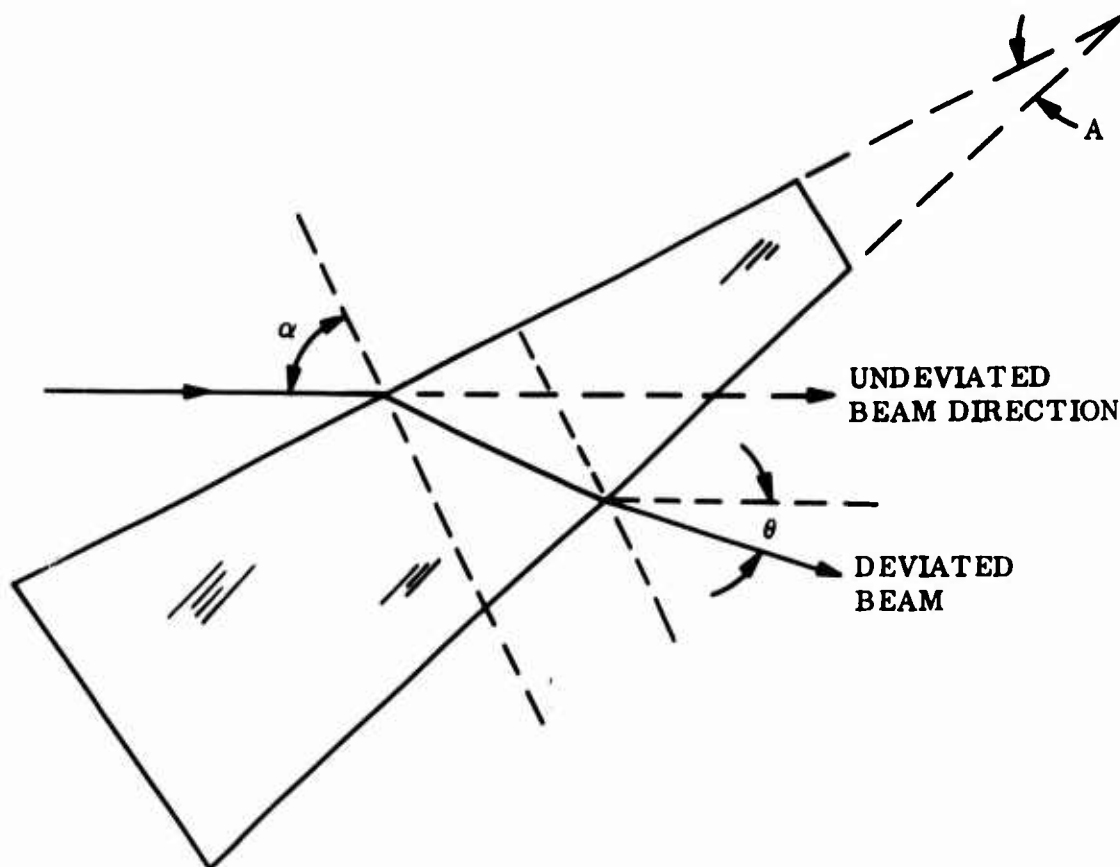


Figure 6 Measurement of Pointing Angle With Crossed Roof Prisms and a Quadrant Detector
 (As the focused beam moves with respect to ridges of roof-prisms, the fraction of the light falling on each quadrant of the detector varies accordingly; the spots of light on the detectors do not move but vary in intensity.)



θ = DEVIATION OF BEAM PASSING THROUGH A PRISM

n = INDEX OF REFRACTION OF PRISM MATERIAL

α = ANGLE OF INCIDENCE AT FIRST SURFACE

A = WEDGE ANGLE OF PRISM

FOR A THIN PRISM, THE DEVIATION IS GIVEN A SIMPLIFIED FORMULA:

$$\theta = (n - 1) A$$

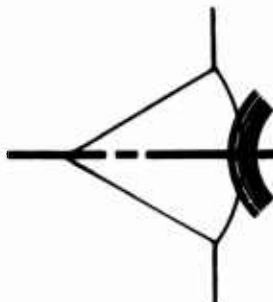
TO DETERMINE THE EFFECT OF THE ANGLE OF INCIDENCE, α , THE COMPLETE FORMULA WAS SOLVED:

$$\theta = \alpha - A - \sin^{-1} \left(n \sin \left\{ \left[\sin^{-1} \left(\frac{\sin \alpha}{n} \right) \right] - A \right\} \right)$$

IT WAS FOUND THAT THE ANGLE OF INCIDENCE ON THE WEDGE WAS UNIMPORTANT SINCE, FOR THE WEDGE GIVING A NOMINAL DEVIATION OF 4.8 MICRORADIANS, THE DIFFERENCE IN DEVIATION BETWEEN 0° INCIDENCE AND 45° INCIDENCE WAS LESS THAN 0.001 MICRORADIAN.

Figure 8 Deviation of Optical Beam Passing Through a Thin Optical Wedge

DIFFRACTION OPTICS



4035 TRANSPORT AVENUE • PALO ALTO, CALIFORNIA 94303 • PHONE (415) 327-5960

24/JULY, 1972

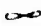
LOCKHEED MISSILE & SPACE CO.
3250 HANOVER WAY
PALO ALTO, CALIFORNIA 94303

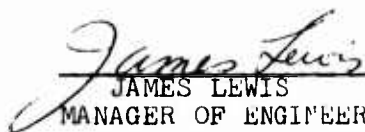
ATTN: C. McCLELLAN

SUBJECT: CERTIFICATION Re: OPTICAL WEDGES. ORDER NO. 9A99H0467A

THE FOLLOWING INFORMATION IS IN DIRECT SUPPORT FOR CERTIFICATION OF OPTICAL WEDGES, DWG. NO. 3275950-01, -02, -03 AND -04 FOR WEDGE DEVIATION AND REFRACTIVE INDICES FOR THE WAVE LENGTHS OF 5100, 5300 AND 6300 ANGSTROMS.

DEVIATION IN SECONDS

PART NO.	WEDGE 	n=1.517	n=1.52077	n=1.51958	n=1.51519
3275950-01	1.93"	1.00"	1.01"	1.00"	.99"
3275950-02	8.35"	4.32"	4.35"	4.34"	4.30"
3275950-03	16.70"	8.63"	8.70"	8.68"	8.60"
3275950-04	24.13"	12.48"	12.57"	12.54"	12.43"


JAMES LEWIS
MANAGER OF ENGINEERING

1-24-72

DATE

Figure 9 Wedge Deviation Data From Diffraction Optics

4. TRACKING TERMINAL

The tracking terminal, shown in Figures 10 and 11 comprised an image dissector tracking system, fine steering mirrors to augment the angular range of the image dissector and keep the image dissector error nulled, a single axis gimballed mirror to extend the tracking angular range capability in one plane, and a pointing laser to permit measurement of the accuracy with which a signal could be returned to the beacon terminal, using the incoming beacon signal as a pointing reference.

a. Gimballled Mirror

The gimbal pivoted a 2" diameter $1/10$ wavelength surface plane mirror. The bearings were Barden SR156SSW50-11 as specified for the inner gimbal of the package A1 of the SDRS preliminary design. They were mounted 6-1/2" apart as they would be in the above design. The assembly is shown in Figure 12. The basic inertia was smaller than the design inertia but with provision for adding mass to bring it up to 0.3 oz-in. - sec² as per the above design. This arrangement was made to permit running tests at two different inertia values. The gimbal was driven by a 6.0 oz-in. Aeroflex brushless torque motor. There were no readout provisions so that mechanical or manual positioning was required to place the gimbal in an initial acquisition position.

When mechanically positioned, acquisition and tracking were quickly attained. Manual initial positioning, due to the lack of steadiness in the human hand, and its flexibility, was sometimes difficult, though generally employed because of its convenience. In a system with servo command to the initial acquisition, this would not be a problem since it would approximate the mechanical positioning.

b. Telescope

The telescope for the tracker was a Spectra-Physics beam expander consisting of an expanding lens #334-L5 and a collimating lens #336. The power of the telescope was 11.3, which was as close as one could come to the SDRS value of 12 power, using off-the-shelf precision lenses. The telescope was mounted with its optical axis parallel to and 4 in. above the surface of the rate table. All other optical components on the table were mounted in this same plane. Threaded adjustments were provided for positioning of the telescope, and its construction included a focusing capability. The telescope had a 2-in. aperture, but it was not fully used due to aperture limitations by other components in the optical system.

c. Fine-Steering Mirrors

The fine-steering gimballed mirrors work together with the tracker and the coarse gimbal as a team. They are used to make small adjustments in the tracking direction. The coarse gimbal is incapable of rapidly making these adjustments because its response frequency is too low. The beamsteerers are provided with a signal from the tracker that indicates deviations from the desired pointing direction, and they rotate to null the deviations. The beamsteerer circuitry in turn provides inputs to the coarse gimbal to keep the beamsteerer positions in the approximate center of their range.

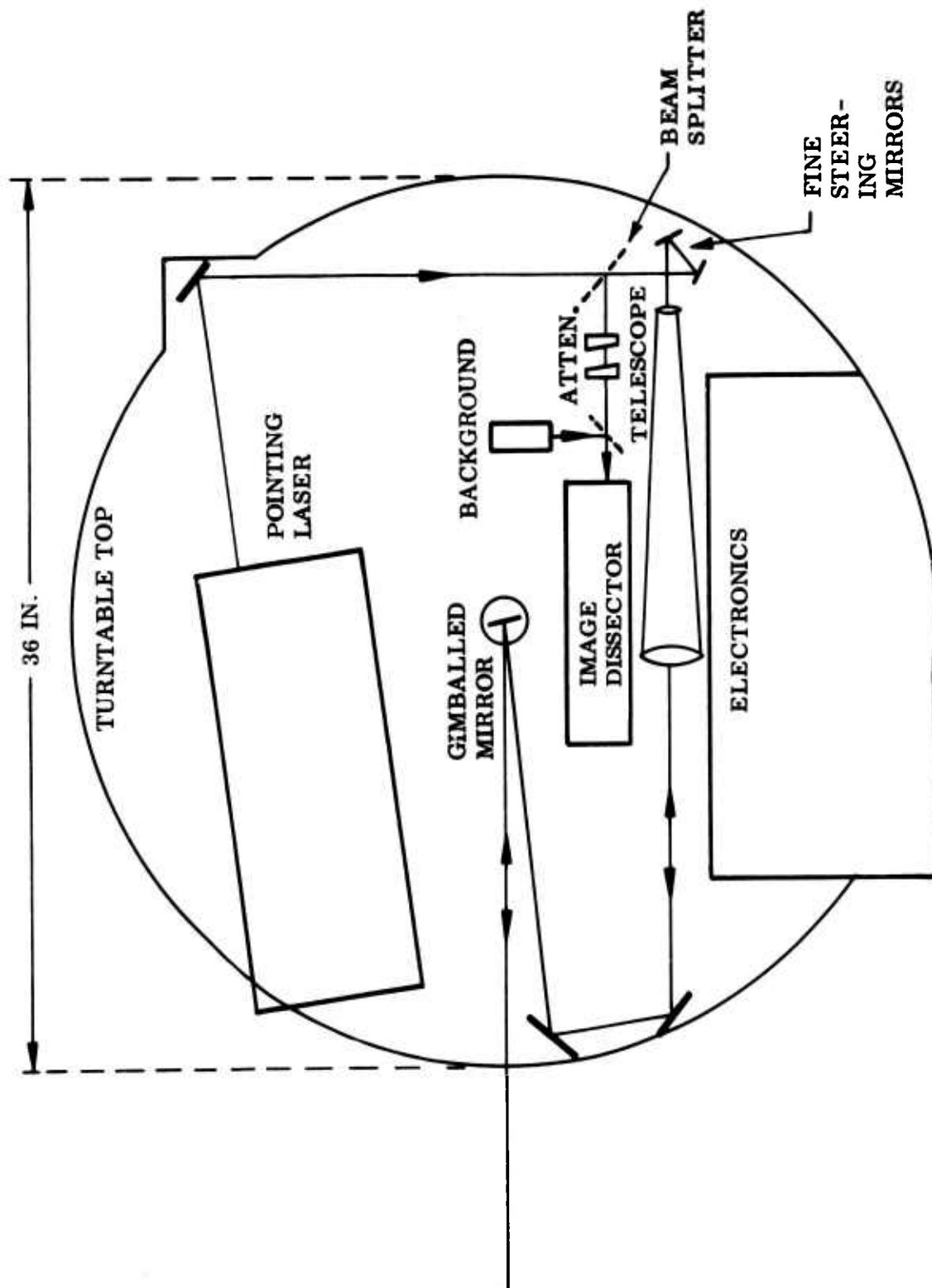


Figure 10 Turntable Layout - Tracking Terminal

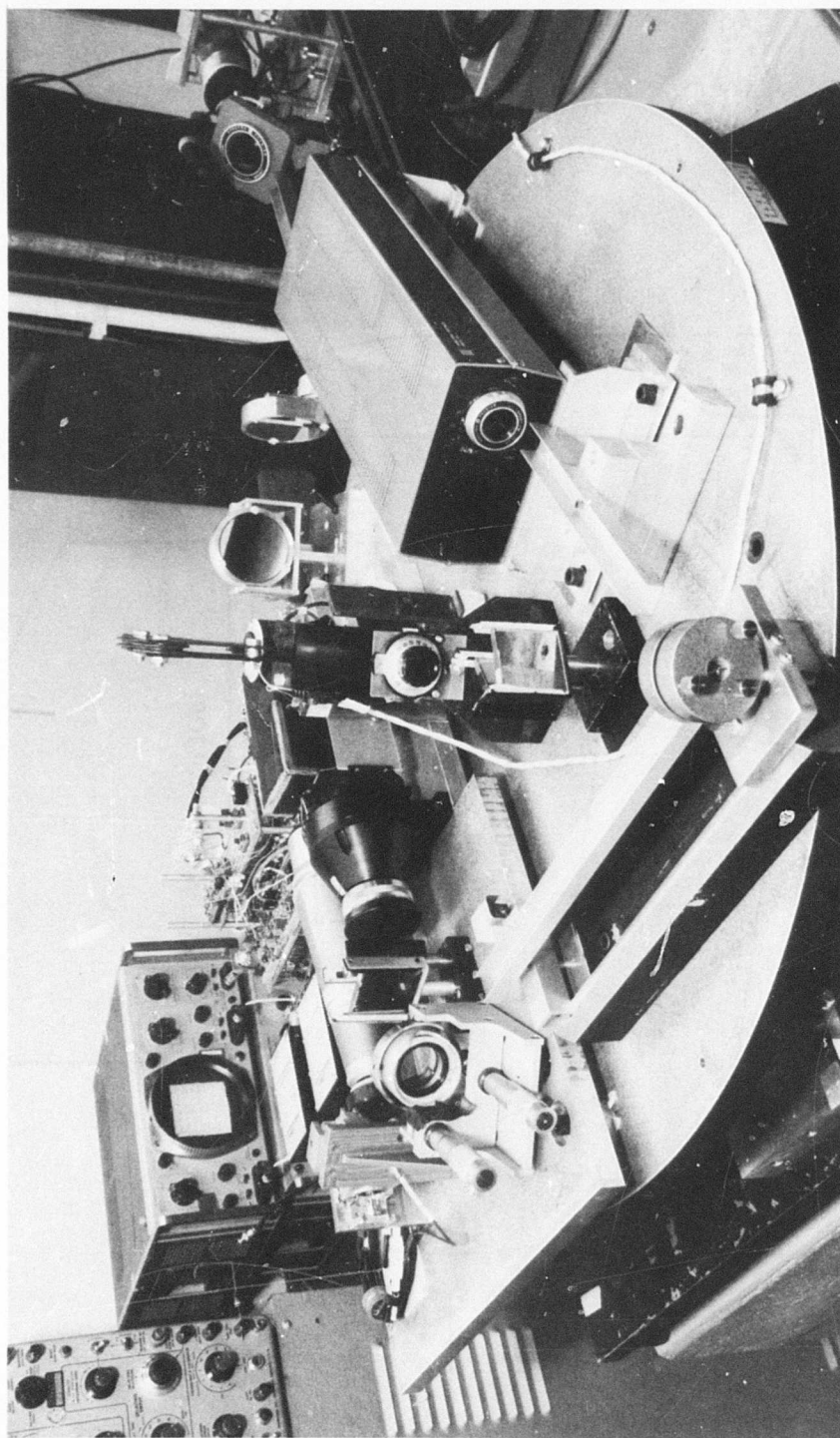


Figure 11 Acquisition and Tracking Terminal

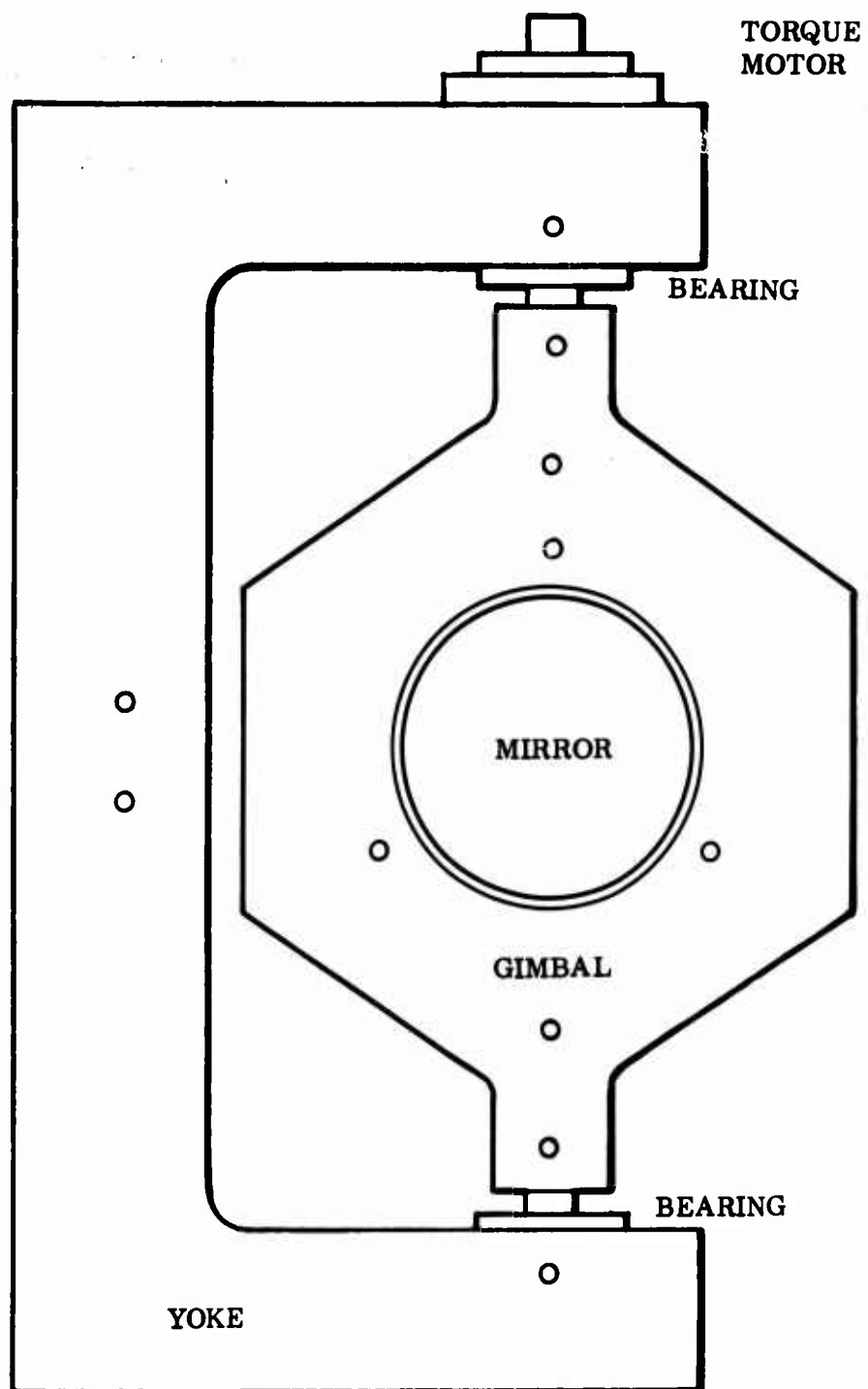


Figure 12 Gimballed Mirror

The fine beamsteering assembly consists of a mirror and torque motor mounted to the same shaft with a position pickoff mounted to the side. The shaft is supported on flexural pivots to allow limited rotation.

The beamsteerer mirror is 18 mm in diameter. The torquer is a brushless d-c motor, and the position pickoff is a coil bridge that detects eddy-current losses. Mirror movement is detected by the pickoff coil and leads to an accurate indication of beamsteerer angle. This information is used in the control loop for the beamsteerer and is also required to control the coarse pointing gimbaled mirror.

The beamsteerer's current response is described by the Laplace Transform,

$$B(s) = \theta/I = K_t [Js^2 + E]^{-1} \quad (\text{rad/A})$$

and the beamsteerer transfer function is

$$\theta/V_c = G_d K_t [Js^2 + E + G_t G_d K_t s]^{-1}$$

where

- K_t = motor torque constant
- G_d = torque driver gain (A/V)
- G_t = the differentiated position signal gain, (V/rad/sec)
- J = rotational inertia
- E = spring constant
- V_c = voltage at beamsteerer control input
- θ = mirror angle

Using a simplifying constant $C = G_d G_t K_t$ and plotting θ/V_c , the beamsteerer transfer function as a function of frequency is obtained as shown in Figure 13.

Referring to Figures 13 and 14 the control loop is a Type I velocity servo loop. The desirable characteristic of this system is that it nullifies position error in a closed-loop configuration. The integrator of the system is presently set to have a break, ω_1 at 0.07 Hz. At this point, it limits the tracker and beamsteering closed loop gain to 76 dB. To have a clean 6-dB/octave slope, the beamsteerer itself is stabilized by a velocity feedback loop. The gain of this feedback is set to minimize the effects of

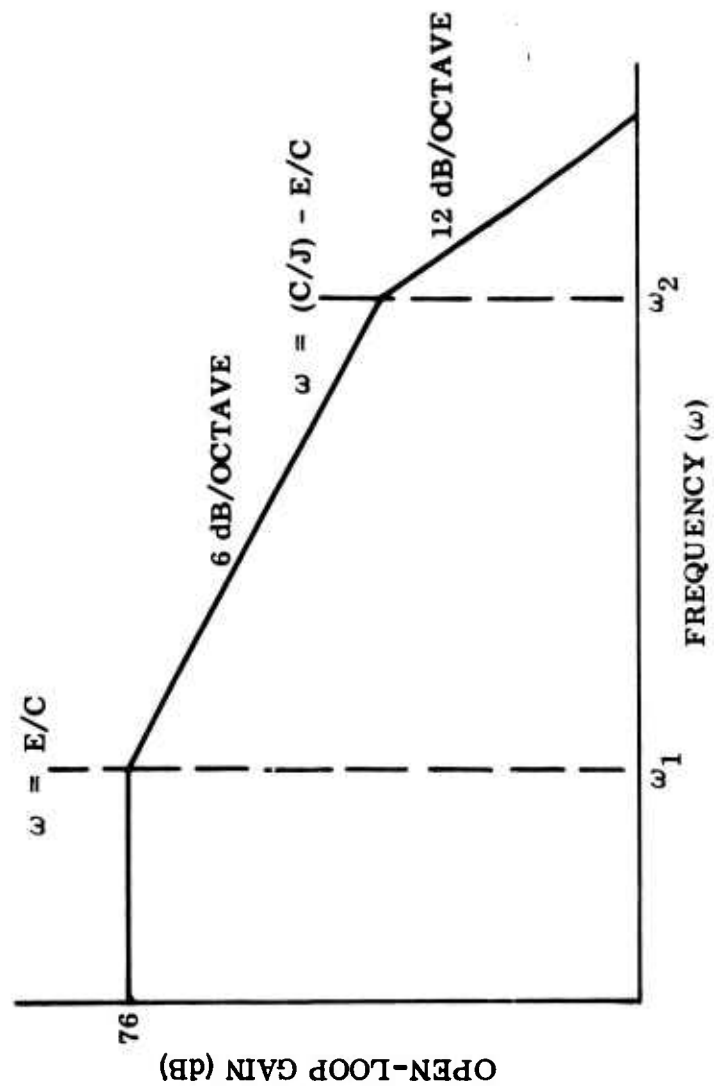


Figure 13 Beamsteerer Open-Loop Response

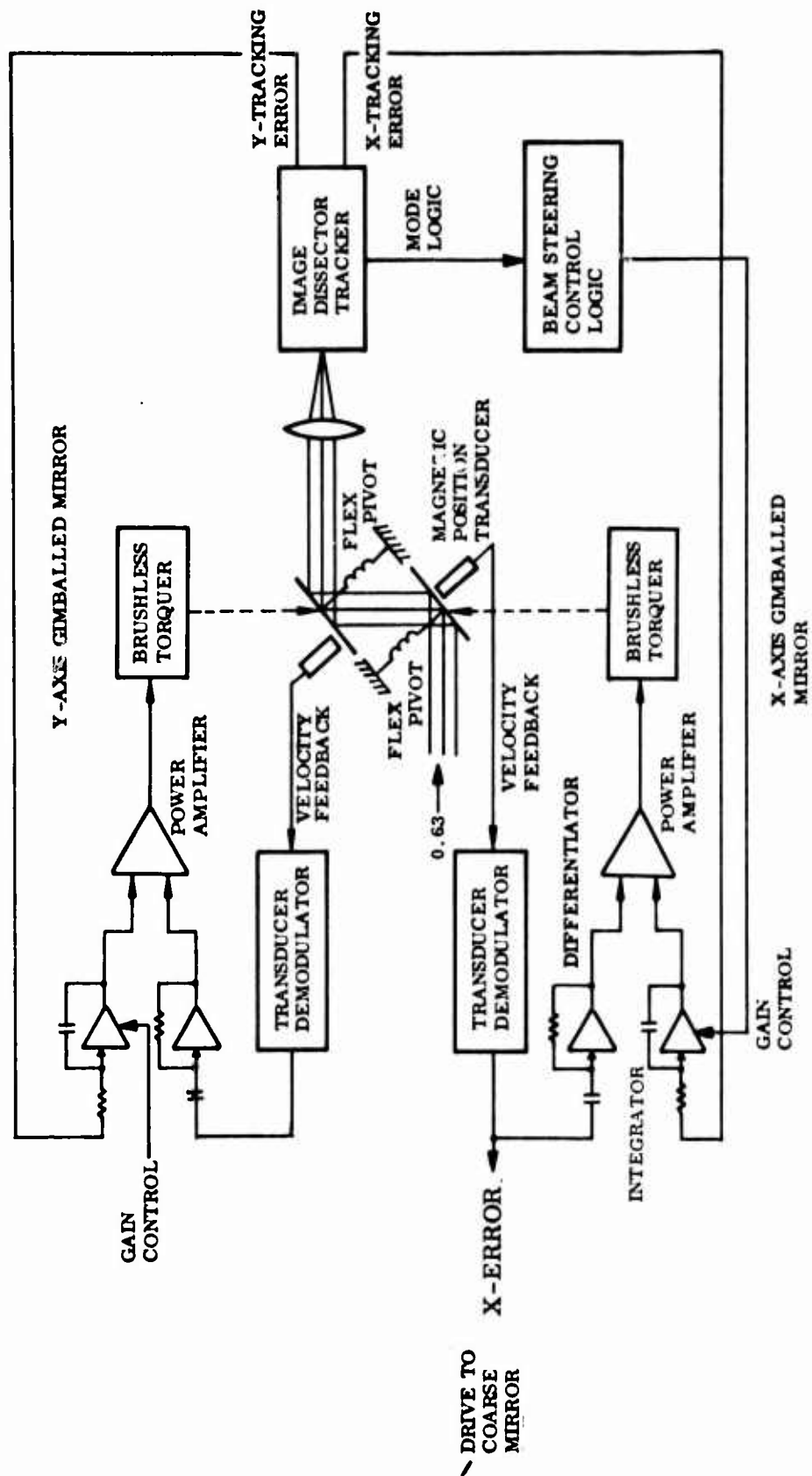


Figure 14 Fine Steering Gimballed Mirrors

the 40-Hz natural resonance of the inertia-flexpivot system. The tracker and beamsteerer loop has a bandwidth on the order of 300 Hz.

For successful operation of the tracker-beamsteerer loop, it must be able to handle the transient conditions of target acquisition and loss of target. This interfacing is accomplished by the mode control logic. Initially, the beamsteerers are inactive and held in a neutral position by the flexpivots. When the tracker has acquired a target, a large error signal is presented to the beamsteerer. At activation of the beamsteerer, therefore, the loop gain is reduced by 30 dB for 600 ms. This causes the speed of the beamsteerer to be limited while the target image is being centered on the face of the image dissector. If the speed were not limited, the large velocity commands could cause excessive rates at the tracker. A weak or faint target could, therefore, be lost, and reacquisition would be necessary.

In the event of the loss of target, the mode control is designed to minimize the reacquisition time. The most probable cause of loss of target is a momentary beam interruption lasting for ten's of milliseconds. The system's immediate response, therefore, is to hold the beamsteerers in their former position and to disconnect them momentarily from the tracker. The search scan within the tracker is also held disabled so that the tracker remains at its former position. If the interruption is momentary, the tracker regains its hold when the target reappears and the beamsteerers are reconnected. If, however, the target has not reappeared after 200 ms, the search scan of the tracker is enabled, and the beamsteerers are returned to their neutral position and remain disconnected from the tracker.

d. Beam-Splitter

A beam-splitter was employed to fold the received beacon beam into the image dissector and to pass the pointing laser beam in the outgoing direction. Initially, the beam-splitter was a dichroic type to reflect HeNe laser light and to transmit argon laser light. Ultimately, HeNe lasers were used in both directions so a cube-type beam-splitter was tried. Since it did not have sufficiently flat surfaces, however, astigmatism was introduced and, eventually, a flat semireflecting mirror was utilized instead. The beam-splitter was mounted in a two-axis adjustable Lansing mount to make possible adjustment of the angle of the beam entering the image dissector. However, because of the magnification of angle coming in through the telescope, the Lansing mount adjustment was too fine to be very convenient and had a corresponding limited range. It was then found possible, without too much difficulty, to perform horizontal alignment of the image dissector to the beacon beam by mechanical movement of the image dissector.

e. Image Dissector and Tracker Circuit

The tracker system simplified block diagram is presented in Figure 15. The operation of the tracking circuit comprises three steps. First, the system is in the acquisition mode, and the surface of the photocathode is electronically scanned. When a laser beam strikes the photocathode within the area of the scan, the second mode of operation begins. This second mode is a decision operation. If the system determines that there is no real target, then the circuit returns to the acquisition scan mode of

operation. However, if it is determined that there is a real target present, then the system goes into the third mode of operation, the track mode. If for some reason the target is "lost," then mode 1 operation begins again.

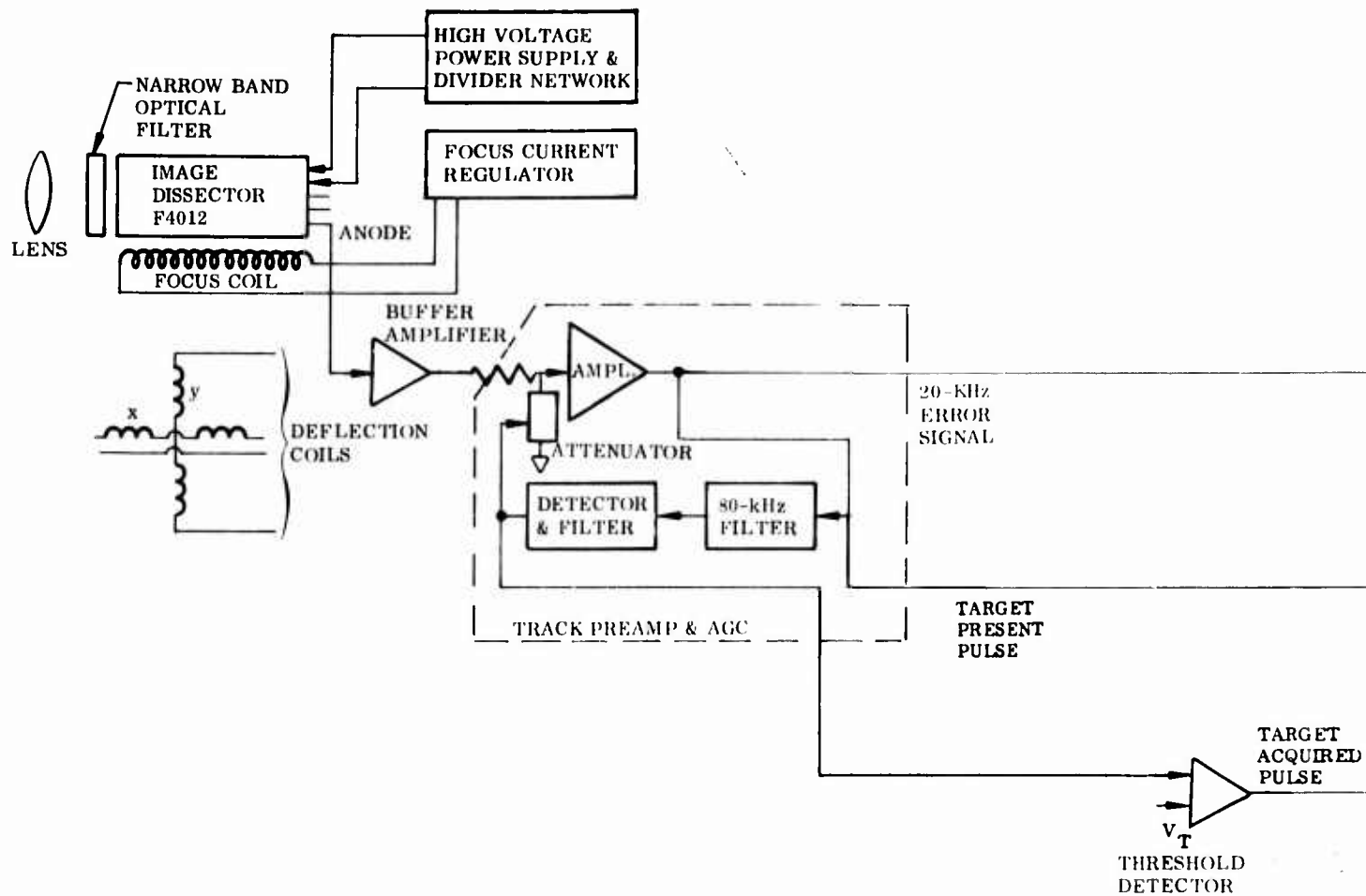
The heart of the tracker is the image dissector (ID) tube. Figure 16 shows a sketch of an ID with the image focused on the photocathode to form an electron image of the target. Behind the photocathode there is an aperture mask and secondary emission dynodes which amplify a signal 10^6 times. The image dissector is constructed so that when an accelerating voltage is applied between the photocathode and a mechanical limiting aperture, only those electrons leaving a specific area on the photocathode will pass through the limiting aperture. This area is called the instantaneous photocathode dimension (IPD).

When a small target image is positioned on the photocathode by the lens, a small stream of electrons is formed by the electron optics of an electromagnetic focusing field. A deflection coil positioned around the image section provides magnetic deflection of the target image electron beam. By applying proper deflection coil currents, the electron beam is swept back and forth across the limiting aperture, causing a modulation of the electron beam. The IPD, when projected through the optics, represents a region in space defined as the instantaneous field of view (IFOV). The region of space covered when scanning deflection currents are applied represents the total search or acquisition field of view (AFOV).

The ID tube search scan extends 3.9 by 5.2 milliradians. When the aperture is electronically positioned so as to receive the photoelectrons from the laser spot on the photocathode, there is a large pulse signal output from the ID, signaling the presence of the desired target. The target present circuitry responds to this pulse to change the scan from acquisition to track. The track scan is a circular nutation of the ID aperture at 20 kHz. The aperture is square, and, as it is scanned around the circular cross-section photoelectron beam, the anode current is increased as the beam passes through the corners of the square. This results in a 4th harmonic (80-kHz) component.

The 20-kHz signal is primarily a sine wave generated by driving the imaged spot around the periphery of the aperture. This sine wave, when demodulated, produces error voltages which, when added to the tube coil deflection current, causes the image to be centered on the aperture. As the image is centered, the 20-kHz sine wave approaches zero amplitude, and only the 80-kHz component due to the square aperture remains as a significant component. This output serves two purposes: to supply AGC control to the video amplifier and to provide a target indication voltage to maintain acquisition. Diagrams of these waveforms are shown in Figure 17 for the discrete conditions described above. Because of waveform complexities, no attempt has been made to diagram composite waveforms or transient conditions.

The first stage of the preamplifier is a broad band buffer amplifier (see Figure 15). The preamplifier output is amplified in a video amplifier which utilizes automatic gain control. FET attenuators and broadband amplifiers supply in excess of 20-dB controlled gain with a minimum phase change over the dynamic range. This portion of the circuit is labeled Track Preamp & AGC in the block diagram.



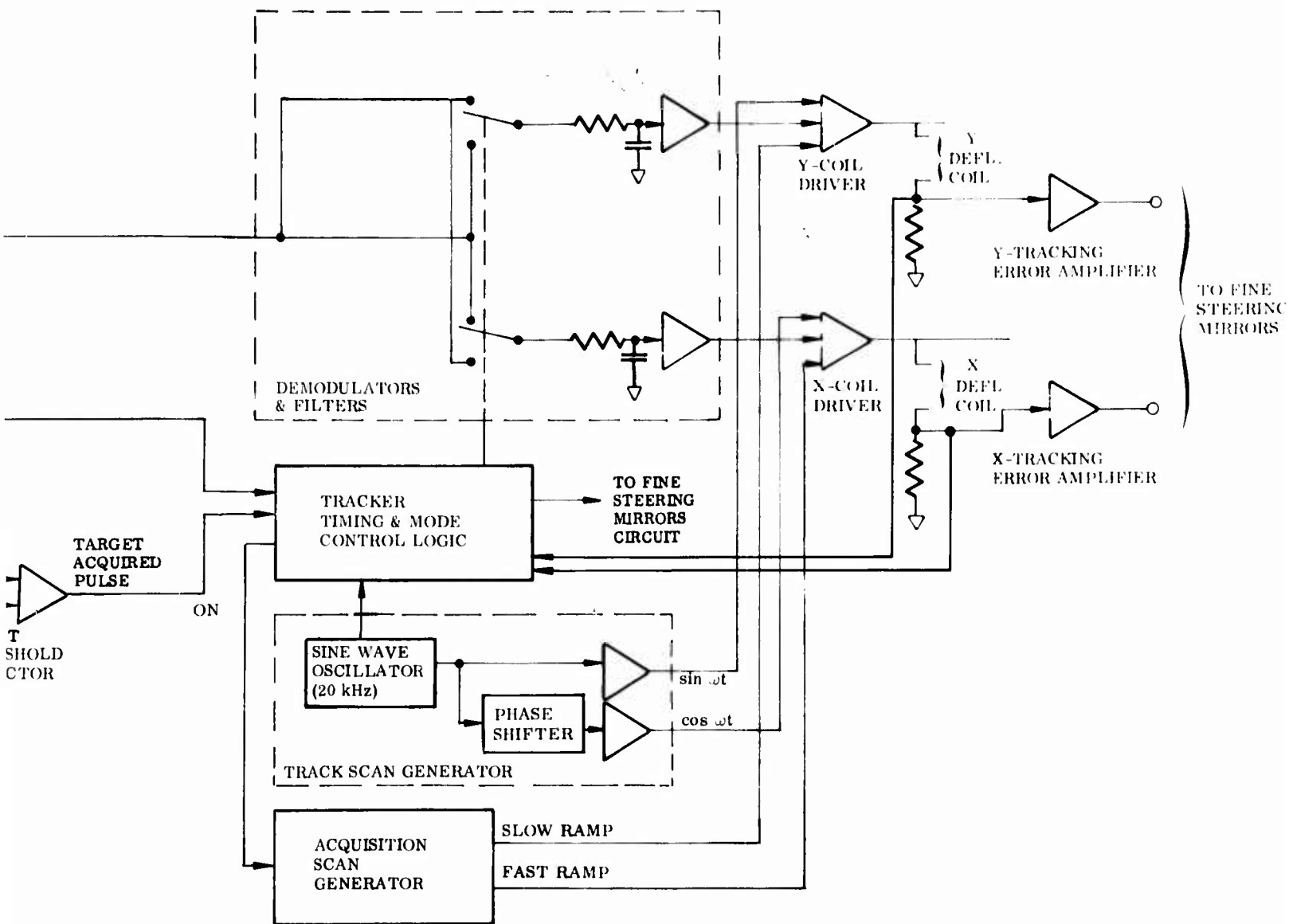


Figure 15 Image Dissector Tracker Block Diagram

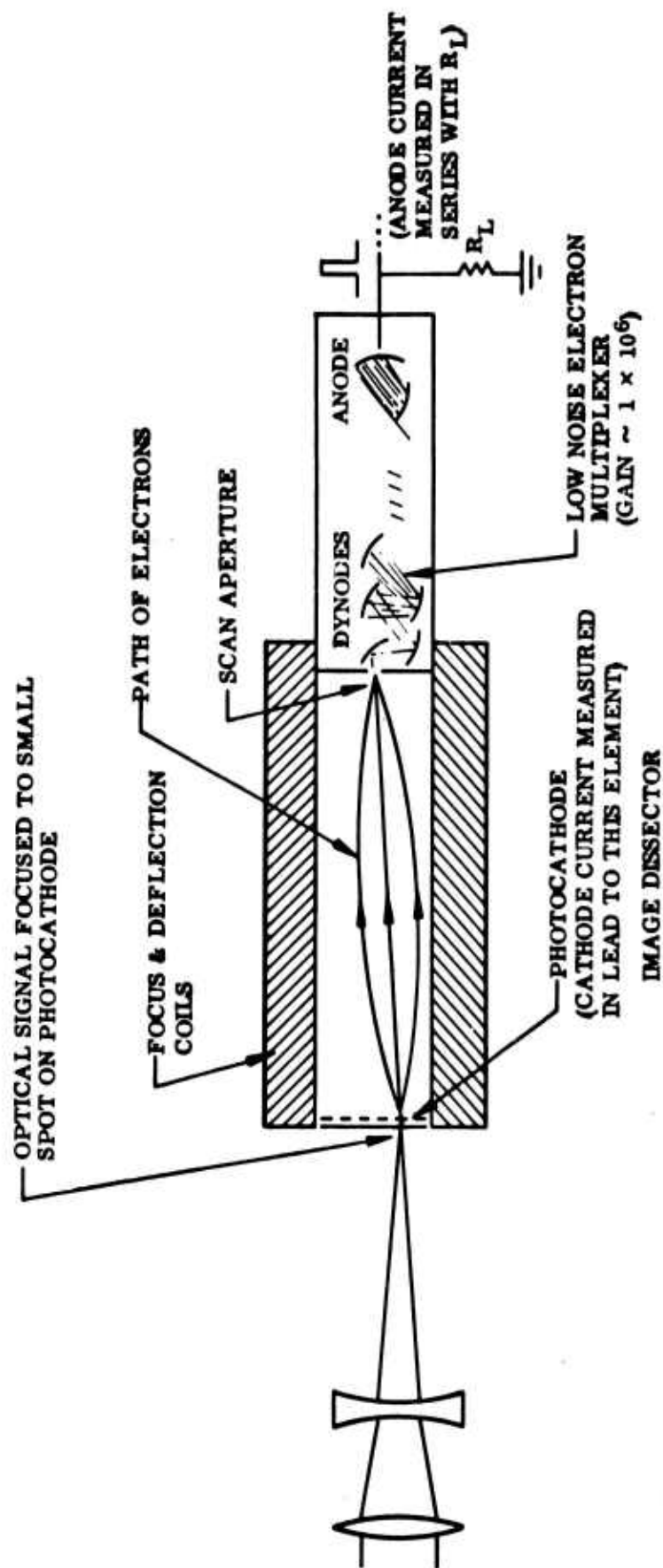


Figure 16 Optics and Sensor of Image Dissector

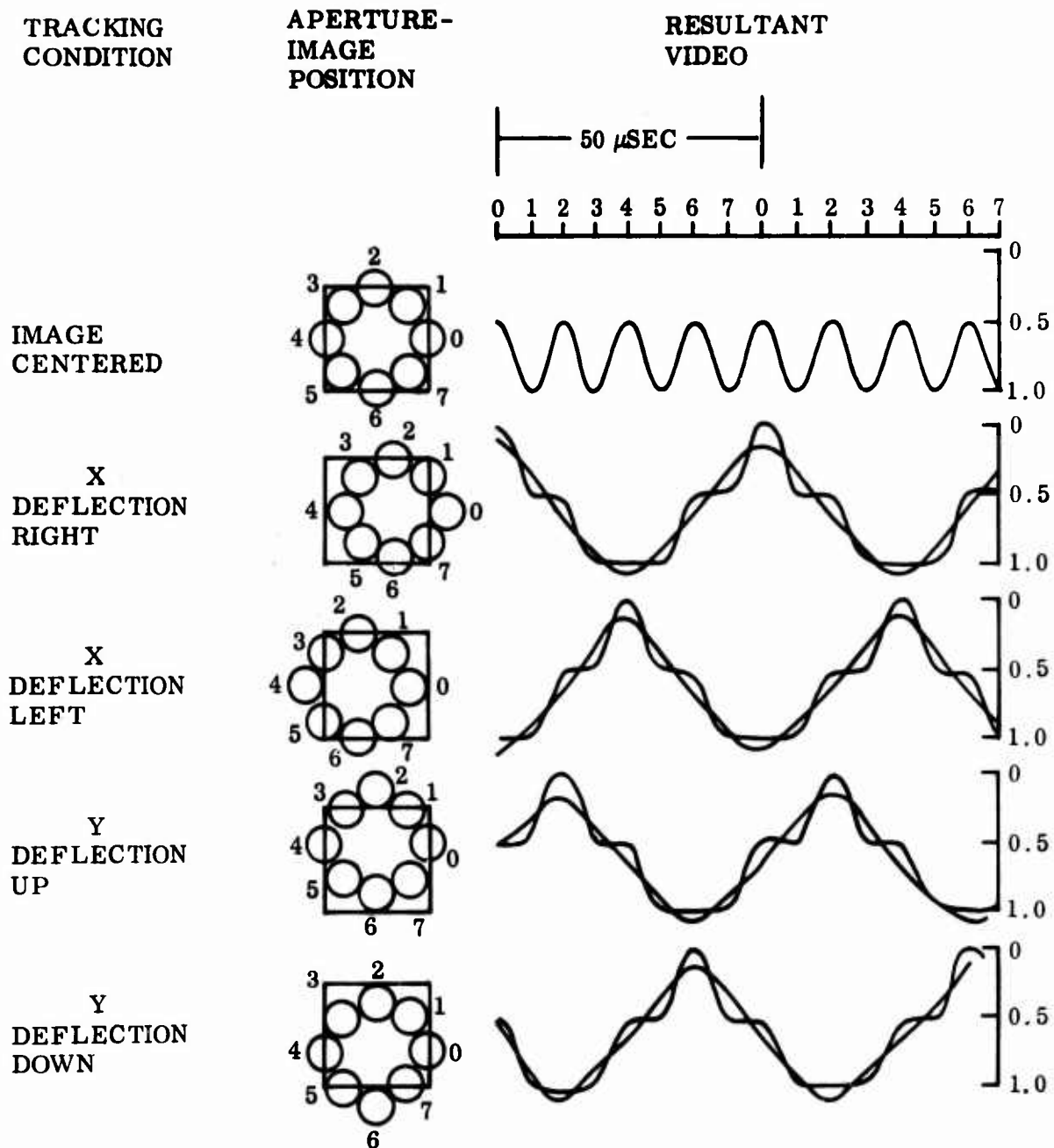


Figure 17 Video From a Conical Scan of an Image in a Square Aperture

At the output of the AGC amplifier, the 20-kHz and 80-kHz components are separated. The 80-kHz component is passed through a 4-kHz band pass filter to minimize the noise bandwidth. After predetection gain, the 80-kHz signal is rectified and filtered to supply AGC control within a 100-Hz AGC bandwidth. A separate filter from the detector supplies an input voltage to a comparator as a target-acquired indication to the tracker to maintain the lock initiated by the target present detector.

The synchronous demodulators receive their reference timing voltages from the deflection currents applied to the tube coils. This assures that the phase of the reference will be correct, assuming negligible delay in the video amplifier. The signal into the demodulator is the 20-kHz signal generated when displacement between aperture and target occurs. For maximum displacement, this 20-kHz signal reaches a 10-V peak-to-peak maximum amplitude. The low-loss FET switches and balanced operational amplifier form a nearly 100-percent efficient demodulator. The filtered output varies linearly from 3 to -3 V as the input signal amplitude is changed and the phase of the signal is reversed. The filter after the demodulator is used to adjust the loop bandwidth to 1 kHz. These circuits are labeled Demodulator & Filters in Figure 15.

The deflection coil sensitivity is 110 mA/in. The coil drivers must be capable of supplying ± 30 mA to facilitate tracking over the entire photocathode area. The acquisition scan is summed with the video error signals at the coil driver. This circuit is made up of an integrated operational amplifier and current booster. The coil current is sensed across a resistor in series with the deflection coil. The 20-kHz component is filtered with an active low-pass filter and a low-drift instrumentation amplifier, which raises the error output level to supply inputs to the beam steerer control amplifier.

The track scan generator produces the circular scan on the face of the ID tube. Low-distortion sine-cosine related sinusoidal signals are required. To produce these signals without the requirement for high-quality tuned circuits, a quadrature oscillator consisting of cascade operational integrators with regenerative feedback is used. The two outputs are 90-deg displaced, have less than 1-percent distortion, and have frequency and phase stability limited primarily by the quality of the RC components used in the feedback path. The basic frequency on this oscillator is 20 kHz. The sine-cosine outputs are coupled to the deflection amplifiers through adjustable resistor attenuators. Manual adjustment of the scan amplitude enables setting to the optimum value.

The acquisition scan generator illustrated in Figure 15 is made up of two synchronized ramp generators which produce a raster search scan on the ID tube. The 20-kHz quadrature oscillator output is divided by 256 to provide a timing pulse for the fast ramp generator.

The fast ramp generator provides a 12.8-ms-period, linear, sawtooth signal to the x-coil deflection driver. A divide-by-64 circuit from the 12.8-ms pulse provides a 819-ms timing pulse for the slow ramp generator. The slow ramp generator provides a linear sawtooth to the y-coil deflection driver.

When a target present pulse is received from the preamplifier, sample-and-hold circuits are activated in the fast and slow ramp generators. These sample-and-hold circuits retain x and y position voltages proportional to the position of the target for a period of time, allowing the track scan to build up error voltages. These error voltages in turn are used by the beam steerers to position the beam.

f. Optical Attenuators

Wedge-shaped optical attenuators were placed in front of the image dissector to vary the signal level received at the photocathode. This permitted investigation of tracker performance as a function of signal level and protected the photocathode from damage. To decrease the possibility of multiple targets at the photocathode because of secondary reflection, the attenuators were wedge-shaped (3 deg) and had antireflective coatings on the back side.

The optical attenuators used were neutral density filters manufactured by Optical Industries, Inc. Filters of 1, 2, and 3 density were used. Two attenuators were placed simultaneously in the optical path to cancel out beam deviation, and resultant attenuations were from 30 to 60 dB in 10-dB steps. They were flat to 2 wavelengths at 6328 Å, and the surface quality (scratch and dig) was 80/50. Being fixed in position and used only on a 2-mm spot, the effect of these attenuator tolerances was considered negligible.

g. Pointing Laser

The pointing laser used was a Spectra-Physics model 126 HeNe laser. It had been planned to use an argon laser to provide a pointing beam of a different color than the beacon beam in simulation of the 0.53 μ doubled YAG of the SDRS. However, tests were conducted on two argon lasers. Both had problems of beam angular noise and mechanical vibrations which made them undesirable for use on the rate table. An attractive alternative was a convection-cooled HeCd laser, but delivery was so long that one could not be obtained for these tests. However, one is being obtained for another contract, and will be used to check out this system for two-color operation after completion of this report.

One argon laser was the Coherent Radiation Model 54. This laser has heavy hoses for cooling water attached to it. These are sources of mechanical and hydraulic coupling of external vibrations to the top of the rate table. This laser also was quite long which created an installation problem.

The second laser was a Spectra-Physics model 162-2 forced air-cooled argon laser. This laser was only 13 in. long and was more suitable for installation. However, the forced air-cooling motor and blower were the source of considerable mechanical vibration and acoustical noise. The measured angular noise of the laser output was many microradians. This angular noise combined with the vibrations which would be transmitted to the whole system weighed against using this laser for the testing program. It was determined that the angular noise dropped by a factor of 10 when the blower motor was turned off. However, the laser would operate only a few seconds in this mode before the over-temperature control turned it off. For initial alignment and preliminary testing, it was decided to use another HeNe laser as the pointing laser until a different color laser could be worked out. It turned out that the tracking and pointing could be successfully operated with the same wavelength light going both ways. The test program was conducted with that configuration. The only problem

was a tendency of the tracker to acquire and track the pointing laser. It can be seen from the optical schematic (Figure 18) that light going to the ID due to multiple reflections of the pointing laser at the beam-splitter will constitute a false target against which the bandpass filter does not discriminate. False acquisition was circumvented by blocking the pointing laser beam during acquisition. Once locked on and tracking, the pointing laser had no effect on the tracking as long as a point-ahead angle was maintained so that the pointing laser did not fall in the ID aperture. The pointing laser used was a Spectra-Physics model 126. This has an output of 3 mW rated, and was measured at the conclusion of the tests as 2.75 mW. Actual power was not a factor in the pointing measurements since the laser was effectively a piece of test equipment to measure how well the mirrors were being positioned. Consequently, it was desirable to have a maximum of pointing laser power so that the S/N ratio would be high and the contribution of shot noise to the pointing would be negligible.

The beam diameter was 0.65 mm, which was appropriate for feeding directly into the tracking optical system where the 11.3 power telescope increased the beam diameter to 7.5 mm. No spatial filter or beam expander was used, so it was necessary to measure the angular noise present in the laser beam. This was measured by reflecting the pointing laser into the image dissector and tracking it. Tracking noise was taken as the laser angular noise. This was measured as 3 microradians rms of laser noise. Because of the telescope demagnification of angles, going from the laser to the pointing detector, the net pointing error component due to pointing laser noise was 0.3 microradians.

h. Boresighting

A retroreflector (or corner cube) was used to align the pointing laser with the beacon laser, using the technique proposed for the SDRS and shown in Figure 19. The retroreflector had an accuracy of 1 arc-sec and a diameter of 0.5 in. With this accuracy, alignment of the laser to the image dissector would be to an accuracy of 1 arc-sec which, considering the telescope power, would be a boresighting accuracy of 0.4 microradian. Boresighting in space would require a corner-cube made to order with two or three times more accuracy than catalog items.

Actual boresighting was easily accomplished although it was noted that certain precautions were required. It was necessary to have the laser adjusted with its beam not only parallel to the beacon but also colinear. There were two reasons for this requirement — one was that if the pointing laser beam was very far off the axis of the telescope — the location of the beacon beam — it might be blocked or truncated by an aperture in the telescope. The other was that if the ID were not perfectly focused, a lateral displacement of the beam would result in an angular shift and consequent error in boresight. It was observed that when the retroreflector was not right on axis and the beam out of the retroreflector was displaced from the incoming beam, that the boresight position of the beam was slightly dependent upon the amount of the lateral displacement. Whether this was due to the lack of perfect focus in the ID mentioned above, or due to imperfection of the retroreflector causing its direction of reflection to be a function of the position on its surface, was not determinable.

Another effect was noticed but not observed to cause any error. This was that if the beam, in its path through the retroreflector, straddled one of the retroreflector edges,

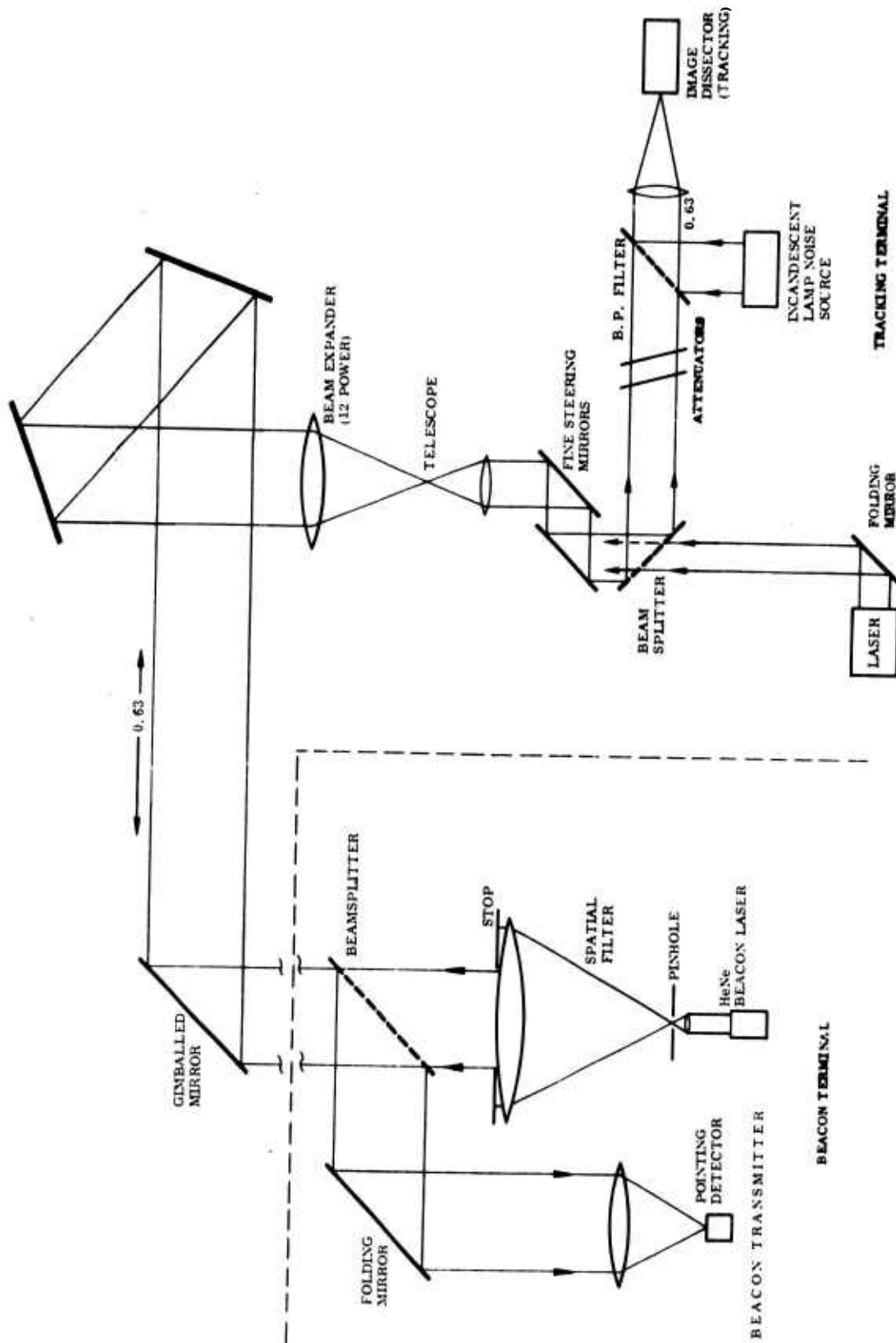


Figure 18 Fine Acquisition Tracking and Pointing - Optical Components

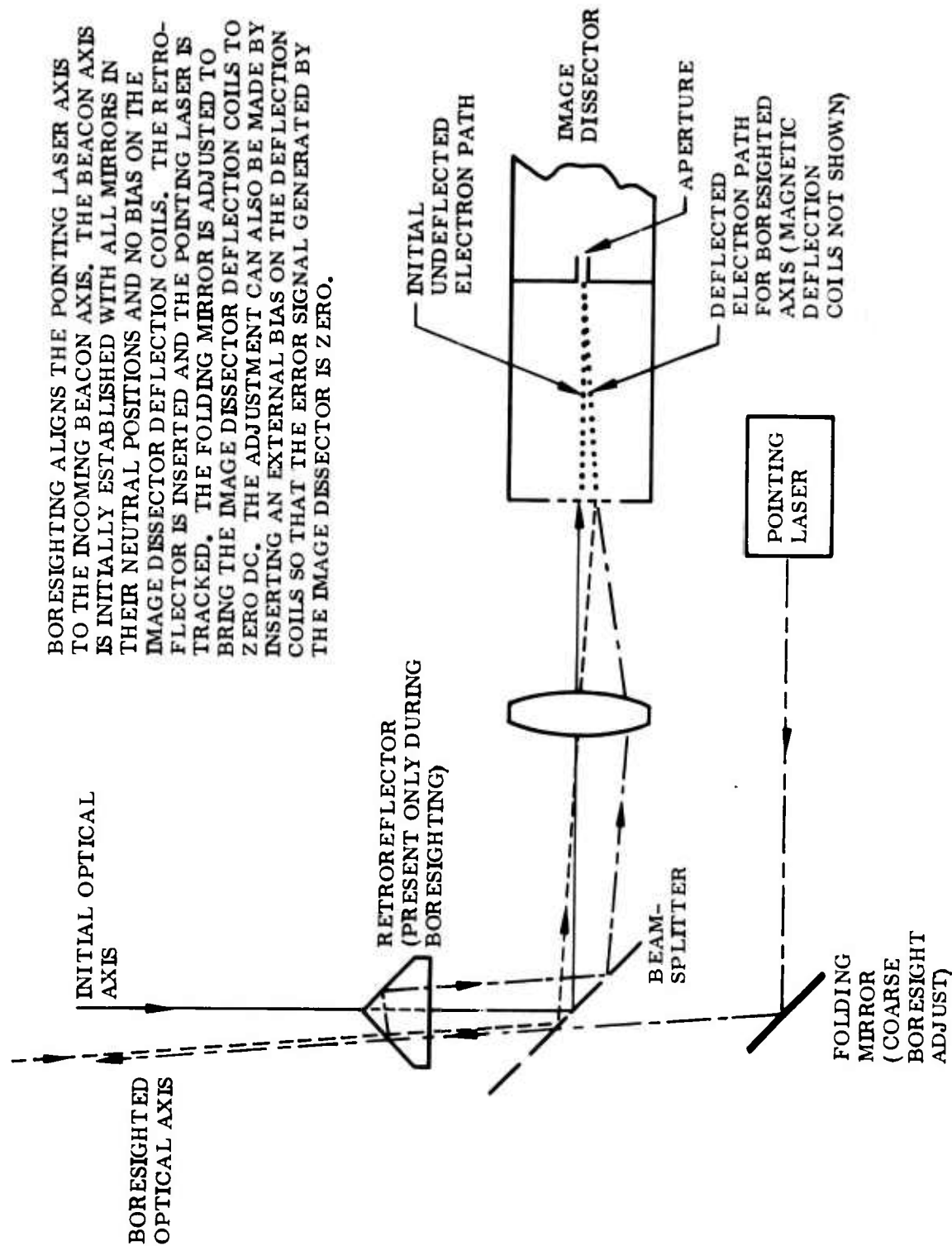


Figure 19 Boresighting Method

a substantial noise showed up in the image dissector error signal. This was assumed to be the result of the beam being reflected at slightly different angles on each side of the edge and of the slight angle modulation of the pointing laser, previously mentioned, varying the proportions coming off at each angle and thus causing the spot in the image dissector to be moving in accordance with the angle noise.

i. Point-Ahead

Point-ahead has no direct analogy in the laboratory since it is impractical to produce the real-life relative velocities between the terminals. However, it is simulated by introducing a known point-ahead angle in the pointing beam. This is merely a controlled boresight error and is readily introduced using the boresighting technique just described. It is done simply with the equipment available by first boresighting the system. Then the fine steering mirrors are disabled and the image dissector dc error voltages, if any, noted. A wedge is then inserted in the beacon beam and biases applied to the deflection coils to bring the ID error voltages to their former value. A point-ahead angle of the value of the wedge is thus inserted. The system is returned to normal operation and the wedge placed in the pointing detector optical path, maintaining its orientation. This compensates for the point-ahead angle and brings the pointing detector back to zero within the experimental accuracy described on page 92.

j. Gimbal Servo

(1) Function of Outer Loop. (Gimbal Drive Loop). The function of the gimbal loop is to reduce the deflection and deflection rate of the agile steering mirror when the table or incoming beam is moving. In the process of subtracting the table or beam motion, the gimbal friction and gimbal loop noise should not contribute significant additional tracking error in the agile beam steerer (inner) loop.

Reducing the motion of the agile beam steerer mirror is required because the mirror has a spring restraint and a viscous restraint (mirror rate damping). A tracking error signal is needed to counteract the restraint torques resulting from the motion of the agile mirror relative to its base. The outer loop bandwidth was established on the basis of limiting this tracking error.

(2) Essential Elements of the Breadboard Gimbal and Beam Steerer Control Loops. The laboratory test unit uses an already developed agile beam steerer. The beam steerer mirror is mounted in flexure pivots and is torqued by a d-c torquer. It has a Kaman displacement transducer to measure mirror angle. The essential elements of the control loops are shown in Figure 20.

Loop A is the high gain control of beam steerer angle based on the image dissector tracking error. The loop has a d-c gain of 83,600 oz-in./rad of mirror deflection. The high d-c gain is due to an integral network that becomes effective below 67 rad/sec.

Loop B is a mirror damping loop using the differentiated output from the Kaman displacement transducer. This loop is the rate restraint which, as mentioned earlier, demands a tracking error whenever the mirror is in motion.

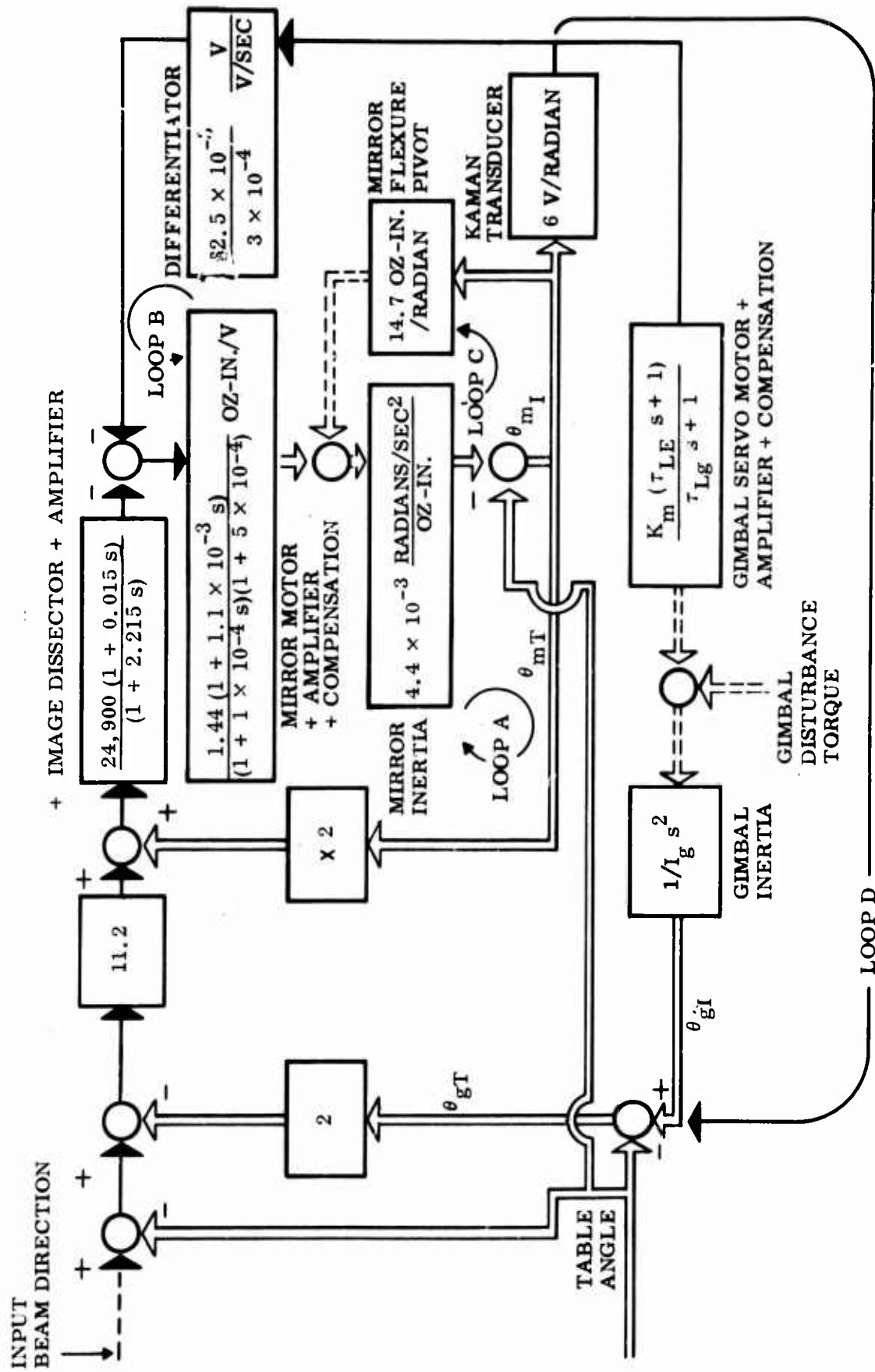


Figure 20 Fine Steering and Gimbal Loops

Loop C is restraint of the flexure pivots supporting the mirror. This is the angle restraint which also demands a tracking error if the mirror is deflected.

Loop D is the gimbal loop. The Kaman displacement transducer senses the agile mirror angle and commands the gimbals in order to keep the steerer mirror angle and rate low.

The following discussion centers around the requirement for gimbal loop bandwidth (loop D).

(3) Agile Mirror Motion Due to a Step in Gimbal Friction Torque. If a small step function torque input to the gimbal is assumed (the friction step input is discussed in Ref. 1), an approximation to the tracking error to compensate for the mirror viscous restraint is given by:

$$\epsilon_t = \frac{3 T_d K_v e^{-\frac{\zeta}{\sqrt{1-\zeta^2}} \times \omega_g t}}{I_g \omega_g (K_a \times 2)} \times \sin \omega_g t \quad (1)$$

where

T_d = Magnitude of step disturbance torque (oz-in.)

I_g = Gimbal inertia (oz-in.-sec²)

ζ = Damping ratio of gimbal servo loop

ω_g = Resonant frequency of gimbal servo loop

K_a = Tracking error gain (oz-in./rad)

K_v = Viscous restraint gain $\frac{\text{oz-in.}}{\text{rad/sec}}$

Equation (1) shows the direct effect of the viscous restraint K_v on the tracking error. The peak error due to this effect is when $\omega_g t = (\pi/4)$. The following parameter values are used to estimate the peak tracking error:

$$\frac{2 K_a}{K_v} = 905 \text{ rad/sec}$$

$$I_g = 0.3 \text{ oz-in./sec}^2$$

$$\omega_g = 30 \text{ Hz, } = 188 \text{ rad/sec}$$

$$T_d = 0.0125 \text{ oz-in.}$$

Utilizing these parameters, the following is obtained

$$\epsilon_{t_{\text{peak}}} = \frac{3 \times 0.0125}{0.3} \times \frac{1}{905} \times \frac{1}{188} \times e^{-(\pi/4)} \times 0.707 \quad (2)$$

$$\epsilon_{t_{\text{peak}}} = 0.24 \mu\text{rad} \quad (3)$$

Equation (3) gives the peak tracking error to counteract the viscous mirror restraint when a torque step of 0.0125 oz-in. is applied to the gimbal. The 0.24 μrad peak error is adequately low because the rms effect, assuming a random sequence of steps, would probably be less than 0.1 μrad . This analysis established the requirement for a 30 Hz bandwidth outer gimbal loop.

The spring restraint of the mirror flexure support also introduces tracking errors. This error is essentially eliminated in steady state by the large d-c gain provided by the integral network in loop A (Figure 20). The following is an approximate equation for the tracking error to compensate for the mirror spring restraint when a step torque input to the gimbal is applied:

$$\epsilon_t = T_d \times \frac{2}{I_g} \times \frac{K_f}{2K_a + K_f} \times \frac{1}{(\sigma_a^2 + \omega_g^2)} \times \left\{ e^{-\sigma_a t} - e^{(-\zeta/\sqrt{1-\zeta^2})\omega_g t} \right. \\ \left. \times \left[\cos \omega_g t - \left(\frac{\sigma_a \sqrt{1-\zeta^2}}{\omega_g \zeta} - 1 \right) \sin \omega_g t \right] \right\} \quad (4)$$

where

T_d = Value of disturbance torque step (oz-in.)

I_g = Gimbal inertia (oz-in.-sec²)

K_f = Mirror flexure stiffness (oz-in./rad)

K_a = Tracking error to mirror torque gain (oz-in./rad)

σ_a = Integral control break point frequency (rad/sec)

ω_g = Servo loop resonant frequency (rad/sec)

ζ = Servo loop damping ratio

The peak value of this error occurs near $\omega_g t = \pi$, that is:

$$\epsilon_t \text{ peak} = T_d \times \frac{2}{I_g} \times \frac{K_f}{2 K_a + K_f} \times \frac{1}{(\sigma_a^2 + \omega_g^2)} \times \left(e^{-\pi \sigma_a / \omega_g} + e^{-\zeta \pi / \sqrt{1 - \zeta^2}} \right) \quad (5)$$

Using the same parameters as used in Eq. (3) and additionally using

$$K_f = 14.7 \frac{\text{oz-in.}}{\text{rad}}$$

and

$$\sigma_a = 67 \text{ rad/sec}$$

we get

$$\epsilon_t \text{ peak} = 0.0125 \times \frac{2}{0.3} \times \frac{14.7}{502.7} \times \frac{e^{-0.357 \pi} + e^{-\pi}}{(4500 + 35,400)}$$

$$\epsilon_t \text{ peak} = 0.023 \mu\text{rad} \quad (6)$$

Equation (6) gives the peak error tracking to compensate for the mirror flexure restraint. It is not significant compared to the effect of the mirror viscous restraint.

(4) Gimbal Loop Design. Based on the criteria developed from Eqs. (1) and (3), the (outer loop) gimbal servo natural frequency is specified as 30 Hz. The gimbal servo is a conventional lead lag compensated loop. The compensation circuits and the frequency response for the compensation are discussed in Section IV, 5.c.(2).

Since the system RMS tracking error is predicted to be less than 0.1 μ radians for the gain parameters specified, it was felt that the servo errors would probably not be

visible during the test. In order to expose potential servo problems that may be barely masked by the high noise* of the breadboard configuration, the gimbal servo was designed with an inertia of 1/10 the nominal value as well as with the nominal value.

(5) Table Acceleration Effects. If the table quickly changes its direction of rotation, the equivalent change in beam rotation rate $\Delta \dot{\theta}_B$ can be deduced from (Figure 20):

$$\Delta \dot{\theta}_B = \left[\left(2 \Delta \dot{\theta}_T - \Delta \dot{\theta}_T \right) \times 11.2 - 2 \Delta \dot{\theta}_T \right] \times \frac{1}{11.2}$$

$$\Delta \dot{\theta}_B = 0.822 \Delta \dot{\theta}_T$$

$$\Delta \dot{\theta}_T = \text{change in table rotation rate}$$

The principal tracking error due to a step in table rate is the tracking error necessary to counteract the peak agile mirror rate. When the duration of the step is short compared to the steering response time, the tracking error depends on the total change in rate and is independent of the acceleration. The peak error is given by

$$\epsilon_t = 0.822 \times \frac{K_v}{2 K_a} \times \Delta \dot{\theta}_T$$

where K_v and K_a were defined at Eq. (1).

If, as in these tests, a 2240- μ rad/sec change in rate occurs in a few milliseconds, the peak error is

$$\epsilon_t = 0.822 \times \frac{1}{900} \times 2240 = 2.04 \mu\text{rad}$$

A comparison of this predicted maximum error (per axis) with measured values is given on page 77 from data shown by Figure 36. The predicted worst case and the measured value are about the same, indicating that the acceleration period was of relatively short duration. Computations for the satellite case, with relatively low accelerations and appropriate values for gain show that the peak error expected during a limit cycle reversal would be on the order of 0.25 microradians and this would exist during a fraction of 1 percent of the time.

*The breadboard configuration has higher noise than the proposed brassboard because of the 1/7 x smaller optical diameter, and because of the noise of the existing displacement sensor on the agile mirror (on the order of 1 microradian; see Figure 41).

k. Test Instrumentation

The following test instruments were employed in the evaluation:

- Precision optical wedges (2), Diffraction Optics Co.: Deflections of ± 4.8 and ± 20.8 μ radians used to calibrate pointing and tracking detectors
- Electrometer, Keithley, Model 620: used for measuring image dissector cathode and anode currents
- Optical power meter, Optics Technology Inc., Model 615: used for monitoring beacon and pointing laser powers
- True rms voltmeter, Ballantine Laboratories, Inc., Model 320: used for true rms reading of tracking errors
- Strip-chart recorder, Sanborn, Model 850: used for recording pointing and tracking errors and other data
- Oscilloscope, Hewlett-Packard, Model 130C: used for continuously displaying the image dissector deflection coil currents
- Oscilloscope, Tektronix, Model 535: used for general-purpose display and photography
- Neutral density optical attenuators (4): used for attenuating beacon beam in 10-dB steps; 10; 20; 30; and 30-dB values
- Function generator: Hewlett-Packard, Model 203A: used as a source of sinusoidal and square-wave signals for testing servo loops and measuring frequency responses of various components
- Fourier analyzer, Hewlett-Packard: used for analyzing the spectral content of the tracking and pointing error signals; consisted of
 - Computer, Model 2115A
 - Analog-to-digital converter, Model 5465
 - Display unit, Model 5460A
 - Oscilloscope, Model H51-180A

The instruments either had their individual calibrations, such as the precision wedges, or were calibrated in the LMSC or ITTG Standards Laboratories. The power meter was uncalibrated but was used only for relative power; the basic measurement of optical power was the current at the cathode of the image dissector.

Section IV

EVALUATION TESTS

1. ACQUISITION, FINE TRACKING SUBSYSTEM - TEST 1

a. Test Objectives

This test measured the performance of target acquisition by the fine tracking subsystem. Three different measurements were made:

- Angular area over which acquisition could take place - Test 1.1
- Average time required to acquire with high signal-to-noise - Test 1.2
- Effects of signal-to-noise on acquisition probability - Test 1.3

b. Results

(1) Angular Acquisition Range - Test 1.1. The angle over which acquisition would occur was measured to be 0.0039 radian in the horizontal dimension and 0.0052 radian in the vertical. This is not the system limit but an arbitrary limit set by truncation of the optical paths. These values were an order of magnitude greater than the SDRS value of 0.0003 radian. It was useful to have the greater range since the initial positioning was manual.

(2) Average Time Required to Acquire - Test 1.2. An average time of 0.66 sec was required to acquire (Table 4). Trials 1 and 6 missed on the first scan and required more than 1 full raster time, indicating that the acquisition threshold was possibly set higher than was necessary. Assuming these would acquire the first scan with a lower threshold, the average time would be approximately 0.6 sec. This is 50 percent greater than 0.4 sec (1/2 raster time). This is probably due to false alarms. The scan time for the SDRS was near 0.2 sec. The difference is accounted for by the time required to scan a much greater angular acquisition area covered by the evaluation equipment.

(3) Effect of S/N on Acquisition Probability - Test 1.3. The rapid variation of the number of false alarms as a function of threshold led to considerable difficulty in accurately adjusting the acquisition threshold to get the desired false alarm rate. False alarms were counted with an electronic counter for a period of a minute; the threshold was then manually adjusted and the count repeated. In an operating system, this would be done automatically and would be not such a tedious operation. Measurements were taken for 1000 and 7500 photoelectrons per integration time of 1 ms. The results are summarized in Table 5. The false-alarms-per-raster rate was preset, changing the threshold for the two cases, and the acquisition probability was determined by comparing the actual acquisitions with the number of scans.

Table 4. Average Time Required to Acquire

Trial No.	Time (sec)
1	0.88 ^(a)
2	0.78
3	0.34
4	0.54
5	0.64
6	1.12 ^(a)
7	0.76
8	0.44
9	0.66
10	0.44
Total	6.60
Average = $\frac{\text{Total}}{10} = 0.66 \text{ sec}$	
Measured Time for One Complete Raster 0.8 sec	

(a) Acquired on second scan.

Table 5. Results of Acquisition Probability Measurements

Electrons/Integration Time	(S/N)_V	False Alarms/Raster	Acquisition Probability per Raster
1000	31	150	0.75
7500	86.5	250	1.00

c. Comparison With Theory

An increase in probability of acquisition with increased S/N was observed as expected. The 75 percent probability of acquisition for the 1000-photoelectron case was, however, significantly less than the 99 percent predicted for photon-limited operation. (Ref. 3, Vol. III, Appendix O, pp 9-22.) This was thought to be caused by a higher threshold setting than would be required for photon-noise false alarms only. This was required because reflections in the optical system produced false targets and because circuit noise was comparable to photon noise. To eliminate these difficulties so that operational objectives can be achieved in future systems, improved optics and the acquisition technique of Ref. 1 should be used. The test system field of view was significantly larger than required. Two fields of view are suggested for future laboratory applications — an expanded field for convenience in alignment and a smaller one for operational use.

2. TRACKING ACCURACY AS FUNCTION OF SIGNAL-TO-NOISE RATIO — TEST 2

a. Test Objective

This test measured the relationship between fast tracking loop S/N and tracking accuracy. The theory for comparison is presented in Ref. 1 and Ref. 2.

b. Test Program

Tracking accuracy was measured for a range of beacon and background received powers simulating the range of photocathode currents ($\sim 10^{-12}$ A) expected for the Phase Va fine tracking by Package A, according to the link analyses in Ref. 1, pp 3-118. The tests included measurement of the rms tracking angle noise in the measured bandwidth of the fast steering mirrors (~ 300 Hz), the signal and background induced photocurrents, and the rms noise current at 20 kHz (the circular scan rate) in an appropriate bandwidth (~ 600 Hz) at the image dissector output. Measurements were made to distinguish shot noise from noise due to fluctuations of the beacon amplitude.

The noise measurement was performed for three different power levels (cases I, II, and III) under the following conditions:

- Flooding of the detector with a low fluctuation background source, a dc incandescent lamp, adjusted in intensity to provide the appropriate cathode current
- Flooding of the detector with the beacon laser signal
- Focusing of the beacon laser signal with the ID scan off. The noise current was measured by means of a filter centered at 20 kHz, with twice the bandwidth of the fast steering loop. This bandwidth was measured by driving the loop from a signal generator and noting the frequency response of the mirror deflection by its position pickoff.

The rms tracking error was determined from the rms tracking error signal at the output of the synchronous detector following the image dissector for each axis. The output voltage error signal was calibrated with respect to angular error by rotating known optical wedges in the beacon beam with the detector loop open. The tracking error was measured with the circular scan on, both while tracking the focused beacon image and with the ID flooded with the appropriate level illumination (but not tracking), to distinguish beacon angle wander from true quiescent tracking error. Noise was measured in the bandwidth of the fast steering mirror loop since that bandwidth is most relevant in determining system performance limitations.

c. Test Configurations and Plan

(1) Signal and Noise Measurements. The following conditions existed in Test 2.1:

- Circular scan and all control loops: Off
- Image dissector: On
- Cathode and anode current meter: On

The test procedure was as follows:

- (a) Set flood illumination at levels that gave the calculated cathode current and measured anode noise current in the loop bandwidth, and measure dc anode and cathode currents.
- (b) With the defocused HeNe beacon illumination set to give calculated cathode current, anode noise current and dc anode and cathode currents were measured.
- (c) With focused HeNe beacon and centered image on image dissector effective aperture, measure illumination level and repeat current and noise measurements.
- (d) Repeat Step c. with addition of background illumination.

The test data are presented in Table 6.

(2) Tracking Error Measurements. The following steps were performed in Test 2.2:

- (a) Calibrate error signal current after synchronous detector by placing known optical wedges in beacon beam (Table 7).
- (b) Measure noise on the tracking error signal with focused beacon plus background, ID loop on, and beam steerer loops off.
- (c) Repeated Step b. with the beam steerer loops on.

Table 6. Signal and Noise Measurements Data – Test 2.1

Item	Case I	Case II	Case III
Test Configuration			
Image dissector: On			
Circular scan: Off			
Beam steerers and ID loop: Off			
Gimbal: Off and locked			
Meters in cathode and anode circuits			
Nominal Cathode Current (A)	10^{-11}	10^{-12}	10^{-13}
Beam Steering Bandwidth (Hz)	300	300	300
Flood Illumination			
Anode dc current (μ A)	10	1	0.1
Cathode dc current, through aperture (A)	10^{-11}	10^{-12}	10^{-13}
Anode noise voltage – In steering bandwidth (mV)	7	2	0.6
Calculated Noise Figure	1.34	1.21	1.0
Defocused Beacon Illumination			
Anode dc current (μ A)	9	1	0.15
Cathode dc current (A)	$.9 \times 10^{-11}$	10^{-12}	1.5×10^{-13}
Anode noise voltage (mV) (in steering bandwidth)	7	2.2	0.8
Focused Beacon Illumination (No background; centered for minimum error output)			
Anode dc current (μ A)	10	1	0.1
Anode noise voltage (mV)	14	23	49
Focused Beacon Plus Background Illumination			
Anode dc current, no background (μ A)	10	1	0.1
Anode dc current, signal plus background (μ A)	20	2	0.2
Anode noise voltage (mV)	24	34	61

Table 7. Image Dissector Sensitivity Calibration

Element Item	Horizontal		Vertical	
	1	2	1	2
Optical Wedge No.	1	2	1	2
Beam Deviation (μ rad)	47.6	9.7	41.6	9.7
Phase Detector Output (mV)	740	200	650	161
Sensitivity (mV/ μ rad)	17.8	20.6	16.35	16.6
Average, weighted, (mV/ μ rad)	18.5		16.5	

Step b shows the performance of the system including beacon amplitude or angular noise. Step c indicates the performance limitations of the overall system.

The test data are presented in Table 8.

d. Results

(1) Signal-to-Noise (S/N) Measurements – Test 2.1. The anode noise current for Test 2.1 was calculated by dividing the anode voltage by the load resistance (110,000 Ω). The noise current is shown in Table 9, together with the theoretical photon-limited current for comparison. The measured S/N ratio was defined as the ratio of anode signal current to measured noise, and the photon-limited S/N ratio is the ratio of anode dc current to the calculated photon-limited noise current. These are also shown in Table 9. A comparison of the results shown in Table 9 reveals the nature of the noise entering the tracker. The flood illumination and defocused beacon measurements are influenced primarily by photon noise. The measured values of noise current and $(S/N)_V$ are about 50-percent poorer than the photon-limited calculations. This result was anticipated because the optical components in the system are off-the-shelf and not optimized. The focused beacon, on the other hand, shows much poorer performance than the photon-limited source. This is because the tracking and fine gimballed mirrors circuitry was not activated to track out scintillation noise arising from passage of the beam through the atmosphere. The increase varied from a factor of 2 worse than the defocused beacon for Case I to a factor of 10 worse for Case III. Addition of significant background illumination produced still more noise as was anticipated. To simulate the satellite-to-satellite situation without fine gimbal corrections would, therefore, require significantly increased care to reduce the effects of atmospheric turbulence.

(2) Tracking Error Measurements – Test 2.2. The theoretical photon-limited tracking error was calculated, using Eq. 4.20 of Ref. 1 (vol. III, pp 0-47). The measured noise in millivolts was converted to tracking error by dividing by 18.5 (the conversion factor measured for the horizontal channel). The values are shown in Table 8. Tracking errors with the fine gimbal on are a little larger than the photon

noise but well within the expected range for the optics used and the scintillation from air currents. (The 0.09- μ A-case measured error is slightly better than theory, but within experimental tolerances for background and calibration techniques for this low signal.)

Extraneous noise sources such as scintillation have obviously been minimized. When the fine gimbal was turned on the noise level increased by 100% for the 9 μ A case and by 30% for the 0.9 μ A case. Track was not established for the 0.09 μ A case. The

Table 8. Theoretical and Measured Tracking Error

Item	Case I	Case II	Case III ^(a)	
Attenuation (dB)	40	50	60	
<u>Fine Gimbal and Coarse Gimbal Off</u>				
Anode Current – Beacon Alone (μA)	9	0.9	0.09	
Anode Current – Background Alone (μA)	0.55	0.55	0.55	
Anode Current – Signal plus Background (μA)	9.55	1.45	0.64	
Voltage Signal-to-Noise Ratio	210	53	8.2	
RMS Phase Detector Output, Horizontal Channel (mV)				
• Background Off	7.5	17	37	
• Background On	8	20	64	
Equivalent Angular Tracking Error (μr)	0.4	1.0	3.5	
Theoretical Photon Limited Error (μr)	0.2	0.8	5.1	
	Case I	Case II		
	Coarse Gimbal Off		Coarse Gimbal On	
	Anode Current – Beacon Alone (μA)	9	0.92	0.92
	Anode Current – Signal Plus Background (μA)	9.55	1.47	1.47
	RMS Phase Detector Output, Horizontal Channel (mV)	15	25	35
	Measured Tracking Error (μr)	0.8	1.3	1.9

(a) Much less than zero-dB S/N margin; tracking not accomplished

increase in fine gimbal noise signifies that circuit noise in the fine gimbal loop is significant for low photon-limited-noise operation. The major source of this circuit noise is the position pick off. In future systems this noise can be reduced by improvement or elimination of the position pick-off to reduce the circuit noise.

The only measurement taken with the coarse gimbal turned on was in Case II. Tracking error increased about 50 percent for this case, indicating that additional circuit noise resulted.

It is likely that this also is primarily the effect of the noise in the fine steering mirror position pick-off since this position signal is the command to the gimbaled mirror servo. Consequently, the pick-off noise puts noise into both the fine and gimbaled mirror loops and becomes the most significant noise source in tracking error except under very low signal-to-noise conditions.

Table 9. Signal-to-Noise Measurement Data

Condition and Case	Anode dc Current (A)	Measured Anode Noise Current (A)	Photon Limited Anode Noise Current (A)	Measured Signal-to-Noise (V)	Photon Limited Signal-to-Noise (V)
Flood Illumination					
Case I	10^{-5}	6.4×10^{-8}	3.1×10^{-8}	157	321
Case II	10^{-6}	1.8×10^{-8}	9.6×10^{-9}	56	104
Case III	10^{-7}	5.5×10^{-8}	3.1×10^{-9}	18	32
Defocused Beacon					
Case I	9×10^{-6}	6.3×10^{-8}	2.8×10^{-8}	159	358
Case II	10^{-6}	2×10^{-8}	9.6×10^{-9}	50	104
Case III	1.5×10^{-7}	7.3×10^{-9}	4.66×10^{-9}	21	33
Focused Beacon					
Case I	10^{-5}	1.3×10^{-7}	3.1×10^{-8}	77	321
Case II	10^{-6}	2.0×10^{-7}	9.6×10^{-9}	5	104
Case III	10^{-7}	4.5×10^{-7}	3.1×10^{-9}	2.2	32
Focused Beacon Plus Background					
Case I	2×10^{-5}	2.2×10^{-7}	5.3×10^{-8}	45	189
Case II	2×10^{-6}	3.1×10^{-7}	1.6×10^{-8}	3.2	61
Case III	2×10^{-7}	5.5×10^{-7}	5.3×10^{-9}	0.4	19

3. TRACKER AGC SENSITIVITY

a. Laboratory Tests

The first part of the tracker AGC sensitivity test was to determine the effect of the preamplifier AGC level on tracking accuracy over the AGC dynamic range. The second part of the test was to determine the bandwidth of the AGC circuit.

The dynamic range test was performed by attenuating or amplifying the image dissector output to the preamp circuit as shown in Figure 21. By varying the attenuation at this point, the S/N ratio was kept constant while the signal level was varied. While varying the signal over the dynamic range, the tracker error voltage was monitored. Any change in sensitivity due to the signal level variation would be indicated by a change in the error voltage.

Table 10 presents the data collected for both the horizontal and vertical channel.

Table 10. AGC Dynamic Range

Signal Attenuation	Horizontal Channel Tracker Error Voltage (mV rms)	Vertical Channel Tracker Error Voltage (mV rms)	Video Signal (V p-p)
189 (Min. Tracking Signal)	16.0	24.5	0.009
100	16.0	24.5	0.017
10	15.5	24.5	0.170
1	15.5	24.5	1.700
2.35 gain (Max. Tracking Signal)	13.0	41.0	4.006

The video signal column is the output from the attenuator (amplifier). With the initial condition of anode current equal to $9.8 \mu\text{A}$, the video signal level was 1.7 V peak-to-peak (gain = 1). The data are plotted in Figure 22.

The data show a constant error voltage over a wide range of signal power. When the maximum signal level that could be handled was exceeded, horizontal and vertical channels drifted in opposite directions. However, the change in error voltage was not caused by the amplifier because similar error voltage changes were recorded before using the amplifier. The different senses of the gain change could be accounted for by a phase change in the error signal as a function of signal amplitude at very strong signals. It was not determined if this was the case. The gain portion of the test was performed two days after the attenuation part of the test. A change in the relative noise level of the two channels was noted over the interval. However, this did not affect the AGC sensitivity test.

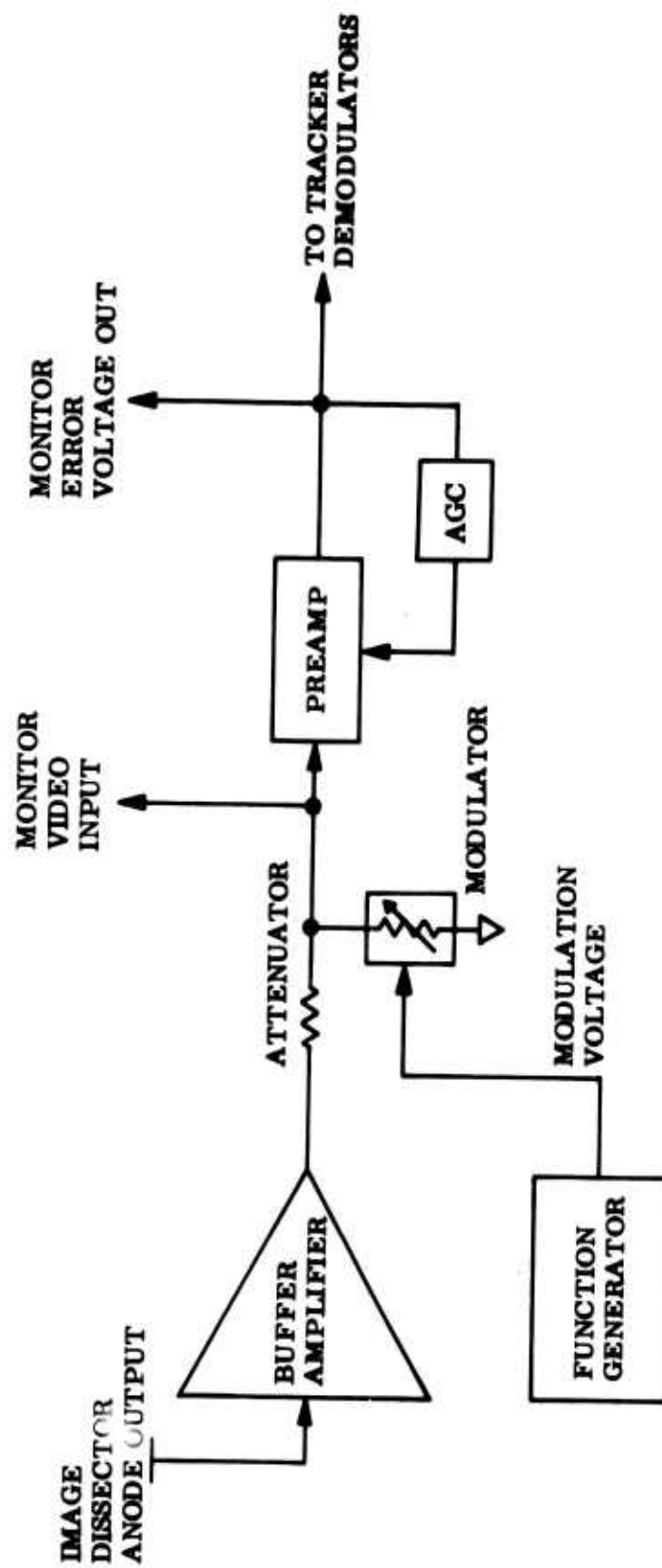


Figure 21 AGC Circuit Performance Evaluation – Block Diagram

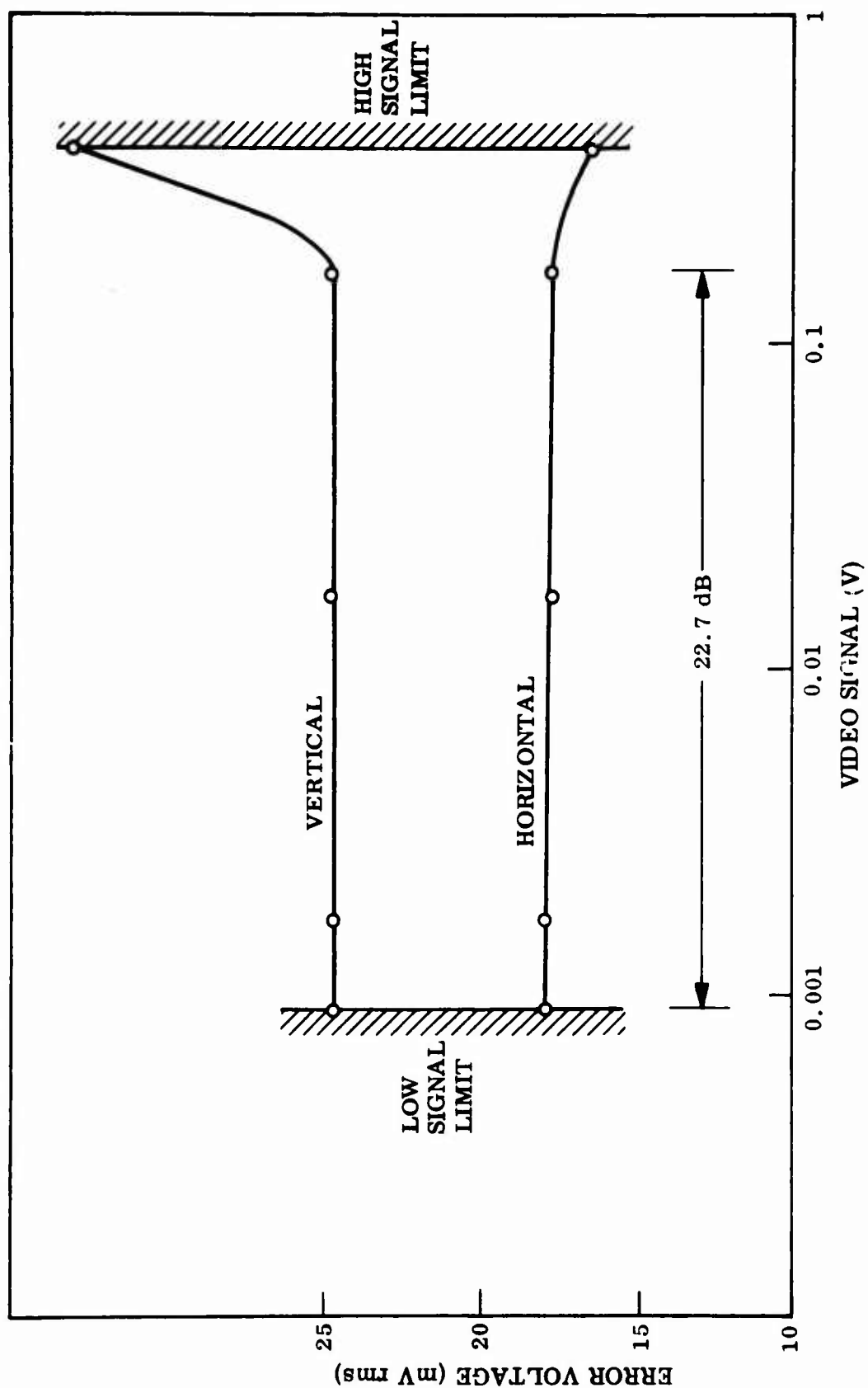


Figure 22 AGC Dynamic Range

For the AGC frequency response test, test points were measured around the expected AGC 3-dB bandwidth frequency. The output of the AGC loop was modulated with a constant amplitude sine wave and the video signal modulation at the preamplifier output was monitored. The 3-dB frequency is defined as that frequency at which the modulation is 0.707 of the maximum modulation. Figure 23 is a plot of the data collected during the test. The vertical axis is the percentage of video signal modulation with 100 percent corresponding to maximum modulation and zero AGC action. From Figure 23, the 3-dB point occurs at a frequency of 70 Hz.

b. Results and Comparison with Predicted Performance

For the tracking accuracy versus AGC level test, the results agreed with the predicted performance. The 3-dB point in the frequency response test was 30 Hz lower than the predicted 100 Hz.

During the subsystem design (Ref. 1), the tracking accuracy was planned to be independent of the signal level over a 20-dB dynamic range of the AGC circuit. This design goal was met since the measured dynamic range of 189 to 1 (22.7 dB) gave little change in the tracking error signal amplitude. The change in horizontal error voltage being 0.5 mV, out of 16 mV. These results are well within practical operating tolerances.

4. IMAGE SIZE EFFECTS ON TRACKING ACCURACY

a. Test Objectives

This test was to determine the effects of image size on tracking accuracy of the fine tracking subsystem. Image size (both angular and linear) was controlled by changing the diameter of the beam by means of a variable iris installed at the exit of the beacon beam expander. Image size and beam size are inversely proportional. Tracking accuracy and image size were measured for several beam diameters.

b. Test Methods

For each image size, measurements were made of fluctuations in tracking angle (tracking noise) for both the horizontal and vertical channels. Background and signal-plus-background anode currents were measured. Tracker output was calibrated in units of mV/ μ rad by inserting a calibrated wedge in the beam between the transmitting and receiving telescopes and observing the output angular error voltage.

The sizes of the images were measured with an oscilloscope by disabling the track scan and imposing a ramp voltage on the deflection coil to cause the image to sweep across the image dissector aperture. The output of the image dissector versus time was displayed on an adjustable delay oscilloscope with the sweep synchronized, and the trace was photographed (Figure 24). Position along the oscilloscope trace was a measure of image location on the photocathode. The rise time of the signal was a measure of spot size. This can be understood by considering the image dissector output when scanning the image across the aperture. As the image edge enters the aperture, the output rises. If the image is smaller than the aperture, the output

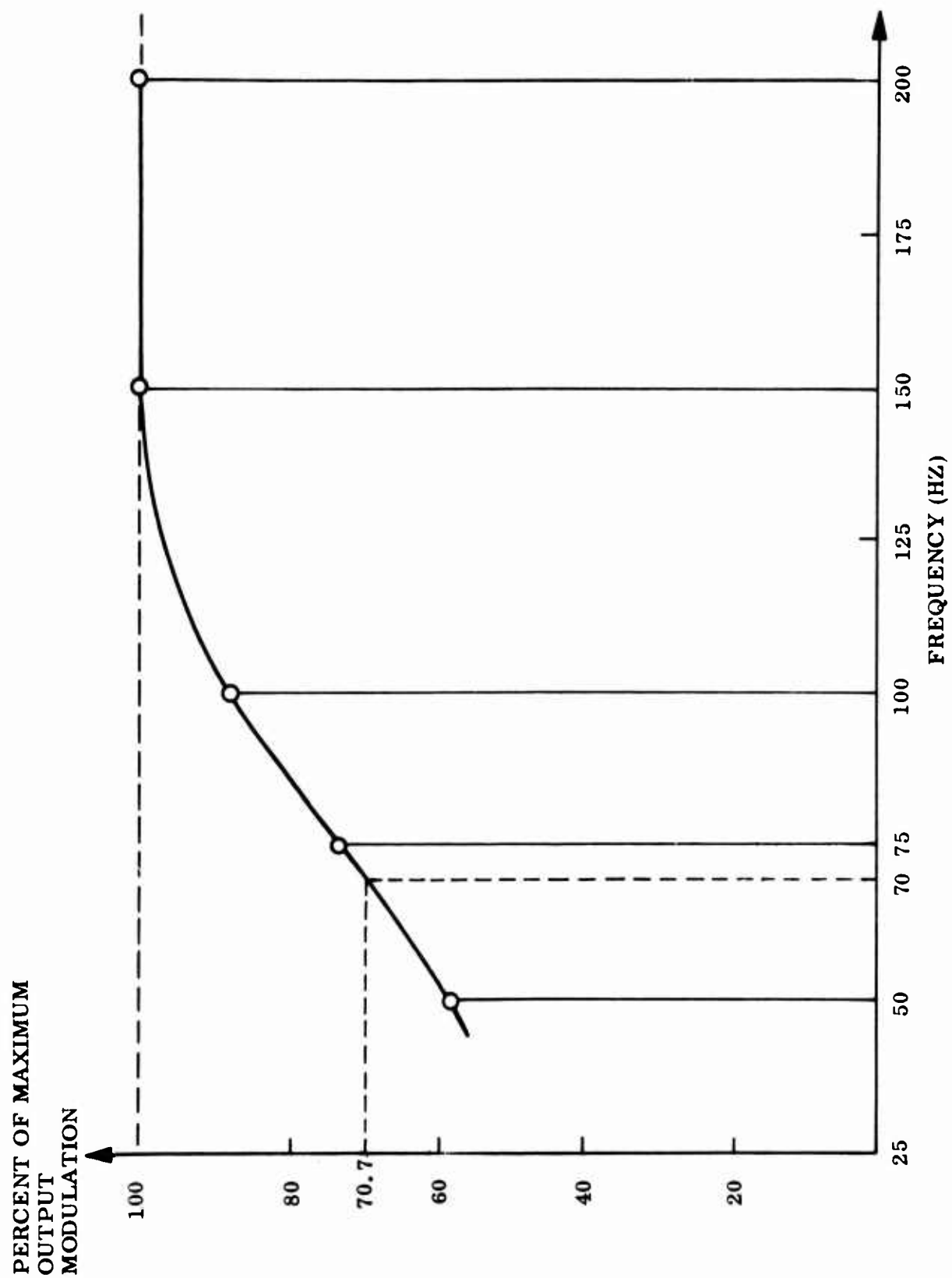


Figure 23 AGC Frequency Response

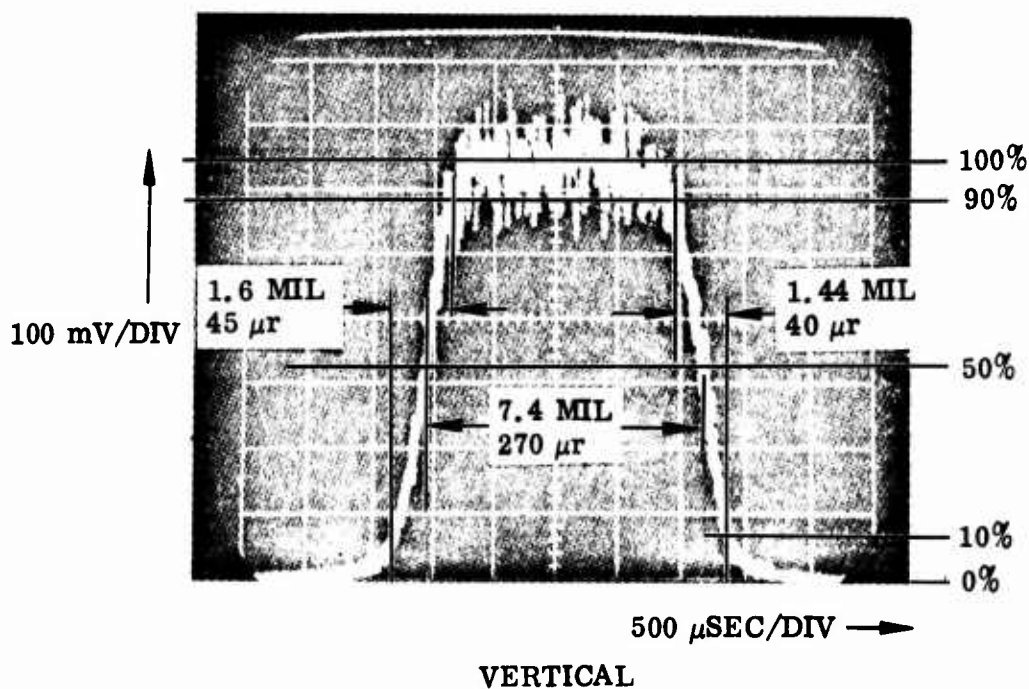
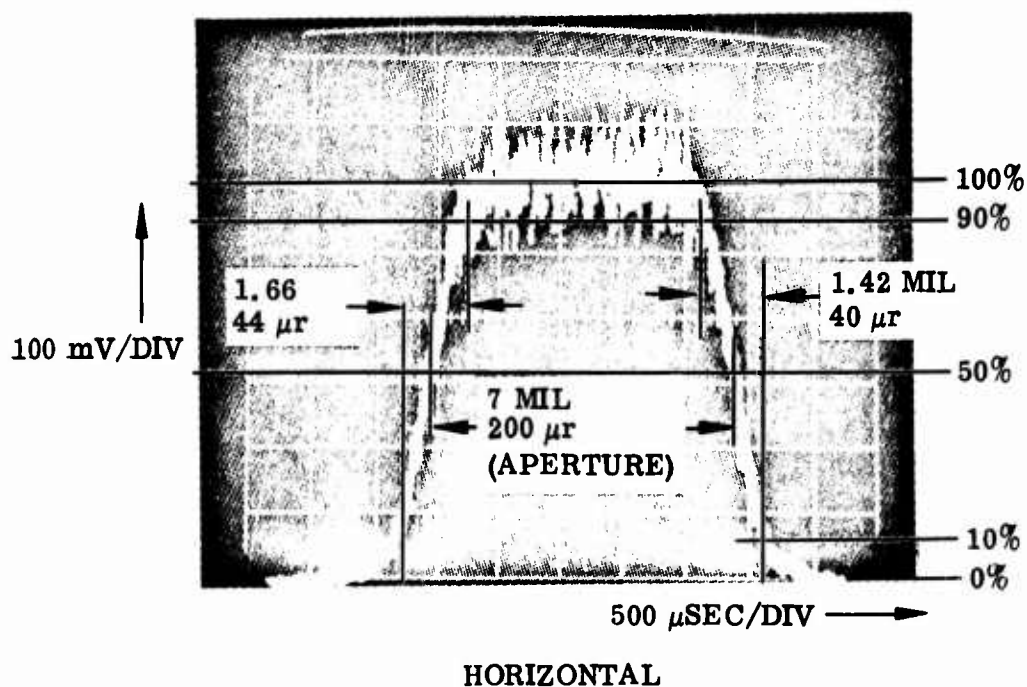


Figure 24 Measurement of Spot Diameter Using Image Dissector Aperture

increases until the full image is within the aperture. The output remains constant until the leading edge of the image spot begins to scan out of the aperture. Then the output decreases until the image is completely out of the aperture. Both rise and fall time are, therefore, measures of image diameter. The 10 and 90 percent amplitude points were used in determining the edge of the image. The resulting measure was approximately 80 percent of the Airy disc diameter. The time axis of the sweep was calibrated in microradians displacement in space by rotating a calibrated wedge in the beam and observing the change in position of the trace.

If the image is larger than the aperture, the constant output will not occur, but the output rises until the center of the image coincides with the center of the aperture. The image size was then measured by (1) measuring the width from where the image begins to enter the aperture until it leaves the aperture and (2) subtracting the size of the aperture from this width.

A comparison of the scope traces as seen for three different beam-widths is seen in Figure 25 in which the rise and fall times of the pulses are proportional to the width of the images.

c. Test Data

The following procedure was observed:

- (1) The tracker output was calibrated by measuring the variation of its output voltage (fine gimbal mirrors off) as a calibrated wedge was placed in the beacon beam between the transmitting optics and collecting optics, with the results shown in Table 11.

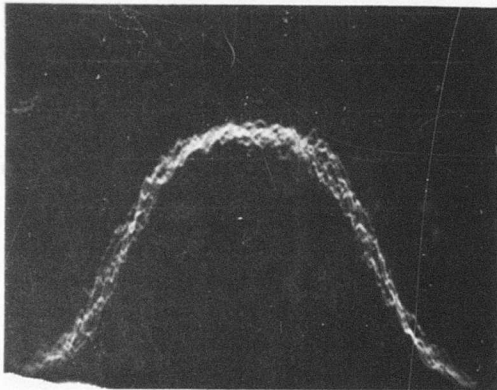
Table 11. Image Dissector Sensitivity Calibration

Channel	Sensitivity (mV/ μ r)
Horizontal	18.5
Vertical	16.5

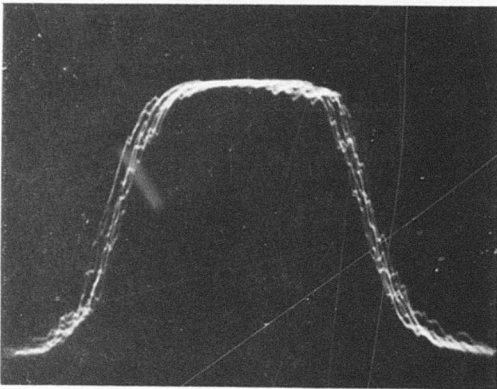
- (2) The horizontal and vertical tracking error voltages for each of the cases of interest were recorded and the error angles calculated or measured with an rms voltmeter with the results as shown in Table 12.
- (3) The signal and background image dissector anode currents for each diameter were recorded and the $(S/N)_V$ was calculated with the results as shown in Table 13.

VERTICAL SCALE: RELATIVE LIGHT ENERGY
IN APERTURE

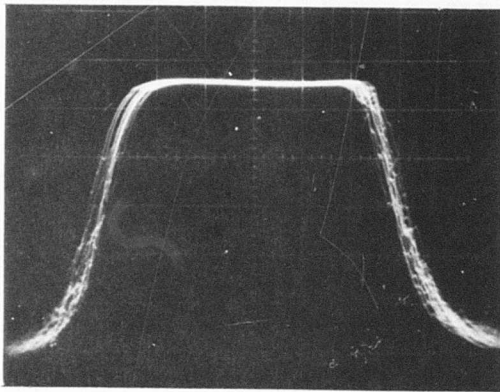
HORIZONTAL SCALE: $34.5 \mu\text{r}/\text{CM}$



(A) 0.25-IN. BEAM DIAMETER
 $95\text{-}\mu\text{r}$ SPOT DIAMETER



(B) 0.75-IN. BEAM DIAMETER
 $66\text{-}\mu\text{r}$ SPOT DIAMETER



(C) 1.5-IN. BEAM DIAMETER
 $54\text{-}\mu\text{r}$ SPOT DIAMETER

Figure 25 Variation of Image Size With Beam Diameter

Table 12. Tracking Error Signal as Function of Beam Diameter

Iris Diameter (in.)	Horiz. Error (mV)	Horiz. Error (μ r)	Vert. Error (mV)	Vert. Error (μ r)	Optical Attenuation (dB)
1.5	6	0.32	5	0.30	50
1.0	7	0.38	5	0.30	50
0.75	7	0.38	6	0.36	50
0.50	11	0.59	8.7	0.53	50
0.25	24	1.30	22	1.33	50
0.125*	27*	1.46*	24*	1.45*	40*

Table 13. Signal-to-Noise Ratios for Various Beam Diameters

Iris Diameter (in.)	Signal Plus Background (μ A)	Background (μ A)	(S/N) _v
1.5	10	0.02	125
1.0	9.2	0.02	119
0.75	4.7	0.02	85
0.50	1.1	0.02	41
0.25	0.1	0.02	12.5
0.125*	0.15*	0.02*	15*

*10 dB Power Increase.

- (4) The horizontal and vertical deflections were calibrated by displaying the video output on an adjustable delay oscilloscope and observing the change in position of the signal on the oscilloscope when a calibrated wedge was rotated in the beam between the transmitting and collecting optics. The calibrations were:

- Horizontal calibration – 34.5 $\mu\text{r}/\text{cm}$ on oscilloscope
- Vertical calibration – 32 $\mu\text{r}/\text{cm}$ on oscilloscope

Oscilloscope traces were photographed when scanning each size of spot over the image dissector aperture and analyzing the pictures. The values found were as given in Table 14.

Table 14. Measured Image Spot Sizes

Iris Size (in.)	Horizontal Spot Size (μr)	Vertical Spot Size (μr)
1.5	54	28
1.0	53	37
0.75	66	57
0.50	69	42
0.25	95	83
0.125	296	200

d. Results and Conclusions

Theoretical tracking accuracy was calculated. (Based on Eq. 4.20, pp 0-47, Vol. III, Ref. 1.) Thus:

$$\text{Tracking Error } \epsilon = 2.36 \frac{\lambda}{D} \left(\frac{S}{N} \right)_p^{-1/2}$$

From this equation, the curve of theoretical tracking noise with constant bandwidth, shown in Figure 26, was calculated. The bandwidth, however, is not constant for the tracking circuitry used but varies with image size as described in the Appendix.

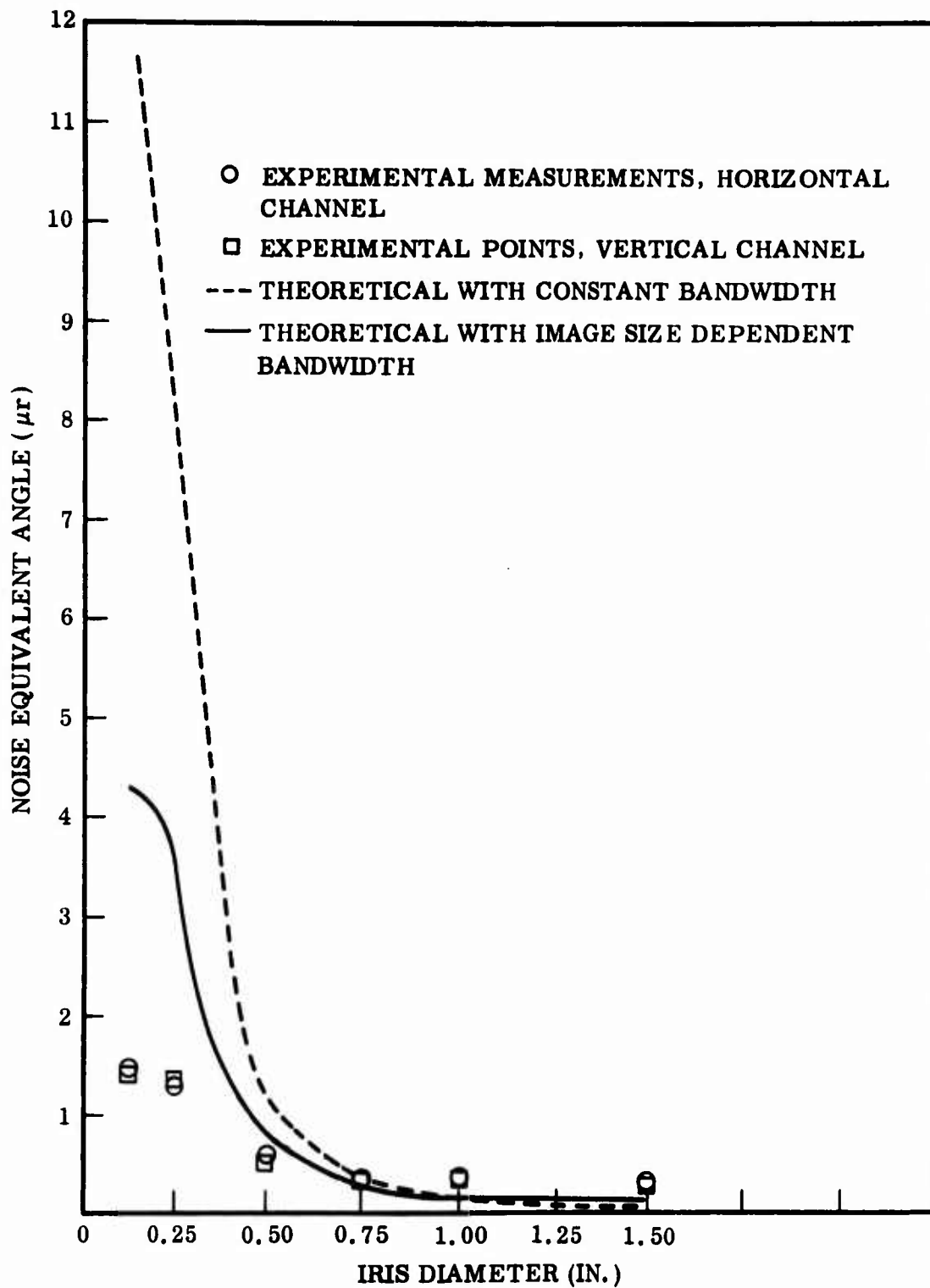


Figure 26 Tracking Noise as a Function of Iris Diameter

The bandwidth used to calculate the S/N ratio in the curve described above was measured with an iris of approximately 1 in. diameter. A curve more nearly describing the physical implementation was determined by considering the bandwidth so that

$$\epsilon = 2.36 \frac{\lambda}{D} \left(\frac{S}{N'} \right)^{-1/2}_p$$

where

D = iris diameter

N' = a function of aperture size, empirically normalized to N for a 1-in.-diameter iris and proportional to D so that N' = ND

Simplification gives

$$\epsilon = 2.36 \frac{\lambda}{D^{1/2}} \left(\frac{S}{N} \right)^{-1/2}_p$$

The result of this curve is given in Figure 26 as "Theoretical with image-size-dependent bandwidth."

The experimentally measured tracking noise is also shown in Figure 26. For an iris diameter of 1 in. or larger, the measured points are within the experimental accuracy expected of either theoretical curve. For a 1/2-in. iris, the measured value is within experimental accuracy for the bandwidth dependent theory but exceeds the constant bandwidth curve. The large difference between the measured noise equivalent angle and the bandwidth dependent theoretical curve for iris diameters of 1/8-in and 1/4-in. indicate that an even stronger bandwidth dependence exists for the very small irises. This is reasonable since the very large image and low signal levels for these cases place them outside the AGC operating design region. Measurements for these very small iris diameters were not originally included in the test plan but were added during testing because they may be of value in determining characteristics of operation outside the normal AGC range.

For large iris diameters, the experimental values are a little larger than predicted by the theory. This is thought to be caused by a combination of two effects. First, the energy is concentrated in the center of the iris with nearly an order of magnitude greater energy density at the center than at 1 in. from the center. Also, for the larger apertures, circuit noise is significant. This explanation is supported by the fact that the experimental values are approximately constant for apertures larger than 0.75-in. diameter.

The theoretical spot size as a function of iris diameter was calculated and is shown in Figure 27. The curve is weighted to give spot size for 10-percent intensity of an Airy distribution to enable direct comparison with the measured values. The measured values are displayed on the figure, and they show reasonable agreement with the

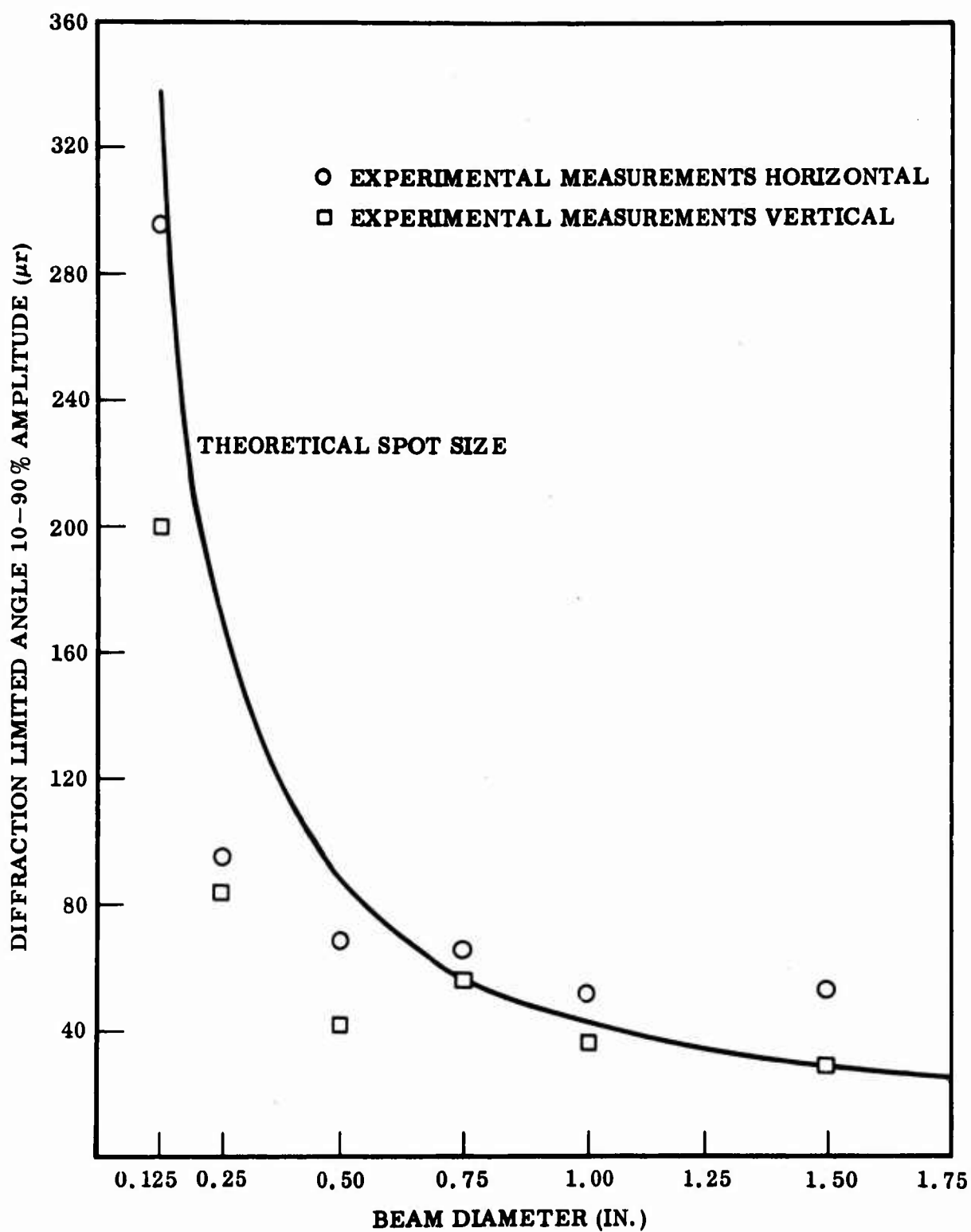


Figure 27 Spot Size as a Function of Iris Diameter

theoretical curve. The following test results indicate areas for improvement in advanced systems with larger optics:

- Improved optics should be used to produce a more even distribution of energy across the beam.
- Circuit noise should be reduced. The fine gimbal position sensor appears to be the major culprit in the existing equipment.
- There should be further evaluation of the best type of AGC to use.

5. MIRROR CONTROL LOOPS

a. Fast Steering Mirror Control Loop Frequency Response

(1) Laboratory Tests. The purpose of this test was to determine the fast steering mirror control loop 3 dB bandwidth. The control loop bandwidth was measured by inserting a constant amplitude sinusoidal signal at the input to the fast steering loop and monitoring with an oscilloscope the system response to this injected sine wave. By increasing the frequency of the test oscillator and recording the system response, the frequency at which the response was down by 3 dB was determined.

Figure 28 was plotted from the data collected during this test. The 3-dB bandwidth was determined for both the horizontal and vertical channels. As indicated on the graph, at low frequencies (up to 100 Hz) the system responded with an expected gain of unity. Although the plot of V versus frequency begins at 1 Hz, the frequency was decreased to 0.1 Hz during the test. At this low frequency the gain was still unity.

Above 100 Hz, the gain decreased at a rate of approximately 20 dB/decade (6 dB/octave).

(2) Results and Comparison with Predicted Performance. As indicated on the graph, the horizontal channel 3-dB frequency is 350 Hz, and the vertical channel 3 dB frequency is 270 Hz. These values are within an acceptable $\pm 20\%$ of the planned 300 Hz bandwidth.

b. Fast Steering Mirror Control Loop Transient Response

(1) Laboratory Tests. The purpose of this transient response test was to measure the fast steering mirror control loop system stability. This was accomplished by injecting a 5.3-V (p-p) square-wave signal into the closed loop summing point at two different frequencies, and then measuring the system response. The measurement was performed by photographing the response of the system displayed on an oscilloscope and reading the response data from the photograph.

Figure 29 was taken with a 50-Hz signal input. The rise time and time delay were measured from this photograph. The figure also illustrates the amount of overshoot with respect to the signal amplitude.

The Figure 30 photograph reflects a 20-Hz signal input. From this photograph, the percentage overshoot, the settling time, and the frequency of damped oscillation were determined.

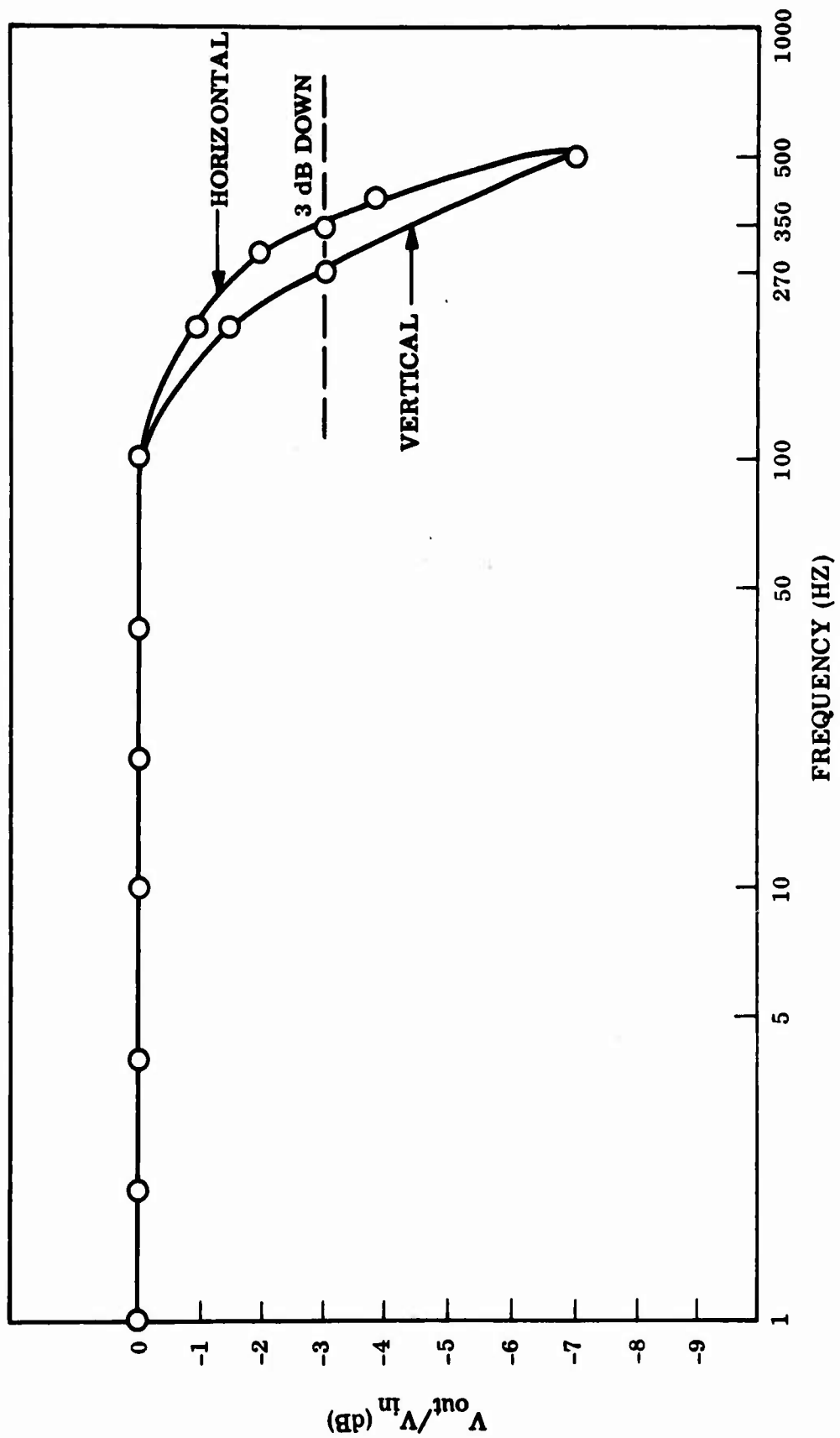


Figure 28 Frequency Response of Fast-Steering Mirrors

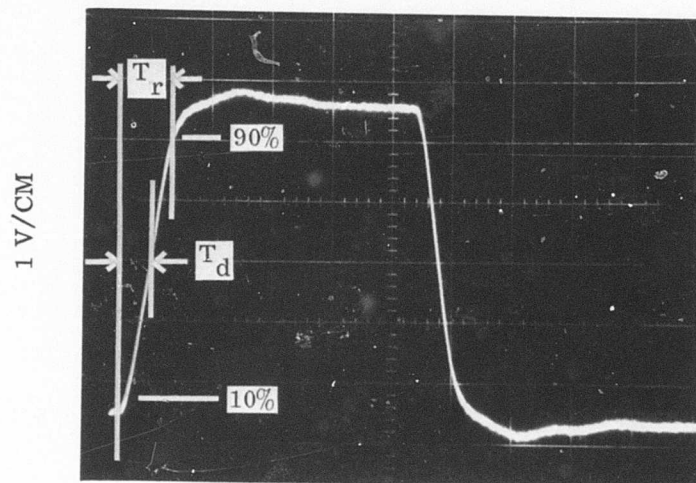


Figure 29 Mirror Response to Square Wave Input (50 Hz)

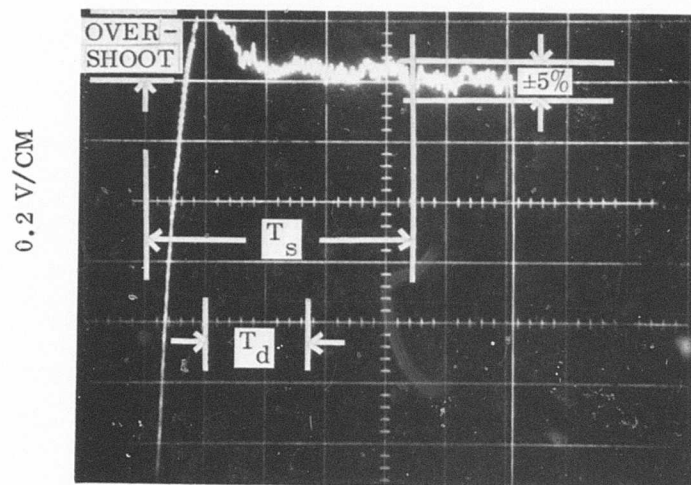


Figure 30 Mirror Response to Square Wave Input (20 Hz)

(2) Results and Comparison with Predicted Performance. The results of the transient response test are tabulated in Table 15.

Table 15. Transient Response of Fast Steering Mirrors

Time-Domain Specification	Measured Value	Figure
Rise Time, T_r (10% to 90%)	1.4 ms	29
Time Delay, T_d (response to reach 50% of final value)	0.6 ms	29
Percent Overshoot $\left(\frac{\text{max. overshoot}}{\text{final value}} \times 100 \right)$	4.2%	30
Settling Time, T_s (within 5% of final value)	17.5 ms	30
Frequency of Damped Oscillation ($1/T_o$)	256 Hz	30

Comparing the data above with that of a classical second-order linear system, it can be concluded that the tracker system with the fast steering mirrors is a stable system. This statement is indicated by the amount of overshoot for a large step input. The 4.2 percent overshoot for the system corresponds to a damping ratio of approximately 0.72 for a second-order system. The designed damping ratio was 0.7.

c. Gimbal Mirror Response, Stability and Effect on Tracking – Test 5.3

(1) Evaluation Steps. The performance of the gimbal mirror was evaluated in three steps. First, the response of the system was measured including the open and closed loop frequency dependencies as well as the response to a square wave. Second was an investigation of the extent to which table acceleration during a rotation-reversal affected tracking accuracy. Finally, loop stability and error sensitivity were measured under a simulation of severe agile mirror deflection conditions.

A natural frequency of the gimbal mirror near 30 Hz was obtained with inertias of either 0.03/ or 0.3 oz-in./sec², the latter was representative of the SDRS, and the former was a much more difficult test condition. Table acceleration much greater than that encountered in space produced only a one microradian increase in tracking error. In the final test, an agile mirror deflection of 0.175 rad. peak-to-peak was simulated by injecting a triangular error signal. Continuous gimbal tracking was still maintained. The sensitivity of tracking error to agile mirror motion was verified in this final test.

(2) Gimbal Mirror Response - Test 5.3.1. The open loop response of the gimbal compensation amplifier as a function of frequency was determined from the variations of gain between the signal input from the fine steering mirror position, and the output of the torquer amplifier driving the gimbal mirror. The closed loop frequency response was determined from the tracker mirror position output. A square wave error signal was injected to observe transient response. The interface points are shown in Figure 31. Figure 32 shows the open loop gain of the gimbal compensation amplifier. Below five Hz, the gain is constant at 14, with a gain proportional to the frequency between 10 and 100 Hz. Break points are at 7, 110, and 650 Hz.

The inertia of the gimbal introduces into the loop a response characteristic which falls off as $1/f^2$. The compensation amplifier has its gain designed to increase proportional to frequency in the region from 10 to 130 Hz. Thus the net response in this frequency range will be a fall-off proportional to $1/f$, or 6 dB per octave, in the neighborhood of the frequency where the closed-loop gain drops to unity. This is a desirable condition for stability of the loop.

The basic gimbal had an inertia of $0.03 \text{ oz-in.-sec}^2$. Weights could be added to bring it up to the normal inertia of 0.3 oz-in.-sec^2 . Tests were made under both conditions. The large inertia was used to determine typical operating performance and the smaller inertia, being more responsive to transients, gave more insight into the influence of perturbations.

The closed-loop frequency response of the gimbal mirror is given in Figure 33 for the nominal inertia of 0.3 oz-in.-sec^2 . The response shows a quite satisfactory frequency response with a bandwidth in the vicinity of the planned 30 Hz and a satisfactory phase shift.

(3) Tracking Accuracy During Table Reversal. The most severe effects of the gimbal mirror on tracking accuracy were expected to be transients of acceleration during reversal of direction during a simulated limit cycle. In this test the increase in tracking and pointing errors due to the reversal in direction of the table were measured. In space the maximum angular acceleration to be encountered is around 0.01 rad/sec^2 . A value of 0.07 rad/sec^2 , given on page 3-156 of Reference 1, was for an early Agena, and 0.01 rad/sec^2 is more representative of current space vehicles. In this test larger accelerations were produced. Nevertheless, tracking was maintained during the reversals, and the increased tracking and pointing errors were as predicted. See Section III, 4.j. (5).

Acceleration was measured with an Endevco QA-116-16 accelerometer with a sensitivity of 1 V/G. The accelerometer was mounted near the perimeter of the table and measured the linear acceleration at that radius. The output voltage was monitored on an oscilloscope. The photograph in Figure 34 was taken by opening the shutter before a reversal, then closing it afterward. The $\pm 20 \text{ mG}$ bright area is the result of over exposure due to several sweeps and to accelerations from the vibrations of the drive motor. The peaks showing above and below the vibration signal after the initial reversal are torsional oscillations of the table following the shock of reversal. Since the camera shutter was open for a time on the order of a second, in order to catch the instant of reversal, several oscilloscope traces are superimposed, and a time relationship between peaks cannot be established.

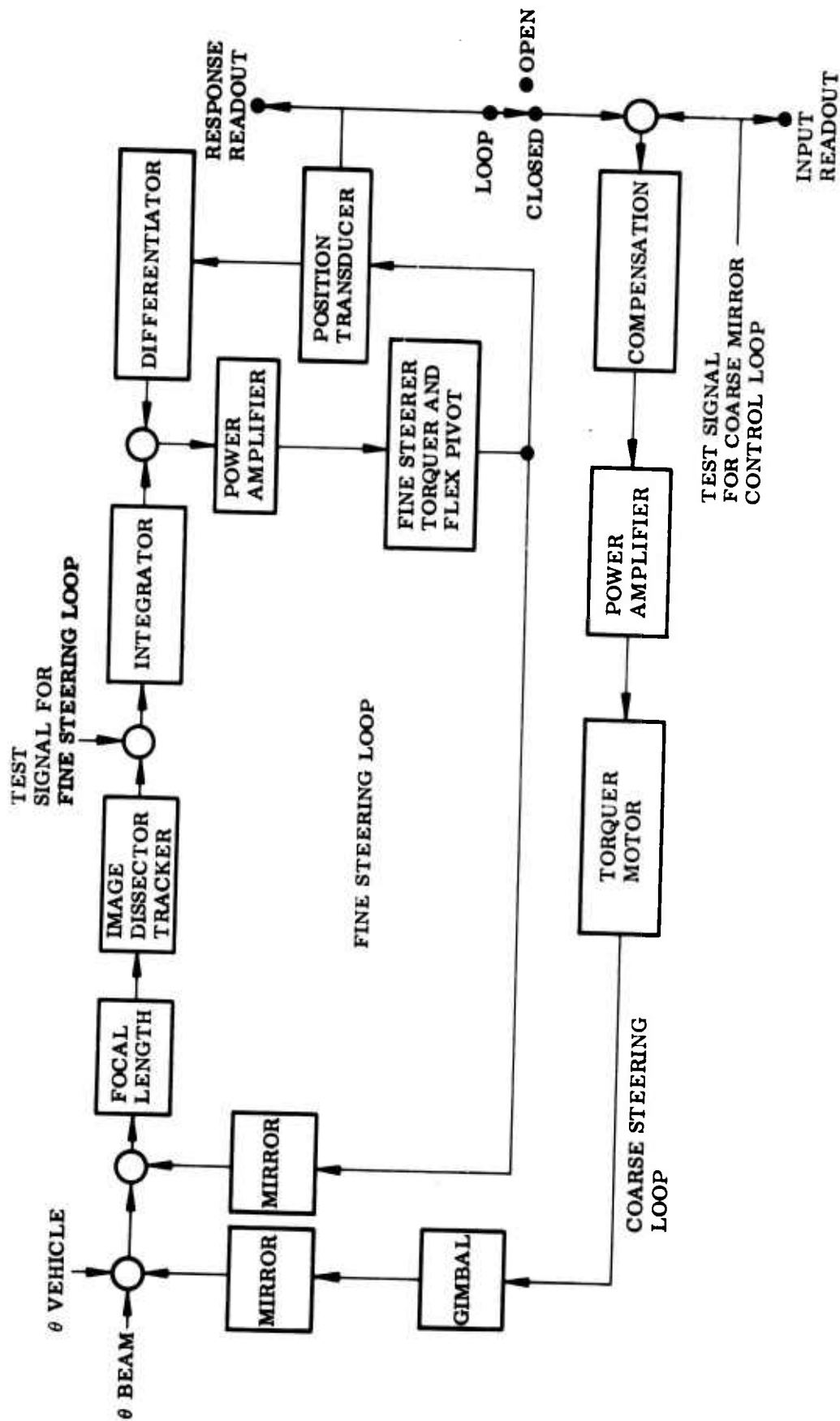


Figure 31 Component Relationship in Tracking Mode

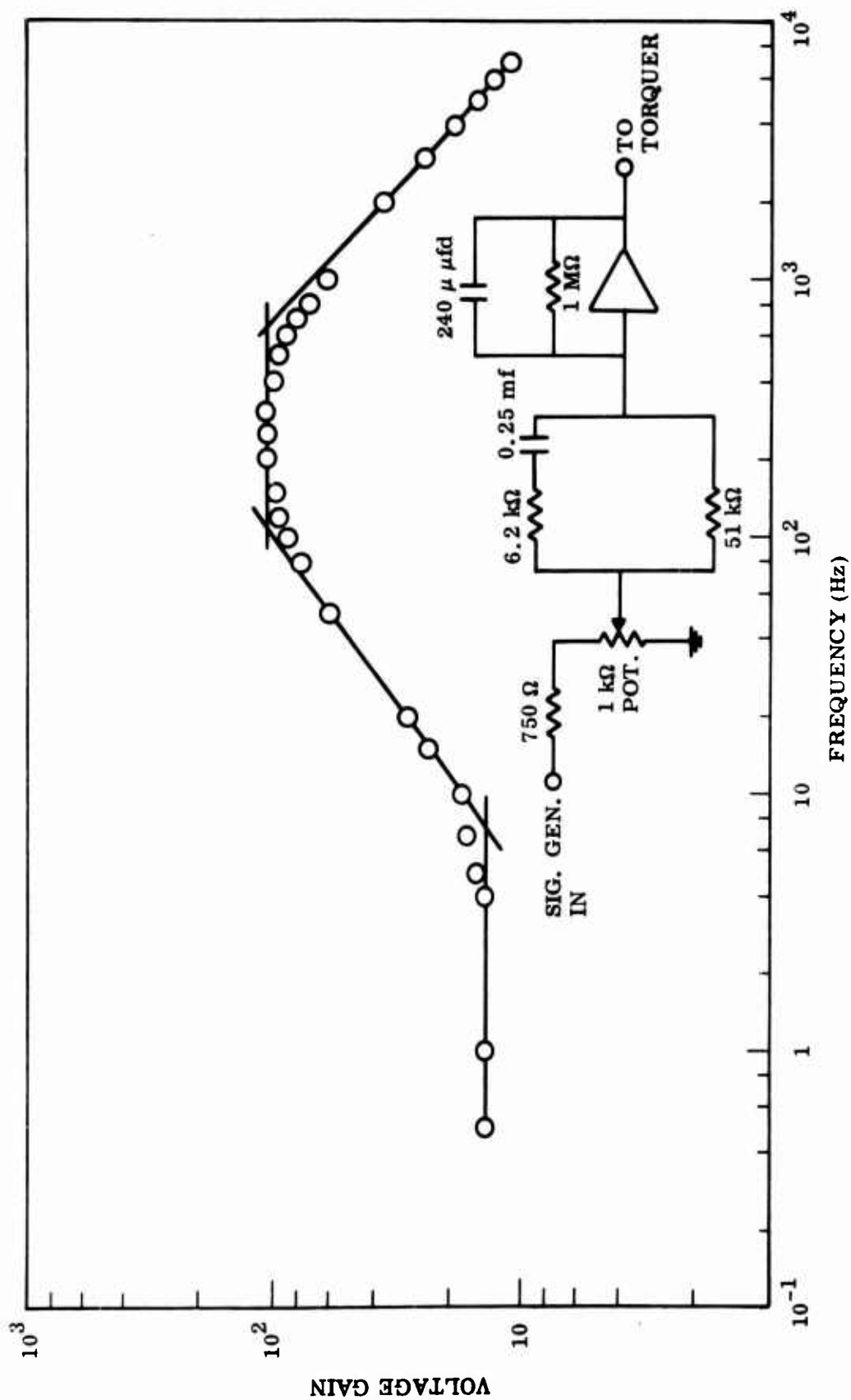


Figure 32 Frequency Response of Torquer Driver Circuit Used With Full Inertia Mirror Assembly

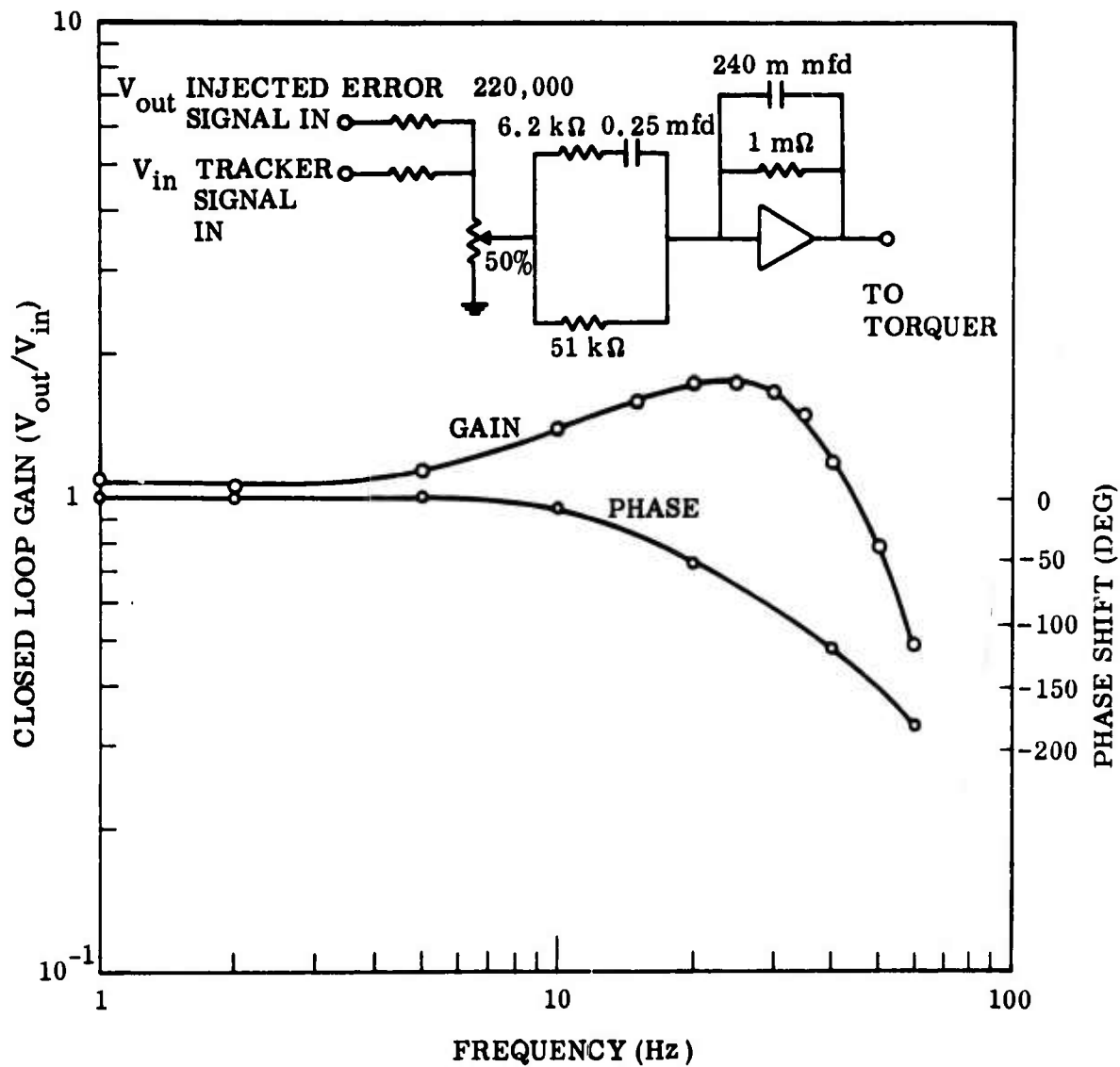


Figure 33 Closed Loop Gimbal Mirror Frequency Response With Full Inertia Mirror Assembly

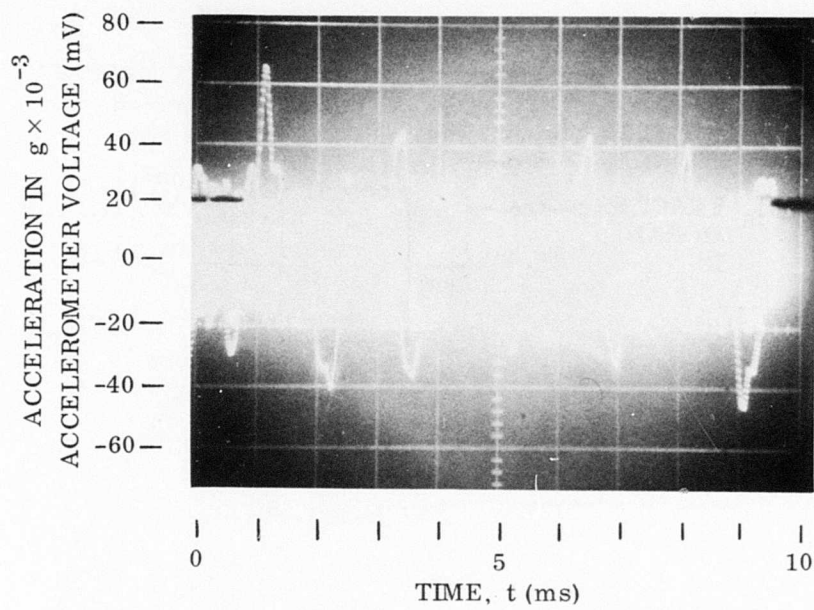


Figure 34 Accelerometer Output Voltage During Table Reversal

The peak acceleration of the linear accelerometer during the typical reversal shown is 63 mG with several subsequent oscillations, of accelerations up to 40 mG. These values correspond to 1.4 and 0.9 radians/sec² angular acceleration, respectively, somewhat greater than expected under space conditions.

Figure 35 shows the pointing and tracking errors and the current through the gimbal torque motor. The abrupt changes in torquer current indicate table reversals. The shape of the current recording shows that there is a dominant friction force, presumably magnetic hysteresis, which increases with the amount of gimbal rotation. From the recorded data it is seen that the drag reaches 0.032 oz-in., which is a reasonable 0.5 percent of the motor maximum torque of 6 oz-in.

The pointing errors have components at the rate-table frequency. For the horizontal component this was due to varying truncation of the beam as the table rotated and was later reduced by realignment of the pointing beam to minimize truncation (Figure 42). Pointing error data were taken from Figure 36 with an expanded time scale.

The errors in pointing and tracking due to reversals are taken only for the horizontal axis since this one only involves the gimballed mirror. Peak errors are difficult to read with precision on the recordings but appear in horizontal to be around 2.5-microradian peaks in both pointing and tracking. The errors persisted through a period of approximately 0.7 sec, probably as a result of the observable shock-induced oscillation of the table top, with the drive coupling acting as a spring. The 2.5-microradian peak error compares with the predicted error (page 45) of 2 microradians, which is fair agreement considering the accuracy of the readings.

6. POINTING ACCURACY, BORESIGHTING AND POINT-AHEAD - TEST 6

a. Discussion of Error Sources

These tests were to determine the maximum accuracy of pointing attainable with given signal and background levels and the ease and accuracy with which boresighting and point-ahead could be accomplished. Pointing accuracy is dependent on several factors:

- Tracking error in the pass-band of the fine steering and the gimballed mirrors
- Tracking error due to beacon angle noise above the F.S. response
- Boresighting error between the image dissector and the pointing laser
- Angular noise in the pointing laser
- Angular noise in the beacon laser
- Effects of atmospheric and mechanical disturbances not affecting pointing and tracking equally
- Noise in the pointing detector

Of these error sources, atmospheric and mechanical disturbances were most significant. Before any other errors could be evaluated, elimination of external sources of error and particularly shielding the optical paths from air currents was necessary. Without the shields, peak pointing noise of tens of microradians was observed, as shown in Figure 37.

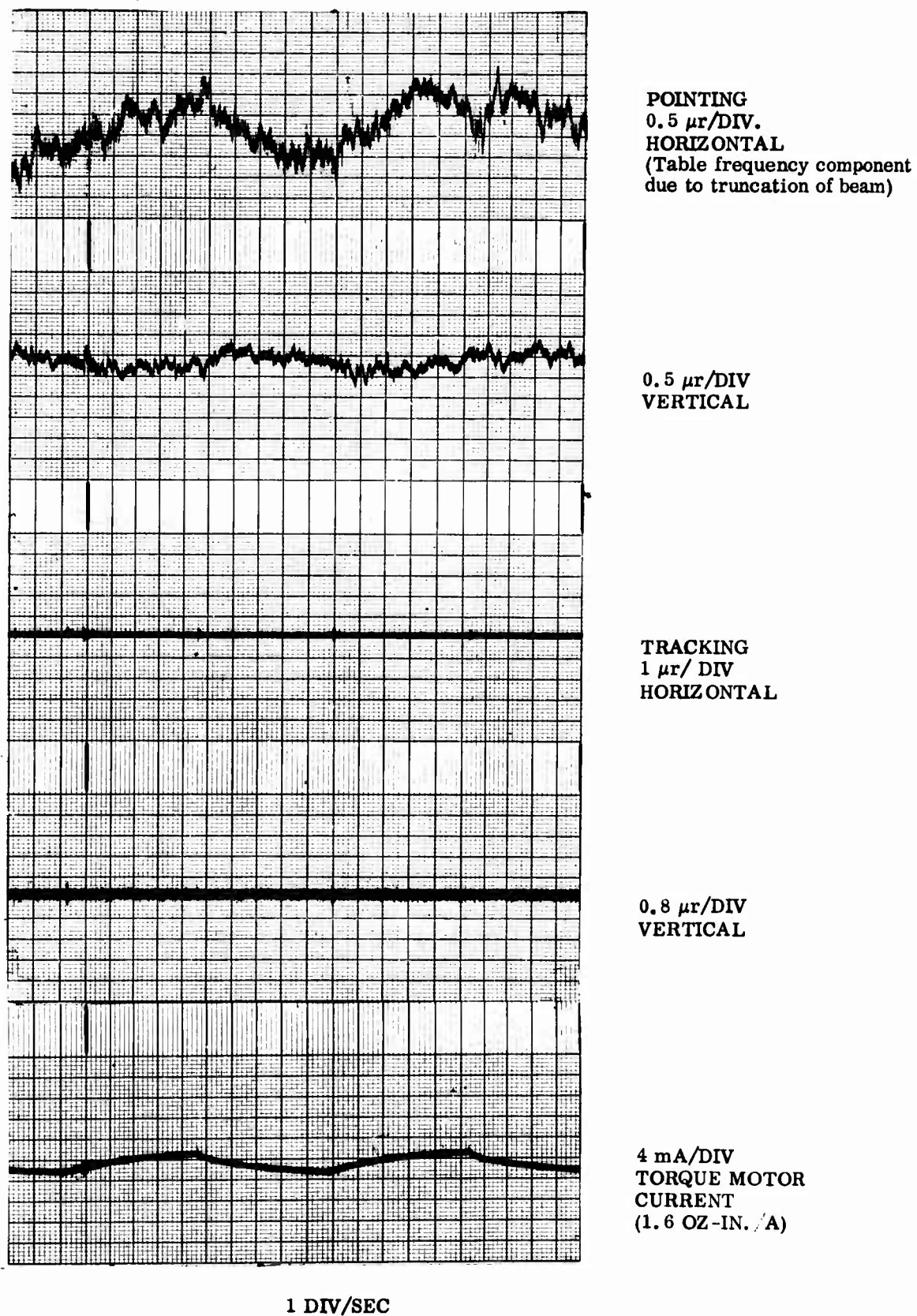


Figure 35 Pointing and Tracking Errors and Torque Motor Current With Table Rotation and 0.3 oz-in.-sec^2 Inertia

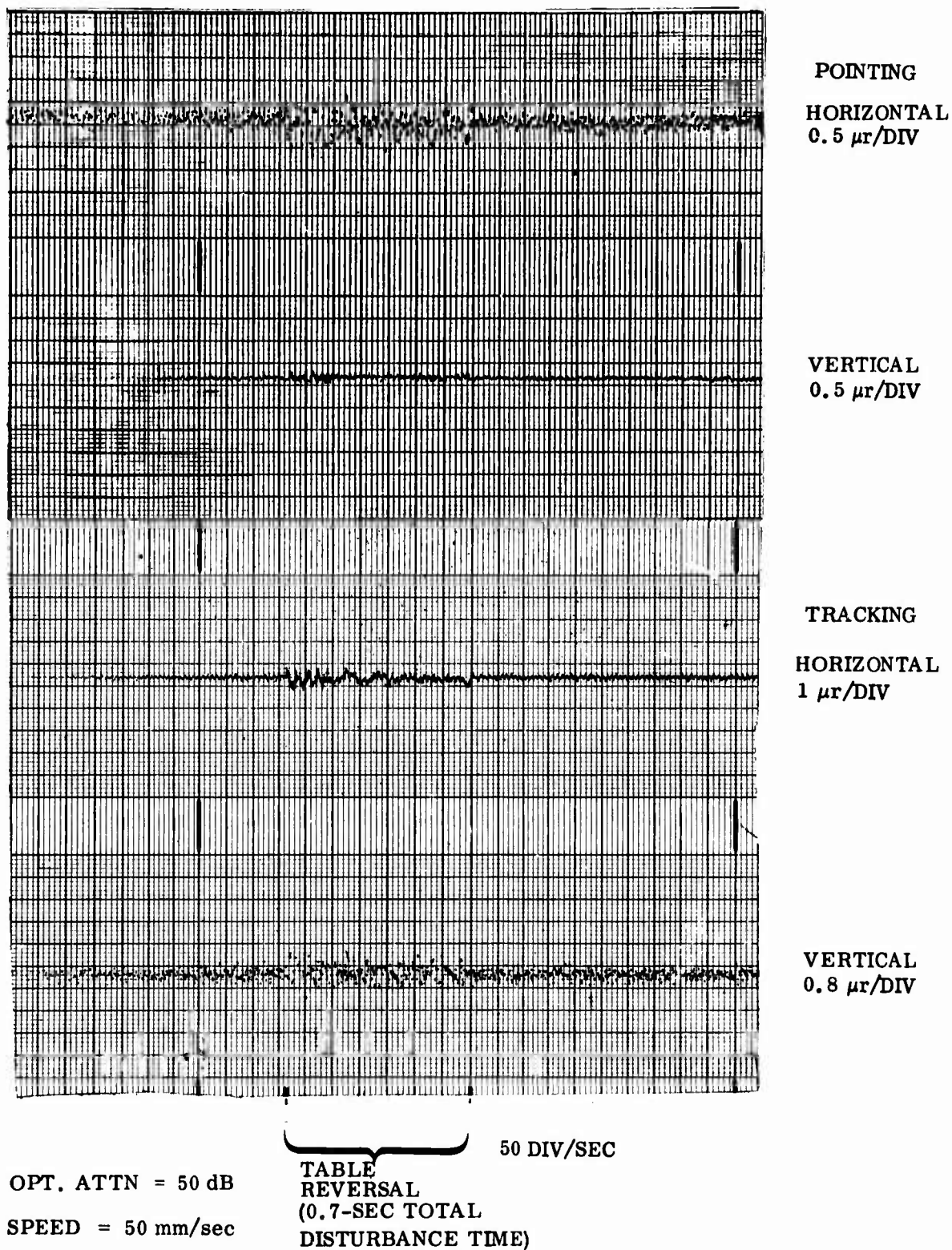


Figure 36 Pointing and Tracking Errors in an Expanded Time Scale

With air shields, the value dropped to less than 1 microradian rms when pointing with tracking circuitry disabled. Because mechanical disturbances were easily observable with any touching of the optical table or the components on it, tests were conducted remotely so there was no need for physical contact with the table during the actual taking of test data.

Noise in the pointing detector was evaluated by illuminating the quadrant detector with a uniform illumination giving the same total detector current as produced by the pointing laser signal. The noise level under this condition was undetectable; its angular equivalent was far below 1 microradian. Noise in the pointing laser was measured by retroreflecting the signal to the image dissector, tracking the signal and measuring the rms noise with the Ballantine RMS Voltmeter. The measured value was 3 microradians rms. Due to the magnification of the telescope, this 3 microradians became 0.26 microradians in the pointing detector space. Consequently, the contribution of the pointing laser noise was small, but not negligible.

Several other pointing noise sources were noted. The construction of the system was not conducive to correction of long-term thermal or electrical drifts except in the case of a large angular drift rate in the pointing laser when first turned on. This drift decreased to the value stated above after an hour to an hour and a half of warmup. Any residual laser noise might have been eliminated with a spatial filter but none was on hand.

Power line frequency noise and its harmonics were sometimes detectable in the most sensitive measurements but were not found to be of sufficient magnitude to justify further effort in their removal.

As a practical matter, all pointing shifts with periods greater than a few seconds are probably due to thermal shifts in optical components or thermal or electrical drifts in electrical components. The equipment was not expected to be free from such shifts since no great effort or expense had been made to eliminate them. Consequently, long period variations were ignored in evaluating the dynamic performance of the pointing. Such drifts do not affect the measured tracking error since the fine steering mirrors maintain the tracking error near 1 microradian through quite violent perturbations.

Boresighting error did not enter into the pointing measurements except in the specific instance of determining how accurately boresighting could be accomplished. Normally, an arbitrary pointing zero was established and then variations in the pointing were recorded throughout a test. One reason for not boresighting the pointing laser to the beacon was to keep the pointing HeNe laser signal from interfering with the beacon HeNe laser signal at the image dissector. The other reason was to avoid time consuming and repetitious boresightings made necessary because the mechanical structure could not be counted on to hold 1 microradian accuracy from day to day.

All of the above factors, except tracking error, are independent of the tracking system. They were measured in sum total by observing pointing noise with the tracking system inoperative. On the horizontal axis, the rms of the resultant pointing noise was 1.1 microradians. This value is not unreasonable for the equipment being tested but would be excessive by a factor of about 3 in an operational system. It is believed that the biggest contributor to the noise is atmospheric turbulence. This would be non-existent in space. It can be further reduced in laboratory tests by more extensive

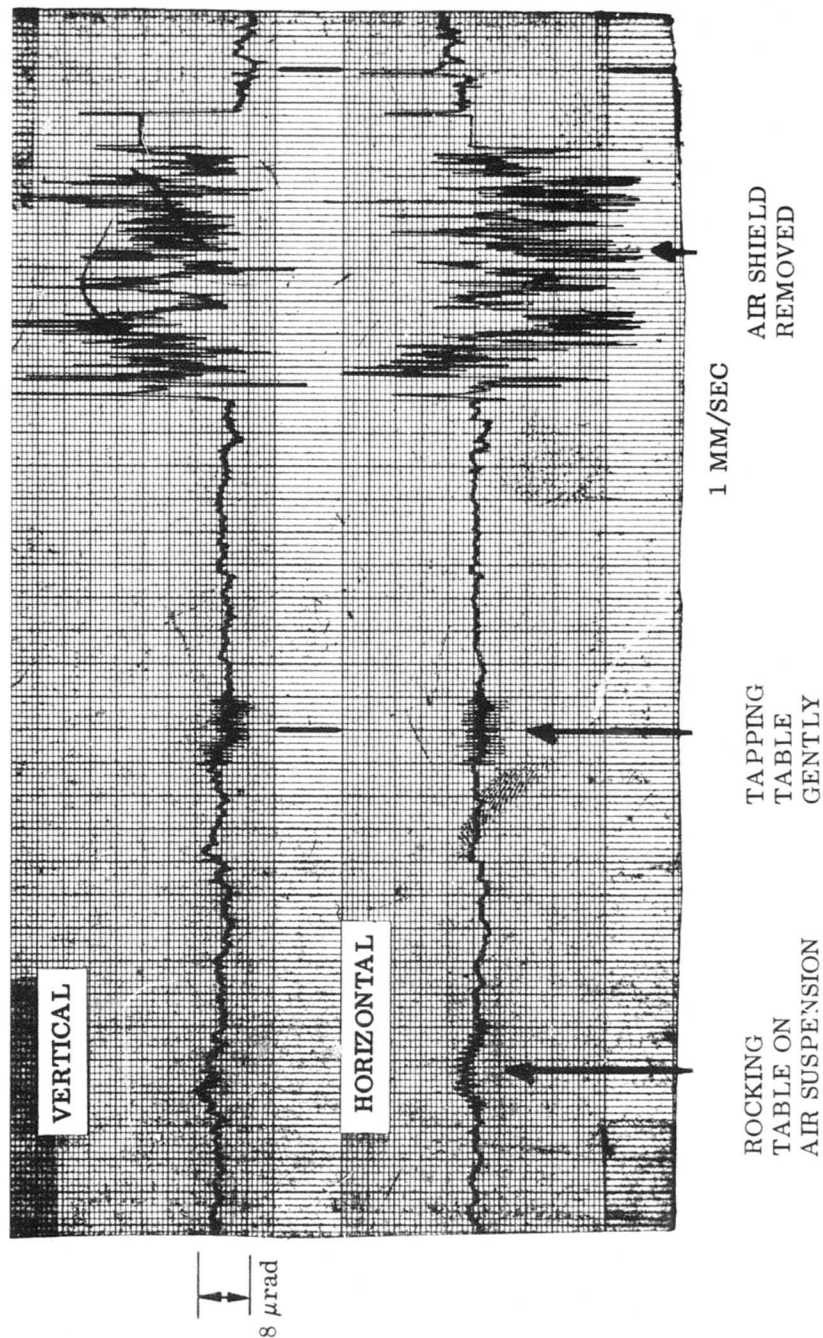


Figure 37 Effect on Pointing Due to External Disturbances - No Tracking Operation

shielding of the optical paths, including double shielding and the elimination of heat sources within the shield enclosures. Pointing laser noise, (0.26 microradians rms amplitude) can be reduced by a spatial filter on the pointing laser output. Mechanical noise could be much lower than existed in the laboratory by use of a better isolated table, greater care in running leads to the equipment, more sturdy mounts for components, and reduction of acoustical noise in the test room.

b. Noise Spectra

During the test program, a Fourier analyzer became available. It had the capability of analyzing the distribution of energy in a signal when observed over a period of time. Measurements were made of the distribution of the noise in the tracking and pointing signals both with and without the fast steering mirrors operating.

The results obtained may not be an exact portrayal of conditions for an operational tracking and pointing system because of the presence of various sources of noise which will be reduced or non-existent in a communication system. Nevertheless, the results are highly instructive.

Noise in the pointing system is shown by Figure 38. When not tracking, the pointing noise peaks at about 1/4 Hz, falls off quite rapidly toward lower frequencies and drops smoothly to 17 dB down at 100 Hz and to 31 dB down at 1000 Hz. This noise is thought to be mostly due to turbulence and pointing laser noise. The effect of tracking, as shown by the dotted line, is to reduce the noise below 18 Hz, to increase it to 300 Hz, and then drop it sharply. This agrees with data shown later on the strip chart recorder and shows the low frequency turbulence being tracked out and the beam-steerer transducer noise being added. The tracking spectrum in Figure 39 is somewhat similar. It peaks at a slightly higher frequency, (around 1 Hz), falls off at about 10 dB at 25 Hz and then is irregularly flat out to 8,000 Hz where it drops very sharply as the result of a filter in the image-dissector error detector. One can easily visualize this to be the sum of a spectrum, similar to the pointing spectrum and a rather flat shot-noise in the image dissector.

As with the pointing, but much more so, the tracking error is attenuated below 30 Hz and increases to a peak at 300 Hz with a rapid falloff above. Strip chart recordings confirm the large attenuation at low frequencies and the increase at the higher end. The result was a substantial reduction in the tracking error as will be shown in section c following. The substantial increase in noise at the higher frequency end may not be typical of tracking systems since it largely stems from noise in the position transducers which read the position of the fine steering mirrors and supply a rate feed-back signal. A valuable result of these tests has been to pinpoint the transducers as weak links in the performance chain and to lead to the development of a more promising approach, not tested here, for obtaining the position and rate signals.

c. Pointing Accuracy Measurement

Pointing accuracy was measured first with the fine steering mirrors, the gimballed mirror, and the table inoperative, in order to evaluate the noise unrelated to tracking in the pointing error signal. These units were then turned on to observe their effects. The effect of the fine steering mirrors was to reduce low frequency error, such as

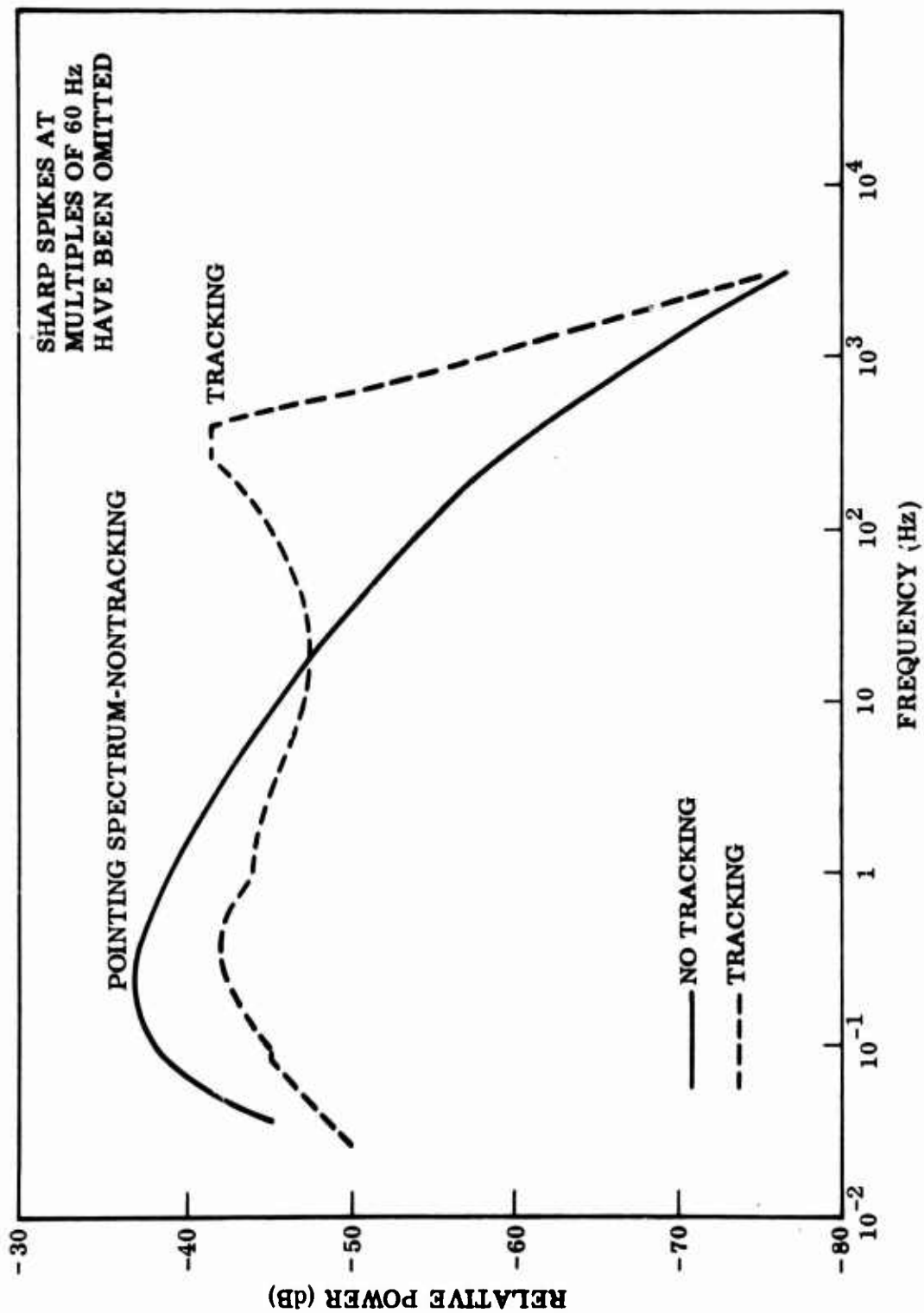


Figure 38 Pointing Noise Spectrums

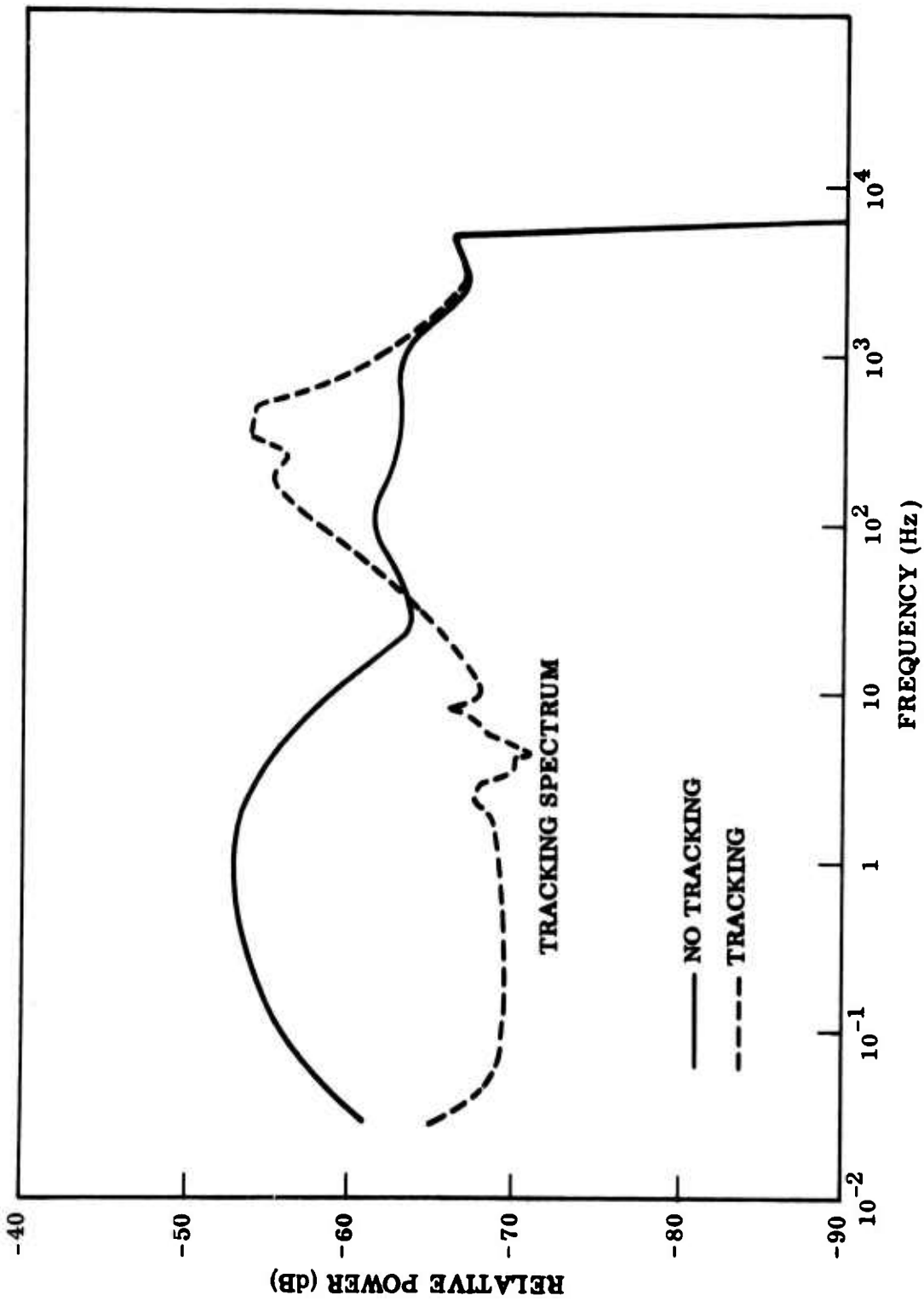


Figure 39 Tracking Noise Spectrum

that due to atmospheric disturbance effects (Sec. IV 10) but to add that due to image dissector shot noise and position read-out noise. Operation of the gimballed mirror and table also increased the noise slightly. Pointing accuracy was measured, at two signal and two background intensities. The lower signal intensity was as near the minimum level projected for tracking in space (2.8 dB above the minimum level) as component values permitted. At the lower signal intensity two different background intensities (Cases I and II) were used. The larger background intensity and low signal intensity (Case II) gave the same signal-to-noise ratio as encountered under worst-case threshold conditions in space, 0 dB S/N margin. This should yield pointing performance representative of the worst case. Increasing the background level increased the noise, as expected.

The summarized RMS pointing and tracking errors are given in Table 16. The static error values, obtained with the mirrors and the table immobile, are found from Figure 40, and show the basic tracking and pointing noise levels without beam-steering. Figure 41 shows the change brought about by the fine steering mirrors. They reduce low frequency error, but increase high frequency error. The vertical tracking signal shows more noise as the result of its not being as well optimized as the horizontal channel electronics. The vertical channel had no gimbal and was not a representative axis for evaluation. The dc shift when the mirrors are activated is due to their position pickoff nulls not being aligned with the mechanical rest position. This causes the image dissector to develop a bias signal when the beam-steerers are inoperative.

In Figure 42, the pointing traces show an increase in high frequency noise but no decrease in low frequency noise. However, under proper conditions, the pointing beam did benefit significantly from the fine steering mirror's compensation of atmospheric effects. This is considered in more detail in Section IV, 10. Pointing and tracking traces with all systems operative are shown in Figure 43. Although there is an increase in noise due to gimballed mirror and table activation, it is not a large change, as may be seen from the numbers in Table 16.

In space, the lowest signal intensity and highest noise conditions that are expected to be encountered are for a synchronous satellite to low orbit satellite link. If no margin were allowed, the current at the anode would be 5.8×10^{-7} A due to the signal, with 1.26×10^{-7} A due to background radiation which were the desired values for the evaluation tests. The available neutral density filters provided attenuation only in multiples of 10 dB. Thus the nearest experimental approach to space conditions was 1.8×10^{-6} A anode current for the signal. Two background intensities were used. One was the ambient background, which gives a low 2×10^{-12} A anode current. The other, adjusted to give 3×10^{-6} A anode current, was chosen to give exactly the same signal-to-noise ratio (0 dB S/N margin) as exists for the worst-case satellite condition.

The tests at higher signal levels, were conducted with the low inertia gimballed mirror - a more-stringent-than-normal condition. The lower signal intensity tests were conducted with the full inertia gimballed mirror, representing the normal operating condition. The trace for no added background was given in a previous section as Figure 35. The trace with added background appears essentially the same, but the Ballantine RMS meter showed the slight increase in noise shown in Table 16. Continuous tracking was achieved even during table reversal, under all of the above conditions.

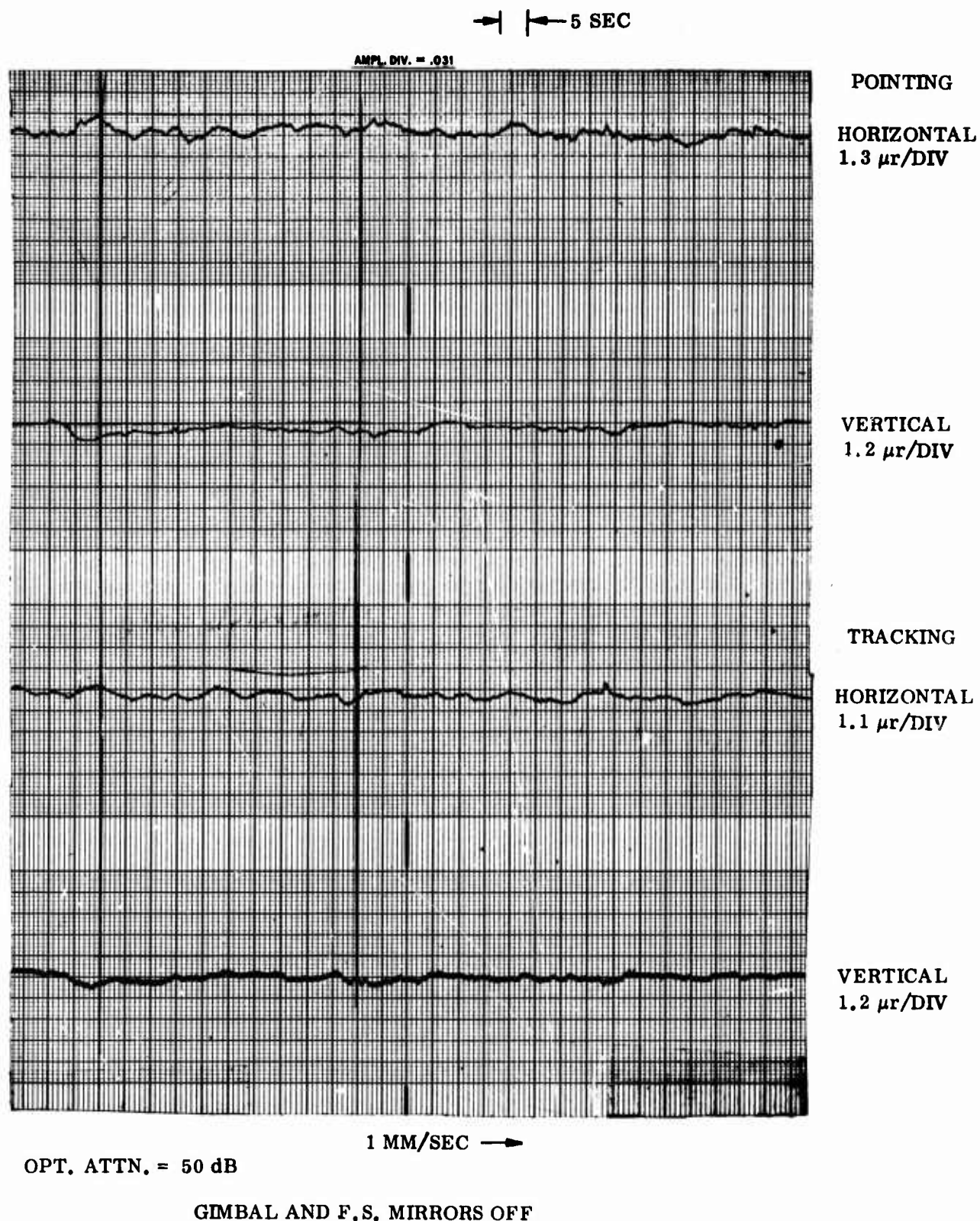


Figure 40 Tracking and Pointing Errors With All Mirrors and Table Off –
Signal Current of 1.8×10^{-5} A

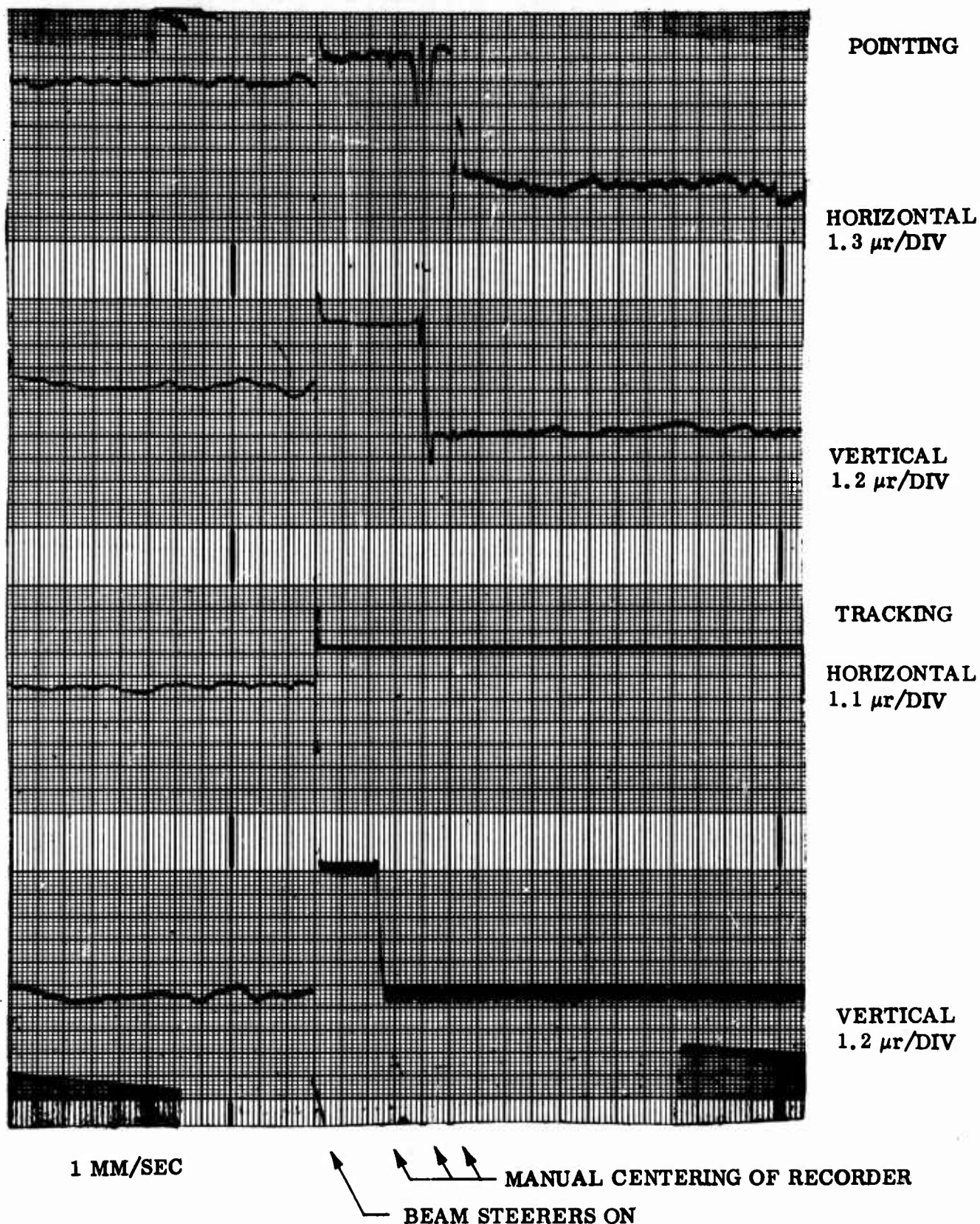
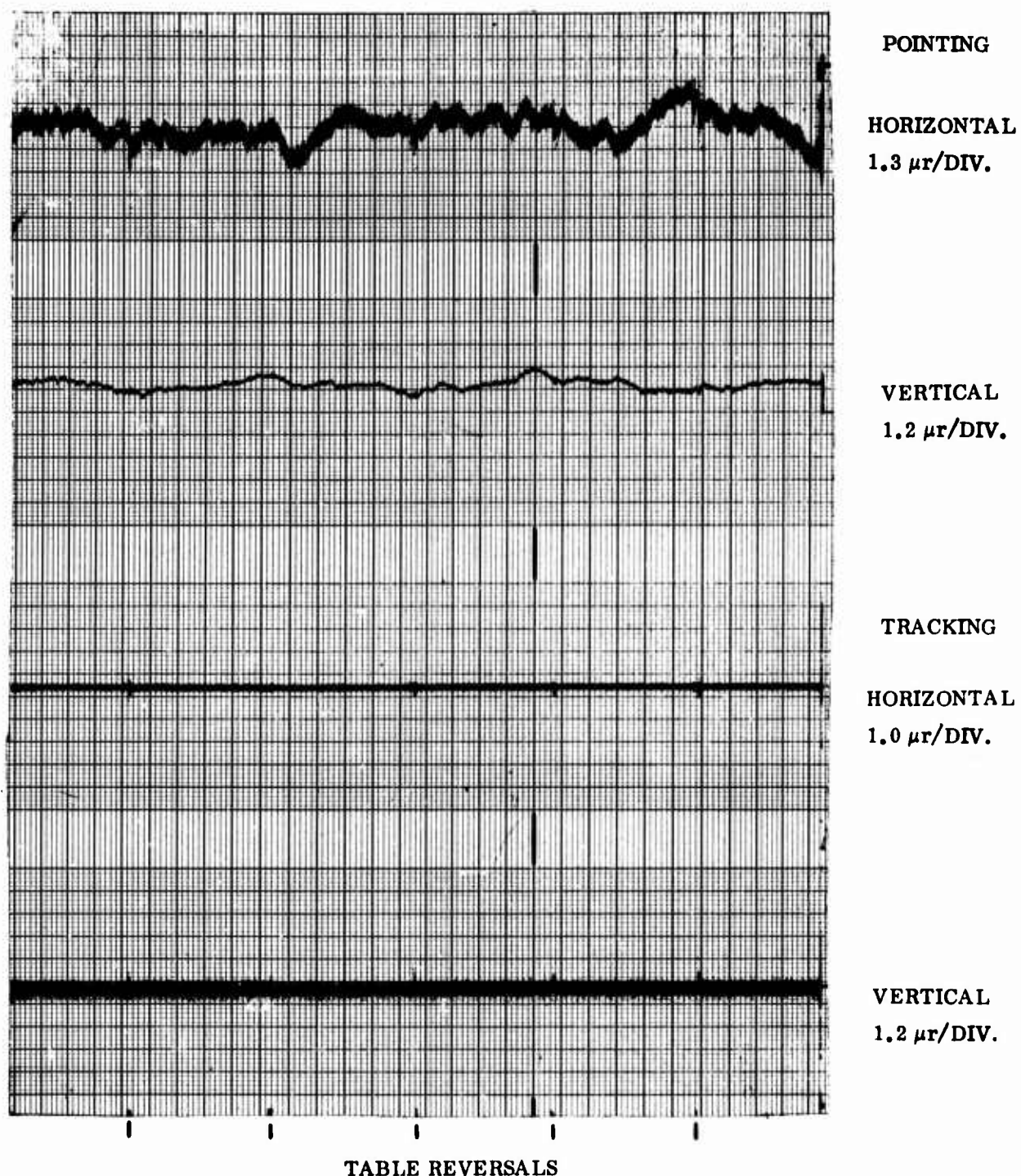


Figure 41 Tracking and Pointing Signals With Gimballed Mirror and Table Motionless and With Fast Tracking Mirror First Off and Then On - Anode Current 1.8×10^{-5} A. Misalignment of fast-steering mirror mechanical and electrical nulls causes dc shift



OPT. ATTN. = 50 dB
11 μA I.D. ANODE CURRENT
1 MM/SEC

Figure 42 Pointing and Tracking Signals With All Systems Operational –
Signal Current of 1.1×10^{-5} A at ID Anode

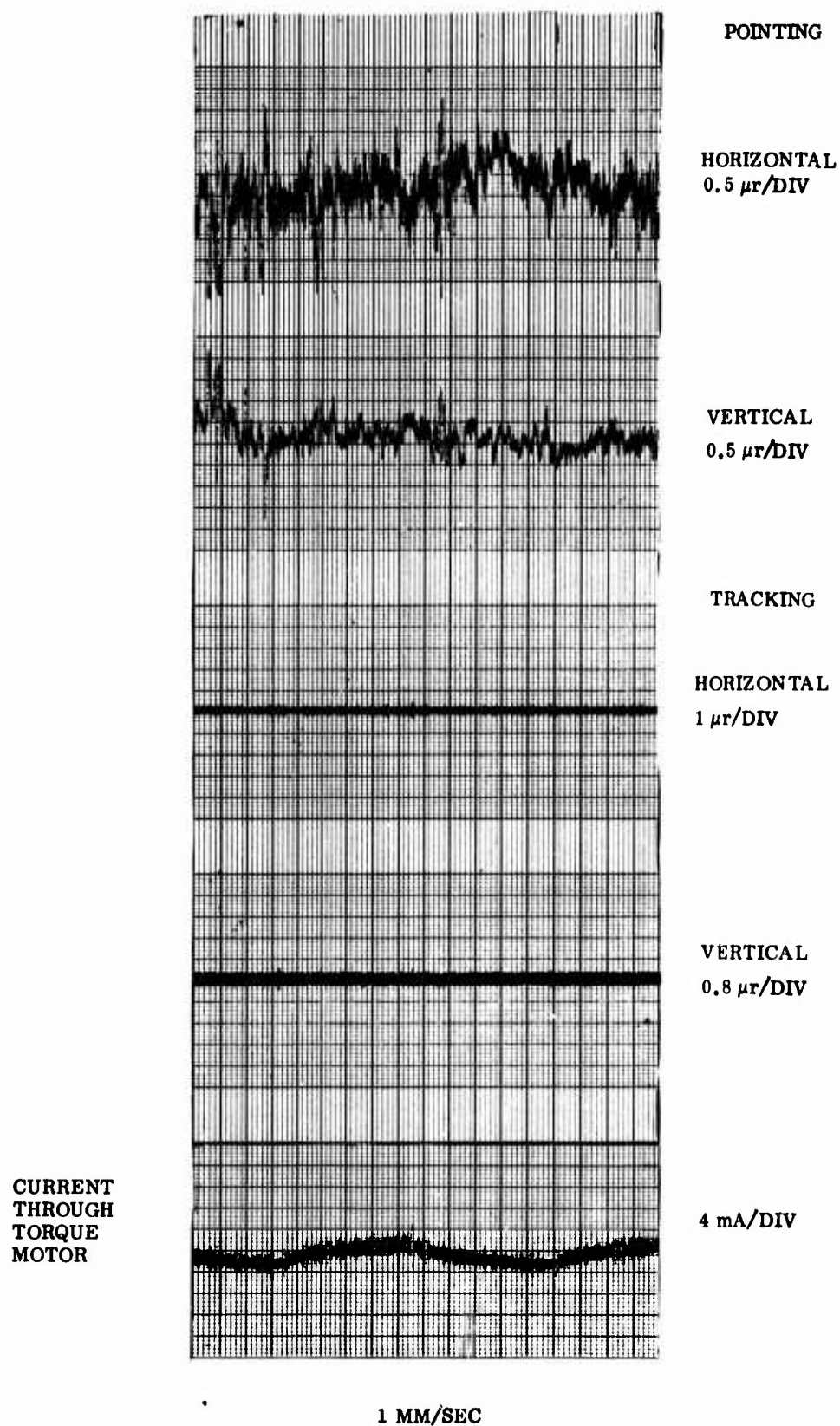


Figure 43 Pointing and Tracking Errors and Gimballed Mirror Current With Full Inertia, Weight, and Gain

Table 16. Summary of RMS Pointing and Tracking Errors

Signal Current at Anode (A)	Background Current at Anode (A)	Steering Mirrors ON	Gimbal Mirror ON	Table Rotating(a)	Error Angle (μ R RMS)		
					Horiz. Track	Vert. Track	Horiz. Point
1.8×10^{-5}	2×10^{-12}	No	No	No	0.75	0.8	1.1
1.8×10^{-5}	2×10^{-12}	Yes	Yes	Yes			1.9
<u>Case I</u>							
1.8×10^{-6}	2×10^{-12}	Yes	Yes	Yes	1.2(b)	1.85(b)	1.3
<u>Case II</u>							
1.8×10^{-6}	3×10^{-6}	Yes	Yes	Yes	1.45(b)	2.05(b)	1.8
							0.9

(a) 2500 drive motor rpm = $0.064^\circ/\text{second}$ (1120 $\mu\text{rd}/\text{sec}$)

Case I corresponds to a low background situation

Case II corresponds to worst case tracking with 0 dB S/N margin

(b) Measured with Ballantine RMS meter. Other RMS values determined point-by-point from chart recording.

d. Boresighting

A retroreflector was placed in the pointing beam after it passed through the beam splitter (see Figure 19), and the pointing beam was reflected back parallel to its path so that when it struck the beam splitter, part of the pointing beam was reflected toward the image dissector. The reflected pointing beam and the beacon beam were aligned (boresighted) when the two beams struck the same point on the image dissector photocathode surface. Conversely, if the pointing beam was adjusted to strike the same spot as the beacon beam, then the two beams were parallel and at the furthest point of their common path; that is, at the beacon laser, the beams were still parallel. This was found to be true within the accuracy of the measurements. The retroreflector has a possible error of up to 5 microradians. It was noted that the beams had to be well collimated and the image dissector correctly focused to obtain best boresighting.

Two prime sources of error were found, both resulting from parallel but not coincident paths for the beacon and pointing lasers. If the pointing beam does not strike the retroreflector in its center, then the reflected beam will be parallel within 5 microradians, to the incident beam, but displaced from it. In this case, if the photocathode was at the focal point of the lens, then the pointing beam still was incident on the same spot as the beacon beam. However, if the focus was not correct, adjusting the pointing beam to strike the same spot as the beacon introduced misalignment of the two beams.

The second source of systematic error was the tracking telescope. If a collimated beam enters and leaves each beam expander, and if the pointing and beacon beams are parallel but slightly displaced, then the displacement is magnified. This may bring about truncation of the pointing beam and subsequent apparent motion when the table rotates. If a beam expander is not properly focused, a displacement in beams produces a difference in their angles when both beams go through the telescope.

When both beams are properly collimated and the optics properly focused, boresighting is a simple technique for aligning the pointing and beacon beams.

e. Point-Ahead

Point-ahead is the deliberate insertion of a controlled misalignment between the beacon and the pointing laser. It is required in space because of the aberration of light when terminals have large tangential relative velocities. The situation cannot be duplicated in the laboratory; however, it can be determined that the mechanism employed for inserting the point-ahead works accurately.

As far as the results are concerned, it is immaterial whether the pointing laser is adjusted with respect to the tracker or vice versa. In a practical case in space, the best way may be for the computer point-ahead angle to be inserted as an electrical current bias on the image dissector deflection coils.

For the laboratory case, it was easiest and most accurate to make an optical deviation of the beam into the image dissector and then to measure the resultant deviation of the pointing beam.

Two methods were used, both with good results. In the first method the image dissector was initially tracking with the fast steerers not operative. A 60.3-microradian wedge was inserted in the beam from the beacon. This caused the image dissector coil currents as displayed on an oscilloscope to shift. A wedge-shaped attenuator in front of the image dissector was then rotated from its angle of minimum deviation to compensate for the wedge in the beam and to restore the coil current to its initial value. The first wedge was then removed, leaving a bias angle of 60.3 microradians in the image dissector.

The fast-tracking mirrors were implemented and the pointing beam was then completely off scale, 60.3 microradians being far in excess of the detector range. The 60.3-microradian wedge was then inserted in the pointing beam just ahead of the focusing lens for the detector. This brought the pointing error signal back on the recorder scale and to within 1.5-div. alignment with its original position. This error of 2 microradians is an acceptable value since the angle set into the image dissector deviation was probably not better than ± 5 percent (3 microradians).

In a second method, the 60.3-microradian wedge was inserted in the beam just in front of the image dissector. Because of the angle demagnification effect of the telescope, the actual space angle deviation introduced in pointing was 5.3 microradians. This deviation was within the range of the pointing detector, and a deviation of 6 div. was noted at the recorder. A 4.8-microradian calibration wedge was put in the pointing beam and rotated, giving an 11-div. peak-to-peak deflection. This calibration gives a 5.2-microradian point-ahead angle. This result is closer than the accuracy of the measurements justify but can be accepted as showing that the point-ahead function operates as designed to within the accuracy of the measurement capabilities of the evaluation system.

7. GIMBAL INERTIA AND BEARING FRICTION

a. Tests Conducted

The effects of gimbal bearing friction, gimbal mirror inertia, and servo amplifier gain were evaluated by measuring the tracking error (1) with the gimbal mirror and table immobile, (2) with two values of load on the bearings, (3) with two inertia values for the gimbal mirror, and (4) for several values of gain. It was found that increased load on the bearings, increased inertia, and a low gain each gave decreased tracking error.

All tests were conducted with a signal intensity giving 1.8×10^{-6} A anode current. There was no added background illumination. The gimbal mirror torque motor current values in Table 17 are given as high frequency and low frequency values. The high frequency data are the noise in the current traces, and the low frequency data are the current range at the frequency of table rotation. Thus, the low frequency values represent the current or torque necessary for the mirror to compensate for friction. A summary of results is given in Table 18.

b. Static Tracking Accuracy

The tracking error noise with the steering mirrors operative but the gimbal mirror and table inoperative is shown first in Table 17. The noise in the horizontal tracking circuitry was minimized so that effects such as those considered in this test can be measured. However, less effort was expended on the vertical channel tracking circuitry. The vertical tracking noise is more than twice the horizontal tracking noise in the experiment and changes little under other experimental conditions. Thus the vertical channel values are not indicative of the effects being measured, and the conclusions are based on horizontal axis performance in which the table and gimbal motion takes place.

The static horizontal tracking error noise was 0.8 microradian rms without gimbal mirror or table motion. This value provided a reference for the subsequent results.

c. Dynamic Tracking Accuracy

The effects of friction, inertia, and servo errors are to produce errors in the correct positioning of the mirrors. These position errors result in corresponding errors in both pointing and tracking. Because it was the cleaner signal, the tracking error was selected as the better observation point for these tests. Pointing had truncation effects.

The smallest tracking error noise achieved for these signal and background conditions, and with the gimbal mirror and table operative, was 1 microradian rms in the horizontal channel. The recorder trace has been shown in Figure 35. Full inertia, loaded bearings, and low servo gain were used to obtain this value. As the effects of decreasing the inertia, decreasing the load on the bearings, and increasing the gain are considered in the following, each is judged by how the horizontal tracking error noise related to the 1 microradian rms tracking error value obtained in this test.

Table 17. Gimbal Inertia, Bearing Friction, and Gain Effects

Case	Table and Gimballed Mirror Operative	Weight on Bearings (oz)	Inertia (oz-in.-sec ²)	Servo Amplifier		Tracking Error (microradians RMS)		Torque Motor Current (mA 0-peak)	
				Rel. Gain	Band Width (Hz)	Horizontal	Vertical	High Freq	Low Freq
1	No	39	0.3	—		0.8	1.7	—	—
2	Yes	39	0.3	0.25	4	1.0	1.8	2	9
3	Yes	13	0.3	0.25	4	1.2	1.8	2	5
4	Yes	13	0.03	0.25	13	1.6	1.9	3	3
5	Yes	39	0.3	1	8	1.15	1.9	6	9

The rate table oscillates through 1.75 degrees at a rate of 0.067 deg/sec (2500 rpm on the drive motor). All tracking error measurements were made on the Ballantine RMS meter.

Table 18. Summary of Effects of Friction, Inertia, and Servo Gain

Parameter	Horizontal Tracking Error – One-Axis Values	
	Magnitude (μrad)	Source of Data in Table 17
Static value, Table and Gimbal Inoperative	0.8	Case 1
Dynamic Value, Table and Gimbal Running	1.0	Case 2
RMS Value of Added Noise	0.6	Cases 1 and 2
Effect of Friction, Reducing Bearing Load From 39 oz to 13 oz – Magnitude of Added Component	0.7	Cases 2 and 3
Effect of inertia, Reduced From 0.3-in.-sec ² to 0.03 oz-in.-sec ² – Magnitude of Component	1.1	Cases 3 and 4
Effect of Servo Gain, Increased From 4 to 8 Hz – Magnitude of Component	0.6	Cases 2 and 5

d. Effect of Bearing Friction

When the load on the gimbal bearings was reduced to 1/3 its value, the tracking noise rose to 1.2 microradians rms in the horizontal channel. The gimballed mirror was constructed with an inertia of 0.03 oz-in./sec² and, to obtain the inertia of a 6-in. mirror system, lead weights were added to achieve 0.3 oz-in./sec². The full-inertia, low-bearing-force case considered here was obtained by counterweighting the lead weights on the mirror. This was accomplished with a monofilament line over a pulley system used to suspend the gimbal and relieve the weight on the bearings. The forces on the gimbal mirror shaft were adjusted until no torque was exerted on the mirror by the counterweight suspension system. Only about half the current necessary to drive the mirror under full bearing force conditions was needed to overcome the reduced bearing friction. Since reducing the load on the bearings, over the range used, reduced the current to overcome friction but increased the tracking noise, an explanation is not clear. One would expect the tracking noise to reduce when the friction reduced. Looseness in the bearings, eliminated by additional preload, would be expected to affect the cross-axis tracking error. Possibly, the additional friction

added a beneficial damping effect. In any event, there is a significant effect of friction on tracking accuracy and, pending a suitable model, bearing assemblies should be empirically adjusted for lowest tracking error. The test did not include enough values to know if an optimum value was used for the overall evaluation measurement.

e. Effect of Mirror Inertia

With the inertia reduced by 10 and the counterweight removed, total tracking error rose still further to 1.6 microradians rms. This is a component of 1.1 μ rad and clearly shows the tracking advantage of increased inertia. The decreased inertia makes the mirror more responsive to noise in the signal from the fine steering mirrors, as well as to other sources of noise. The current required to drive the mirror with all weights removed is about half that required to drive it with the full inertia and low bearing load, and a third of that required to drive the mirror with full inertia and full bearing load.

f. Effect of Servo Amplifier Gain

When the gain on the servo amplifier controlling the gimballed mirror torque motor is increased by a factor of 4, the most pronounced effect is on the noise in the current through the motor. Although the current necessary to drive the mirror is the same as the case of Figure 35, the current noise is three times as large as that in the reference case. Figure 43 shows the increased current noise. Although the noise in Figure 35 appears to be primarily 60-cycle signal originating in the electronics, the noise in Figure 43 appears to be white noise and is due to the high gain amplification of the displacement sensor noise.

In order to reduce the effect of the displacement sensor noise in masking other servo problems, the evaluation of friction effects was based on cases 2, 3, and 4 shown in Table 17. In these cases, the gimbal servo gain was lowered to the point where the displacement sensor noise was not considered the major contribution to the change in tracking error from agile mirror loop operation to agile mirror plus gimbal loop operation. The lower gimbal loop gain makes the tracking error more sensitive to gimbal friction, which is desired in order to expose possible friction problems.

g. Influence of the Gimbal Loop on Tracking Error

Using the data presented in Table 17, one can conclude that, excluding the effect of the displacement transducer noise, the gimbal operation will introduce negligible tracking error when operated in the present system configuration.

The breadboard configuration has two factors that result in different gimbal performance from that expected in the final configuration. One of the factors is the higher noise level in the image dissector because of smaller-diameter optics. The second factor is the presence of a relatively large noise source from the displacement transducer of the agile beam steerer loop.

As shown in Table 17, a tracking error of 0.8 μ radians was measured with the gimbal loop inoperative. Considering the fact that the agile mirror loop attenuates the image dissector noise in the indicated tracking signal, this 0.8 μ radian error is probably due primarily to the displacement sensor noise.

The tests of Table 17 use a low bandwidth gimbal loop to reduce the effect of the existing displacement sensor noise. In using lower bandwidths, the friction effects on tracking error are amplified. In extrapolating the results of Table 17 to indicate tracking error due to friction with the full bandwidth, one decreases the friction error effect by the ratio of the test bandwidth to the final configuration bandwidth. See Eq. (1) of Section III for the reason for using bandwidth ratio.

As shown in Table 17, the worst case is when the bearing is lightly loaded (13 oz) and the inertia is nominal (0.3 oz-in./sec). A conservative assumption is made that the change in tracking error from no gimbal to gimbal operation is due to gimbal friction only. Thus, the friction component, on a root sum square basis, is 0.9 microradian. Extrapolating to the 7-times-higher bandwidth used in the final system, the rms friction error due to gimbal operation is 0.13 microradian.

In Table 19 the extrapolated final system performance estimate is given based on cases 2, 3, and 4 of Table 17. Case 5 is not included because it is apparent that the displacement sensor noise is the principal reason for the increase in output when the gain is increased. Case 5 illustrates why the tests were made with low gimbal bandwidths - to eliminate this noise effect.

Table 19. Extrapolated Friction Error - Final System Configuration

Case (see Table 17)	Indicated Tracking Error (Test) (μ radians)	Gimbal Bandwidth (Test)(Hz)	Gimbal Inertia (Test) (oz/sec ²)	Extrapolated Friction Error (Final Config.) (μ radians)	Gimbal Bandwidth (Final Config.) (Hz)
2	1.0	4	0.3	0.1	25
3	1.2	4	0.3	0.15	25
4	1.6	13	0.03	0.07	25

The use of the low-gimbal-inertia and low-gimbal-loop bandwidths in the test have given indication that no gimbal servo error sources are hidden just beneath the experimental noise level of the test. With an order-of-magnitude reduction in the noise of the agile-mirror displacement sensor, the gimbal servo as presently designed for the breadboard will meet the required accuracy. Further assurance of meeting the accuracy comes from the total elimination of the displacement sensor and the high sensitivity to agile mirror motion that it causes.

8. EFFECTS OF VEHICLE MOTION

Vehicle motion was simulated by rotation in the horizontal plane of the entire tracking assembly with respect to the beacon assembly. Angular velocities of $\pm 1,120$ micro-radians/sec were used. This was close to the maximum expected limit cycle rate of $1,200 \mu\text{radians/sec}$ for a space vehicle.

The minimum rate which could be run was 10 to 12 microradians/sec because of a minimum operating speed of the drive motor. At this speed there was no indication of an increase in noise such as might have been anticipated using earlier models for bearing friction which hypothesized a stick-slip form of low-speed friction.

Test data for the table OFF case are shown in Figure 44; those for the table ON case were previously shown in Figure 35. It was found that table motion introduced an increase in horizontal tracking error from 0.85 to 1.0 microradians rms (see Table 20). This amounts to an added component of 0.53 microradian rms. This may be due to observable vibrations introduced in the tracking system by the 2,500-rpm drive motor.

Effects of acceleration at reversal are discussed in Section IV, 5.c.(3). Measurable tracking errors on the order of a microradian peak were found but, as noted above, the acceleration was many times normal. Both of these error sources are due to the table and may be less in a vibrationless system with normal acceleration.

Table 20. Effects of Vehicle Motion

Table ON	Fine Steering Gimballed Mirrors ON	Weight on Bearings (oz)	Inertia (oz-in.-sec ²)	Torque Motor Current (mA 0-Peak)		Tracking Error ($\mu\text{rad rms}$)	
				High Frequency	Low Frequency	Horiz-ontal	Ver-tical
Yes	Yes	39	0.3	2	9	1.0	1.8
No	Yes	39	0.3	2	0	0.85	1.75

9. IMAGE DISSECTOR PHOTOCATHODE SENSITIVITY MAPPING - TEST 9

a. Mapping Program

The photocathode was mapped by tracking a target that was deflected in a raster scan across the active photocathode area. As the target scanned, it appeared to have varying brightness because of an increase or decrease in photocathode sensitivity. The change in photocathode sensitivity was measured by recording the varying current.

b. Results

The detected power was plotted (Figure 45) as a spot image was scanned at set vertical angles of $+8 \text{ min}$, $+6 \text{ min}$, and $4, 2, 0, -2, -4, -6$, and -8 min . For each vertical

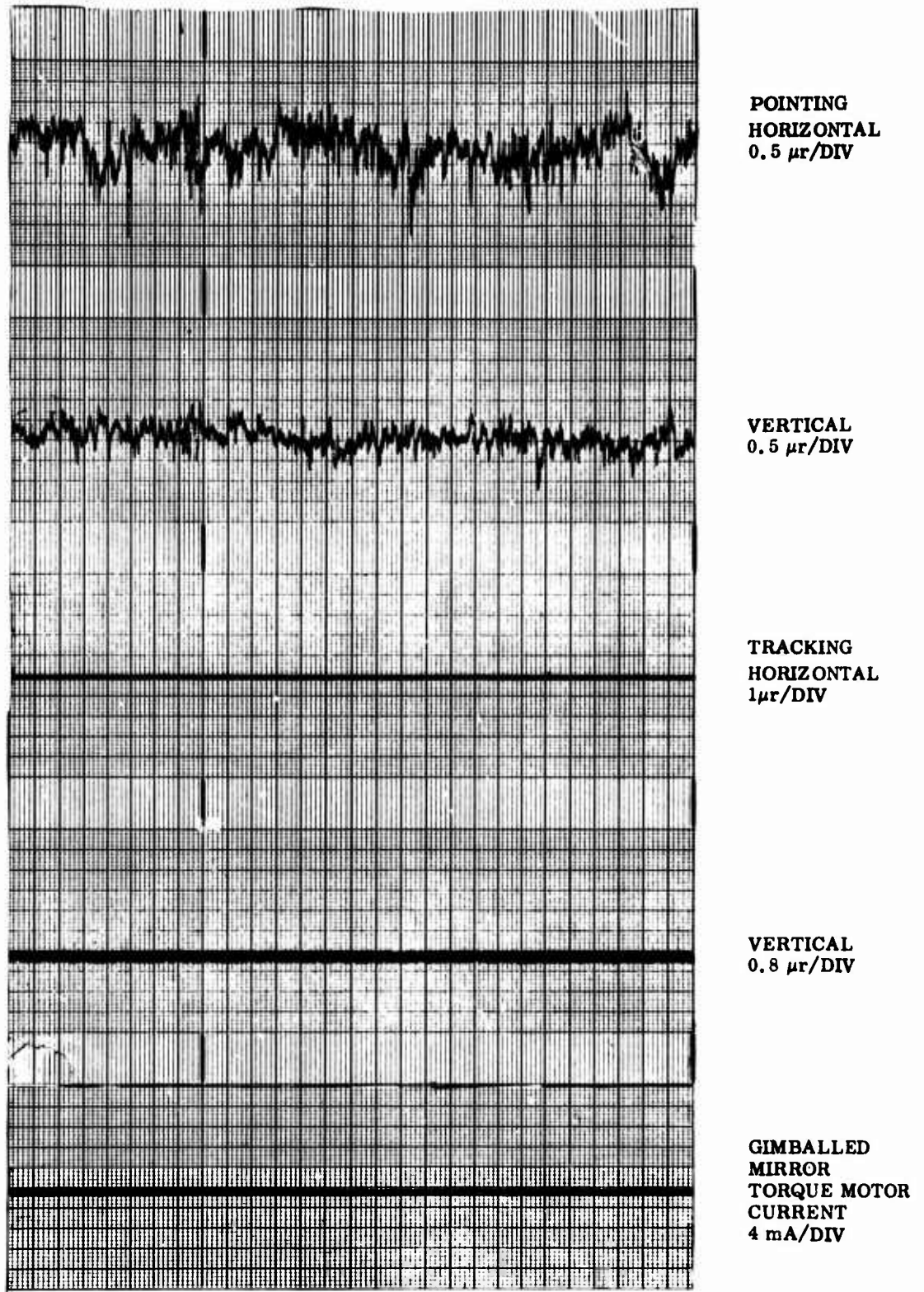


Figure 44 Pointing and Tracking Signals With Table Not Running But With Fine Steering and Gimballed Mirrors Operating

setting the horizontal scan was swept from about -8 min to +8 min so that a 16-min by 16-min field was swept. The light source was reviewed through an 80-in. Questar telescope; hence, the 16 min is equivalent to 0.373 in. on the photocathode.

The measuring system response was 0.25 volts, 0.3 star magnitudes, per inch. Sensitivity variations in the area of the photocathode used (Figure 45) had a range of 3/16 in., which is 0.056 of a star magnitude. This corresponds to a sensitivity range of 5 percent. In a worst case this range would take place in the width of the image spot and could cause a displacement of somewhat less than 0.5 percent of a spot width, possibly 0.3 or 0.4 microradians, in the center of illumination. However, this would be inherently compensated during alignment or boresighting. Slow mechanical or thermal drifts in an operational system, which might shift the null point on the image dissector, would be corrected for by the closed-loop feature of the tracking system.

10. ATMOSPHERIC TURBULENCE EFFECTS

Atmospheric turbulence can produce beam wander, which in turn results in error signals at the tracking and pointing detectors. Errors at the tracking detector (image-dissector) can be greatly reduced by activating the fast-tracking mirrors. It was anticipated that fast steering would also result in a reduction of pointing error due to air turbulence. This was found to be true, as can be seen in Figure 46. For this measurement the optical alignments were adjusted to simulate a communication link. This required the beams to be similar in size and intensity distribution as well as to be in optical alignment.

The turbulence in the optical path, and thus the beam wander, was normally kept to a low value by shielding placed around the optical paths. The effects of turbulence were studied by removing a portion of the shield where the optical path is common to both beams. Controlled turbulence was introduced by using a device which blew air from a compressed source across electrically heated coils and through the optical path. The frequency distribution of the tracking error signal introduced by the turbulence is shown in Figure 47. It was measured with a Hewlett-Packard Fourier analyzer. The turbulence magnitude was found to be repeatable for given values of current through the coils and air pressure.

The power spectrum of each voltage signal, for a 1-ohm load, was displayed on a CRT (Figure 47). The CRT displays have logarithmic abscissas and ordinates; 2 cm vertically corresponds to 10 dB, and 2 cm horizontally corresponds to a decade in frequency.

Figure 48 also shows the spectrum of the equivalent signal from the pointing detector with the mirrors activated. The two photographs have been arranged on the page so that the vertical scales match. The improvement is remarkable and could be anticipated to be even greater with equipment designed with this test in mind. The spectra show a decrease in signal of about 35 dB at 3 Hz, essentially no change at 100 Hz, and an increase of more than 5 dB at 300 Hz — all due to the activation of the steering mirrors.

Initially the pointing signal was not improved greatly by activating the steering mirrors because the distribution of energy across the cross sections of the two beams was not the same and their paths were not colinear. The beacon beam has a larger diameter, with

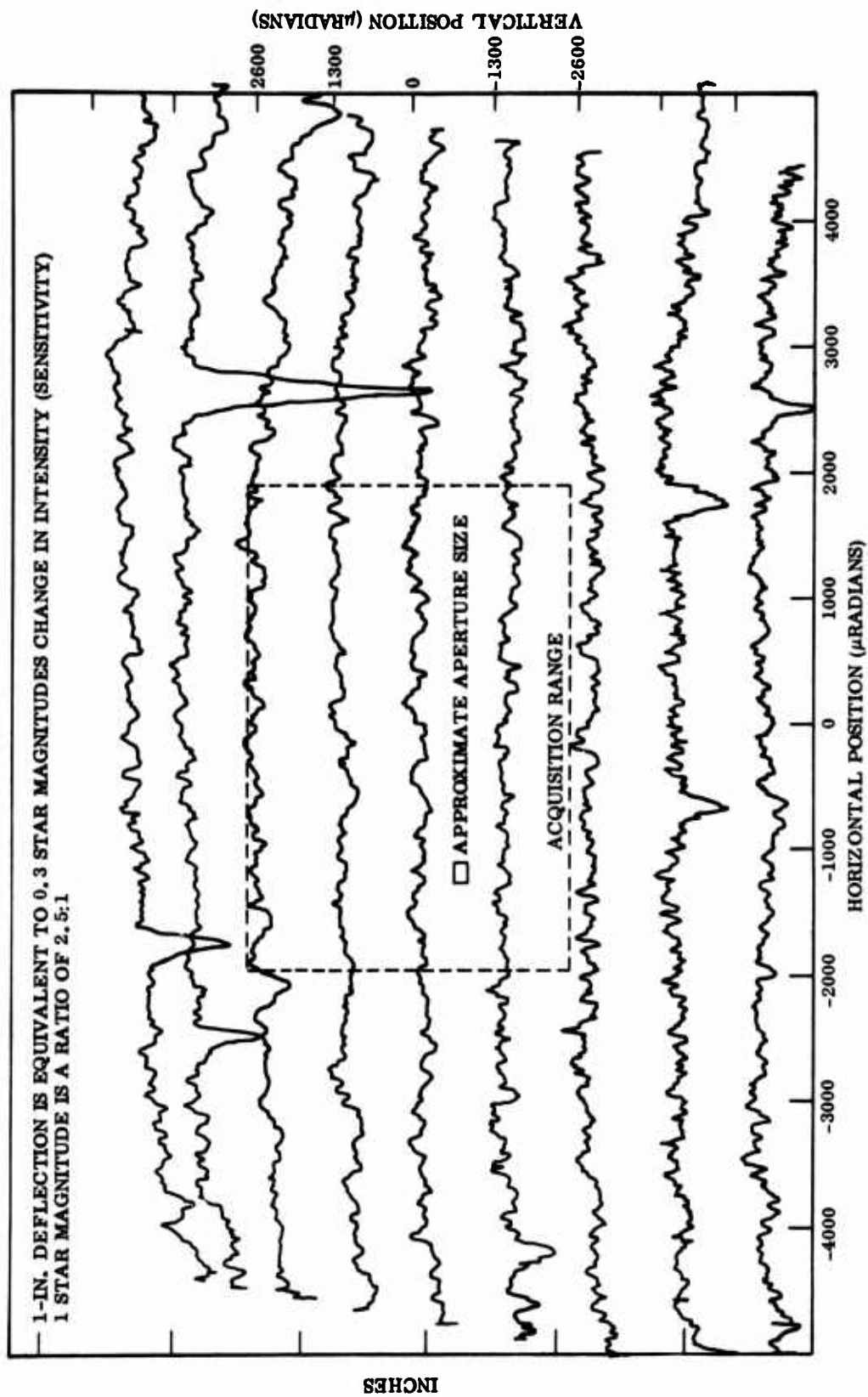


Figure 45 Map of Photocathode Response as a Function of Spot Position

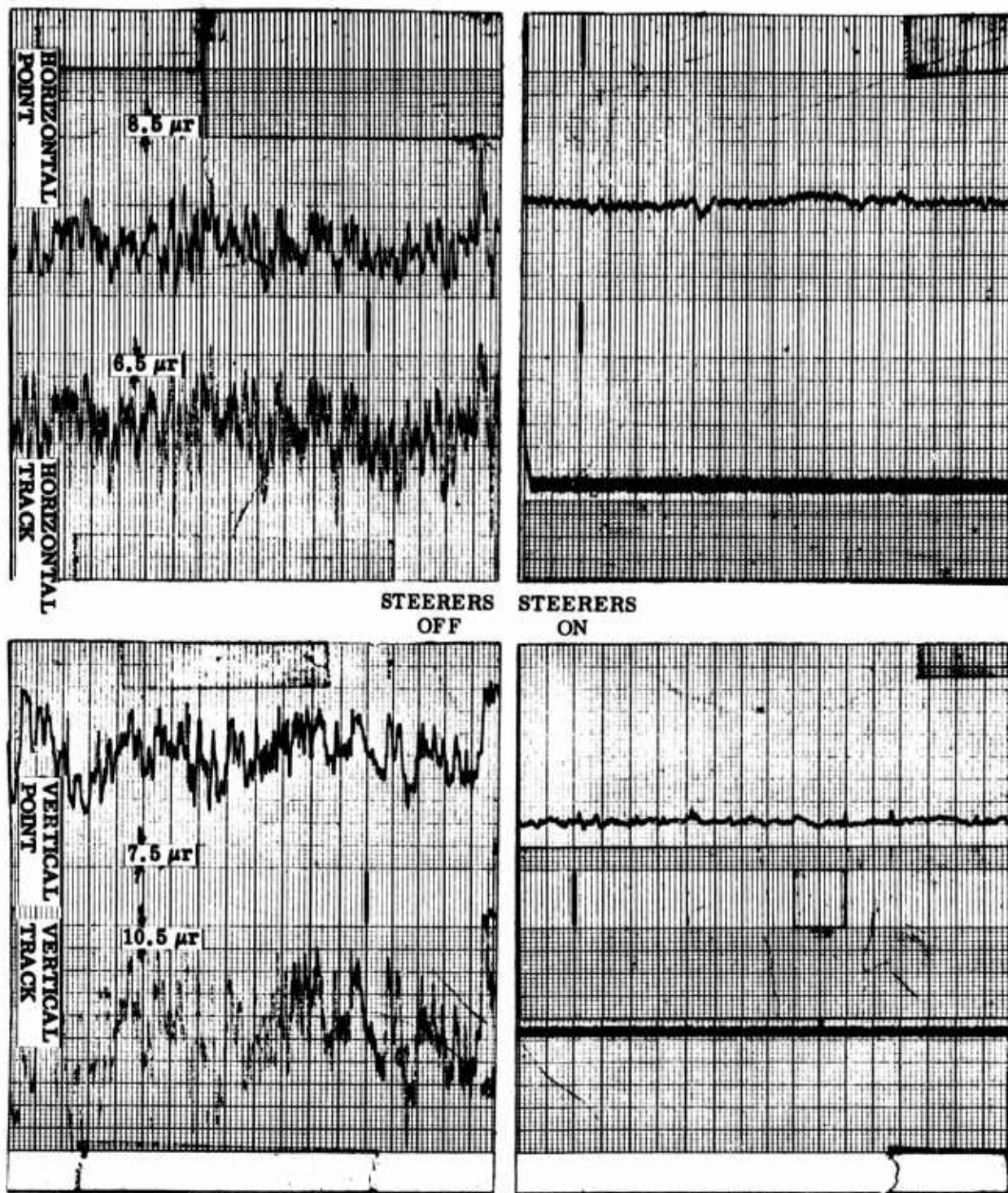


Figure 46 Pointing and Tracking Detector Outputs With Generated Atmospheric Turbulence. Sections from continuous trace scales remain constant across page (see Figure 41 for an unbroken trace)

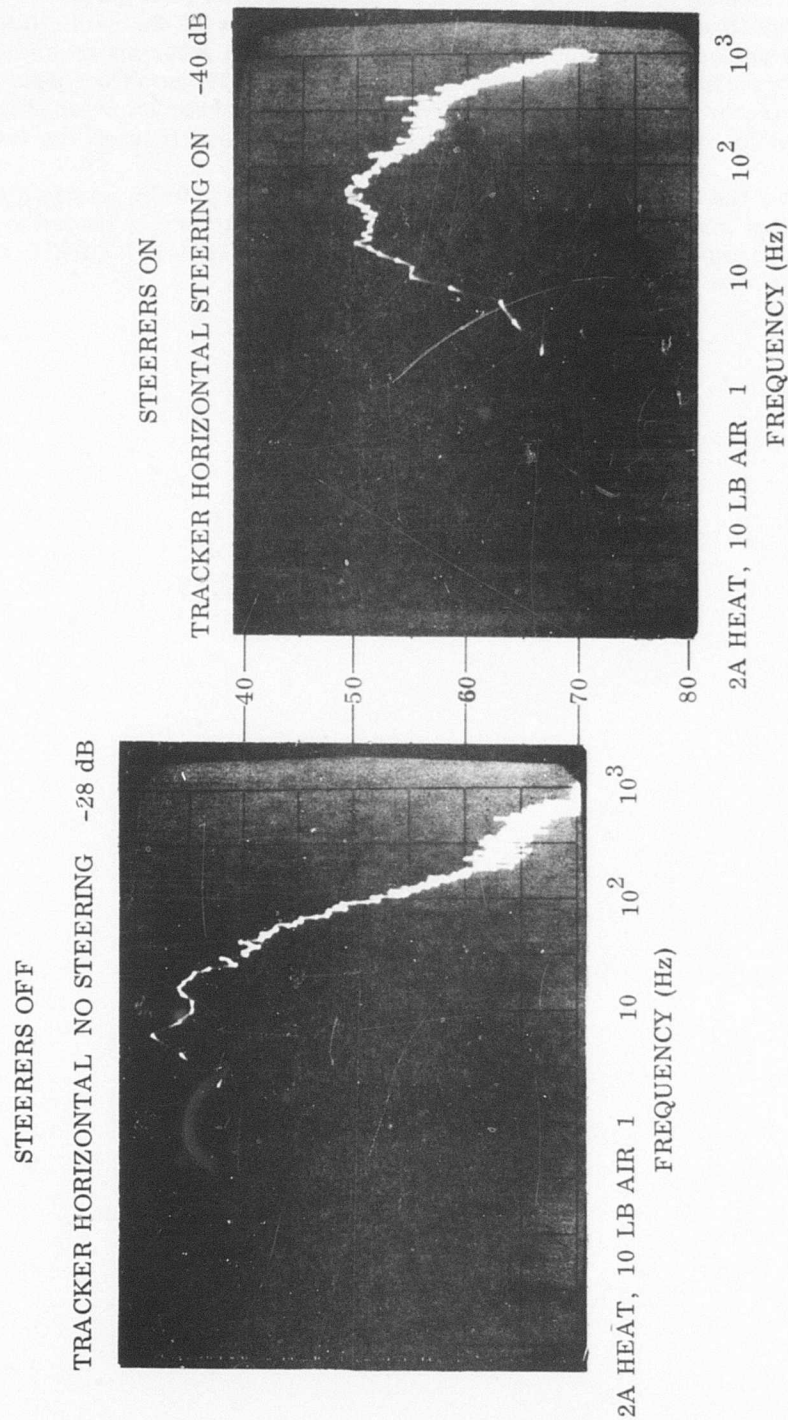


Figure 47 Power Spectra of Tracker Horizontal Output With High-Frequency Turbulence (Heat and Air)

the energy distributed more evenly across the cross section than the pointing laser. An aperture was then placed in the beams, making both beams the same diameter, with relatively uniform distributions of energy. The beam steerers then greatly reduced the effects of the turbulence in the pointing detector. Figure 48 shows the power spectra from the pointing detector output. Here, steering reduced the error signal at 3 Hz by 20 dB, and raised it at 300 Hz by 10 to 20 dB. This is uncertain because it is off the low end of the scale.

Figure 46 shows the actual time traces of the tracking and pointing error signals. The improvement made on all axes of both pointing and tracking is indeed striking. This subject was explored in more detail by work done on contract F33615-72-C-1938 and will be reported in full on that contract.

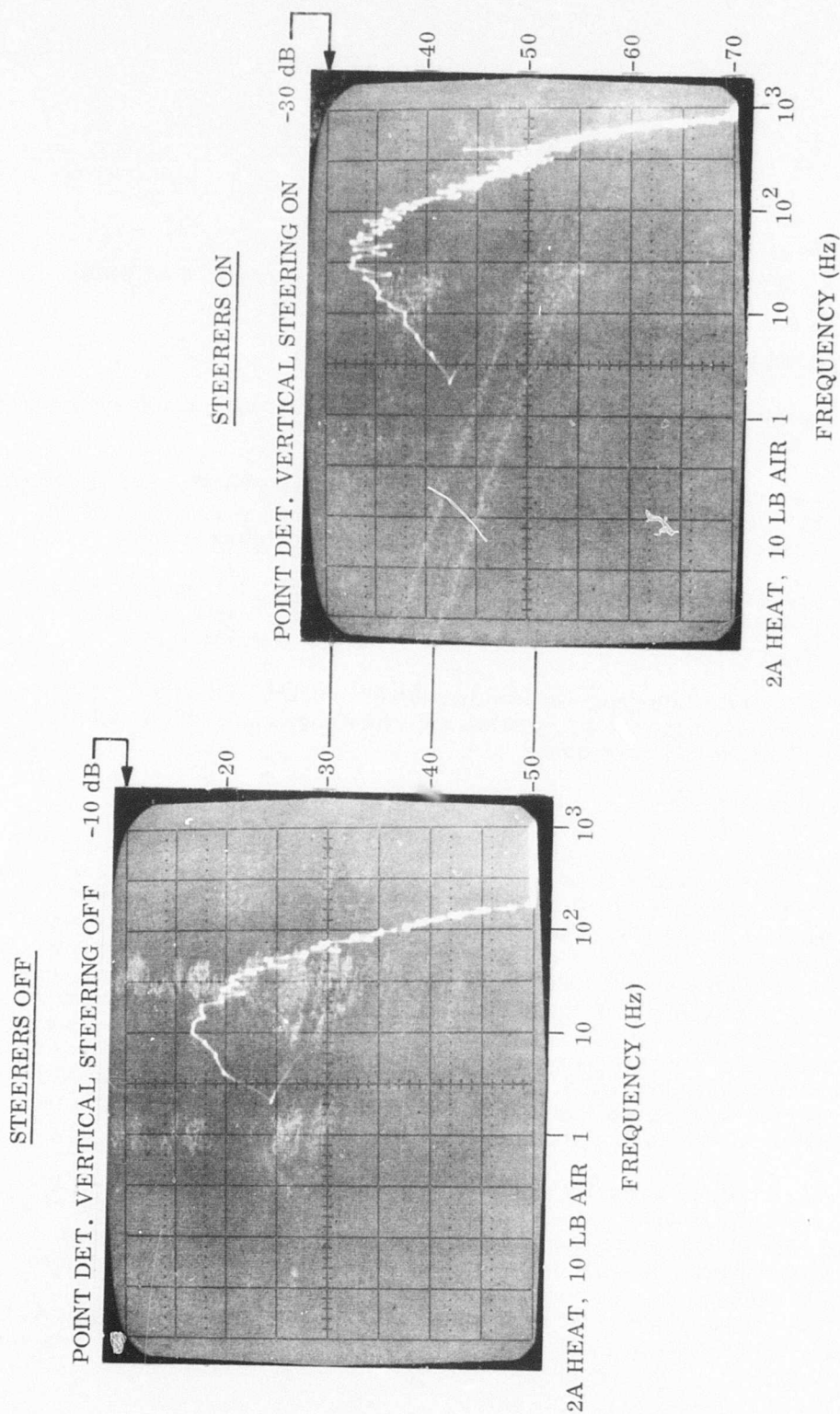


Figure 48 Power Spectrum of Pointing Detector Output With Beam Steerers Off and On (Vertical and Horizontal Scales Are Logarithmic)

Section V

CONCLUSIONS, ERROR ANALYSIS, AND SCALING FACTORS

1. CONCLUSIONS

The primary conclusions made from the results of the acquisition and tracking evaluation tests are as follows:

- Laboratory testing of an optical model with reduced-size primary optics is a practical method of studying some of the noise sources that degrade the performance of a full-scale tracking and pointing system.
- The data obtained confirm the SDRS preliminary design study results and indicate that the performance to be expected for a full-size model should at least approach that predicted by the study (Reference 1).
- The evaluation program was extremely valuable, not only for the measured results but for the information and experience applicable to future design work and test programs.

2. ERROR ANALYSIS

In the SDRS Final Report (Reference 1), a pointing rms error of $1/10$ beamwidth was designated as the allowable pointing error at one terminal, thus establishing a pointing loss factor for the communication system. The required received power for 0-dB margin was then calculated. The report, after a small correction, gave a FWHP beamwidth of 4.0 microradians for the $0.53\text{-}\mu\text{m}$ wavelength beam transmitted through a 6-in. diameter radiating aperture. This beamwidth thus required a 0.4-microradian rms, or smaller, pointing error by the tracking terminal. The 0.4-microradian value becomes 0.28 for one axis. It was assumed that, of the several independent pointing error factors, shot-noise at the tracking detector would contribute one-half of the total. Since the errors combine as the root of the sum of the squares (rss), the allowable tracker shot-noise component on one axis would be 0.2 microradians rms ($0.28/\sqrt{2}$) at the 0-dB signal-to-noise margin.

The tracking error is inversely proportional to the diameter of the beam, for constant detector current; so for the $7/8\text{-in.}$ -diameter beam used in the evaluation tracker, the rms error due to shot-noise should be appropriately larger, or 1.37 microradians. The other components of error in pointing do not scale, so their estimated sum in the test system remains at 0.2 microradians, as listed in Table 21. When they are rss'd with the shot-noise, the expected rms error increases only to 1.38 microradians so these other components are not very visible in the test data. However, they include

factors such as turbulence, mirror pick-off noise, and component vibration whose magnitudes are unknown but which in reality are probably larger than they would be in a qualified system operating in space.

Actual measurements of the pointing error in the horizontal axis with the tracking system working and the rate table running gave an rms value of 1.8 microradians. This value is compared to the predicted value of 1.38 microradians. Because of the fundamental calibration technique used at the pointing detector, with a precision calibration performed at plus and minus 4.8-microradians pointing angle, there is not likely to be a gross error in the actual pointing measurement. As noted on the preceding page, there are other error sources, applicable only to this particular laboratory model, which increase the pointing error.

Table 21. Comparison of Measured Pointing Errors With Expected Error

Pointing Error Component	Expected Errors	
	SDRS Final Report (Microradians)	Scaled To 7/8 In. (Microradians)
Shot-Noise At Image Dissector	0.2	1.37
All Other Sources	0.2	0.2
Total (RSS)	0.28	1.38
Measured Error	—	1.8

NOTES: Data taken with fast steering and table in operation.

All values in rms.

Pointing error measured on horizontal axis only since all turntable motion was on this axis. Vertical data not necessarily significant since it was not always maintained at maximum performance.

The measured value of 1.8 microradians is 30 percent greater than predicted by theory. Many perturbations are omitted from the computation of the theoretical value because their influence is unknown. Their uncertainties could accumulate into a considerable error in the difference between the predicted and measured pointing accuracies. These include: mechanical vibrations, pointing laser angular noise, turbulence components not corrected by the tracker, and noise due to the angular position pickoffs of the fast-steering mirrors. Hence, the theoretical pointing error is expected to be less than the measured value.

The important fact is that, regardless of the possible overstatement of the tracking accuracy allowable and some slight discrepancies in signal-to-noise at the image dissector, it has been shown that the pointing accuracy is as good as, or even better than, had been expected for the size of the optics used. No reason is apparent why the pointing accuracy will not increase in proportion to the beam diameter in going from 7/8-in. - to 6-in. -diameter optics.

Tracking errors are not explicitly analyzed because of their peculiar nature. The so-called tracking error, as measured by the image dissector error output, is not an accurate indication of the quality of performance of the tracking function. It can indicate a lot of shot-noise above the response band of the fast-tracking mirrors, and this does not contribute to pointing error. On the other hand, it could have a small error output while energetically driving the mirrors with low-frequency shot-noise - which would actually be a pointing error. Thus, the real proof of the overall system operation is the measurement of pointing errors.

3. SCALING FACTORS

The principal factor scaled in the evaluation, as compared with the SDRS preliminary design, was the diameter of the beacon beam. This diameter was adjustable, but for most tests the diameter was 7/8 in. and the scaling factor was 6.85. This meant that a diffraction-limited spot at the image dissector would be 6.85 times as large in angular diameter as it would be for a 6-in. aperture. In physical dimensions they will be alike because of a longer focal length for the big aperture. It has been shown (Reference 3) that shot-noise tracking errors are proportional to the spot angular diameter and also are inversely proportional to the voltage signal-to-noise ratio. Therefore, measured errors due to shot-noise would be less by a factor of 6.85 for a 6-in. -diameter optics system. This assumes that the signal-to-noise ratios are the same and that the receiver bandwidths are the same. The budgeted shot-noise error of 0.28 microradians for the 6-in. system was scaled up to the 7/8-in. system by multiplying by 6.85 to get 1.9 microradians rms budgeted.

Section VI

COMMENTS AND RECOMMENDATIONS

1. GENERAL COMMENTS

The evaluation "breadboard" equipment provided experience both with the image dissector tracker as an angular error detector and also with the use of crossed roof-prisms in conjunction with a quadrant detector.

As was anticipated, the equipment was highly subject to external disturbances. These were reduced to tolerable limits but, for more accurate equipment, the precautions will have to be even more stringent. The primary disturbances were as follows:

- Atmospheric turbulence (by far the worst offender) led to errors. Although shields were put around the optical paths, a small residual turbulence error undoubtedly remained.
- The system was very sensitive to any mechanical shock applied to the support table or any part of the system.
- On intermittent occasions, the pointing was very sensitive to acoustics. This was thought to be caused by a "loose" optical element, such as a beam-splitter, which vibrated with sound energy excitation.

One HeNe laser was used for the beacon and another HeNe laser was used for pointing because of the difficulty in obtaining a suitable laser with a different color. The use of this pointing laser caused the following problems:

- There was a tendency to acquire and track the pointing laser, and it had to be blocked off during acquisition.
- To keep the pointing laser from affecting the beacon tracking error, the pointing laser was operated slightly misaligned from the beacon. The misalignment occasionally caused the pointer beam to truncate at some place in the system. The amount of truncation would vary as the table rotated and could result in a shift of pointing with table rotation, as seen on some of the strip chart records.

The use of precision optical wedges for calibrating angle detectors was very effective.

The coarse gimbal needs to be firmly positioned during acquisition to prevent the initial transient from the fast-steering mirror from driving it too far out of position.

At the lowest S/N operating conditions, 0-dB margin, ambient light produced targets which could be acquired, and it was necessary to turn out the lights. The 0-dB margin was set with the lights out. When tracking, room lights had little effect.

Adjustments of the optical elements were troublesome where there was mechanical backlash or cross-coupling between axes.

Although the evaluation equipment was less accurate than a full-scale model, it was necessary to have high-quality optics to maintain scale accuracy.

A number of helpful techniques were utilized during the evaluation to assist in alignment and adjustment. They were as follows:

- Positioning of the pointing spot on the sharp edges of the roof prisms was observable by use of a screen with a pinhole, for the beam, in front of the prisms. The several reflections from the surfaces of the prisms could be observed around the pinhole, and their relative intensities were an indication of the centering accuracy of the spot.
- A thick optical flat tilted in collimated portions of the beams could be used as a focusing aid by finding the focus position at which tilting had the minimum effect.
- Fringes by reflection, using the same optical flat, were a sensitive indication of beam collimation.

2. RECOMMENDATIONS

Recommendations resulting from the data and experience of the evaluation are as follows:

- The AGC should be made to operate on the dc signal level as designed in the SDRS final report. The AGC employed alternating current because that was incorporated in the ITTG in-house tracking system used in the tests.
- Only highest-quality optics should be used in any critical optical path.
- Further study should be made of the required bandwidth of the fast-tracking system. Although friction effects were small, the results obtained by using reduced gimbal inertia and lower gimbal servo gain implied that the friction was at most no larger than that assumed for the SDRS final report. Based on the bearing test data from Ball Brothers Research Corporation reports, it appears that the fast-tracking loop bandwidth could be reduced. This would reduce shot-noise errors without increasing errors caused by friction disturbances.
- In any laboratory tests, consideration should be given to two layers of air shields, one close to the beams and one encasing beams and components.

- Heat (or cold) sources should be eliminated from the shielded air passages.
- An improved method of position indication is needed for the fast tracking mirrors.
- In a future test system, all components should be mounted as rigidly as possible to the base or frame.

Appendix I

OPTICAL PARAMETERS

1. OPTICAL COMPONENTS

The optical functioning can be observed by referring to Figure 1. The beacon HeNe laser beam goes through a spatial filter and beam-expander at the output of the laser. It passes through a beam-splitter, which separates the incoming beam from the pointing laser, and strikes the gimbaled mirror. The beam is reflected from this and additional folding mirrors and passes through the receiving 11.3-power telescope. Here it is folded twice by the fast-steering mirrors and then is separated from the pointing beam by a beam-splitter. It passes through two oppositely oriented wedge-shaped neutral-density attenuators and is then focused on the photocathode of the image-dissector after passing through a band-pass filter.

The pointing laser has no spatial filter or beam-expander. It is combined with the beacon beam by the previously mentioned beam-splitter and follows the path of the beacon in reverse until it reaches the beacon beam-expander where it is separated to the pointing detector. The parameters of these components are given in Table 22.

Table 22. Component Parameters

Item	Beacon	Pointing
Laser, Spectra-Physics Model No.	133	126
Power output (mW)	1.2	3.0
Wavelength (μm)	0.6328	0.6328
Beam-expander and spatial filter (Spectra-Physics Model No.)	336	none
Beam diameter (between terminals) (in.)	0.87	0.5
Focal length of detector optics (in.)	35.6	26
Spot angular diameter ($2\lambda/D$) (μr)	58	101
Spot linear diameter (in.)	0.002	0.0026

Appendix II

ANALYSIS

1. GOALS

The purpose of this section is to calculate the tracking error as a function of all variables. From these relationships the trade-offs among the variables can be seen and evaluated. The analysis is in four sections: Inherent errors in the overall specific system, errors due to tracking in a dynamic environment, and acquisition considerations.

2. TRACKER PERFORMANCE

We first calculate the value for the noise equivalent angle that results from shot noise and its being processed through the tracker loop. The calculations will determine the noise as inches on the photocathode which can be easily converted into angle error by dividing by the focal length. The task is divided into three sections: tracking error detector sensitivity, noise at the output of the tracker, and response of the loop to these signals. A functional block diagram is shown in Figure 49.

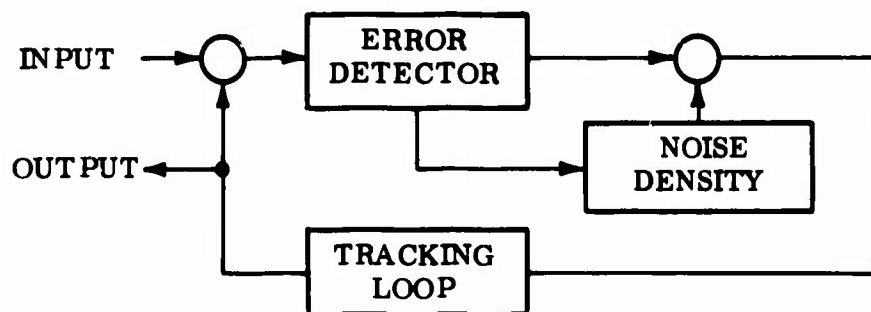


Figure 49 Block Diagram for Tracker Performance Evaluation

The error detector has an image dissector, load resistor and preamps, and a coherent demodulator. During tracking operation inside the tube, a small aperture, through which the tube can detect optical power, is in effect moved in a circular pattern on the face of the tube. The task of the tracking loop is to keep this circular pattern centered on the position of the optical image of the beacon. If the image is centered, the optical power detected by the tube will be constant in every part of the circular scan. If, however, the image moves from the scan center, the intensity detected will vary as the image is scanned. The phase and relative amplitude of the detector output will be demodulated to get information as to the angle and radial position of the moved image.

This information is applied to the servo loop, which will move the scan so that it will again center itself on the image. The scan's position, then, monitors the position of the optical image on the face of the tube to within the error limitations of the loop.

a. Error Detector

With the above functional description, one derives a mathematical description of the process. The image dissector is a scannable detector. Its sensitivity to optical power on the photocathode is given in units of amperes per watt. For the spectral region in which we are operating, $0.63 \mu\text{m}$, the sensitivity is 0.032 A/W , corresponding to an effective quantum efficiency of 6.3 percent. This sensitivity includes the attenuation due to an accelerating wire mesh electrode behind the photocathode. The photoelectrons which are focused through the scanning aperture are amplified in a dynode chain amplifier. The output of the tube at the anode is a current. By accumulating these factors, one can describe the current output of the anode that results from image power (electrons) that goes through the scanning aperture.

The next question is, how many get through? The image with W watts can cause Y amperes at the anode, using an effective sensitivity APW and a dynode gain GD

$$(W) (APW) (GD) = Y \quad (1)$$

if all electrons go through the aperture. The image diameter is about $25 \mu\text{m}$ (0.001 in.) in diameter and is labeled DS . The exact description to be used in this analysis assumes a diffraction limited optical system. The optical image diameter, DO , is

$$DO = \frac{\lambda f}{D} \quad (2)$$

where

D = aperture size of the optical telescope

λ = wavelength of the light

f = focal length of the telescope system

This is about the half-power diameter of the Bessel function that describes the Airy disk. In the system under test,

$$\lambda = 0.6 \text{ m}$$

$$D = 25 \text{ mm (maximum)}$$

$$f = 36 \text{ in.}$$

Therefore,

$$DO = 0.0009 \text{ in. (minimum)}$$

The electron image this will produce at the aperture will be slightly defocused by the electron optics, resulting in an electron image diameter of

$$\begin{aligned} DS &= DO \text{ (defocus factor)} \\ DS &= 0.001 \text{ in. (minimum)} \end{aligned} \quad (3)$$

For a first approximation a circular aperture much larger than the electron image will be considered. In the current tests, for example, the aperture is about $150 \mu\text{m}$ (0.006 in.).

One can speak in terms of the electron image scanning around a stationary aperture or of the aperture scanning a stationary image. Both are essentially true. The image is stationary at the photo cathode, and the aperture is stationary at the back of the magnetic focusing section. It is appropriate in this description to choose the point of view of the electrons from the stationary optical image being scanned magnetically around the physical aperture at the back of the focusing section. The scan of these electrons is designed to have a scan radius equal to the aperture radius. When there is no error, the center of the electron image will be on the edge of the aperture during the complete scan.

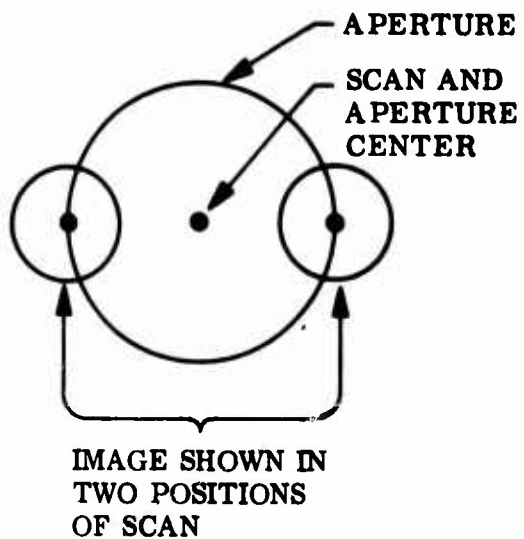
If, however, there is a positioning error between the center of the aperture and the center of the scan, more photoelectrons will enter the aperture during one part of the scan, and less during the opposite part of the scan as shown in Figure 50. When the error exists, the current out of the anode will vary sinusoidally at the scan frequency.

To derive the amplitude of this sine wave, let us assume that the aperture is much larger than the image size. A following section will derive a correction for the case in which this assumption is not true. A gaussian model will be used for the spot. The half-power width will be made equal to the half power width of the Bessel function. The amplitude of the current can be calculated by mathematically describing a gaussian function sampled by a moving edge. The amplitude for a given position error is, within a few percent, equal to that calculated by modeling the image as a uniform intensity circular spot with a diameter equal to DS , and with a photoelectron flow that is multiplied by an amplitude factor $(\pi/4)$. The a-c amplitude of the output current is the difference between the electron flow through the aperture when the image is centered on the aperture edge and when it is not.

The amount of increase in the current is the electron flow intensity (A/unit area) multiplied by the difference in the area, error $\times DS$, as diagrammed in Figure 51. Therefore the amplitude ΔI is

$$\Delta I = (\text{intensity}) \times (\text{error} \times DS)$$

NO POSITIONING ERROR



ERROR TO THE LEFT

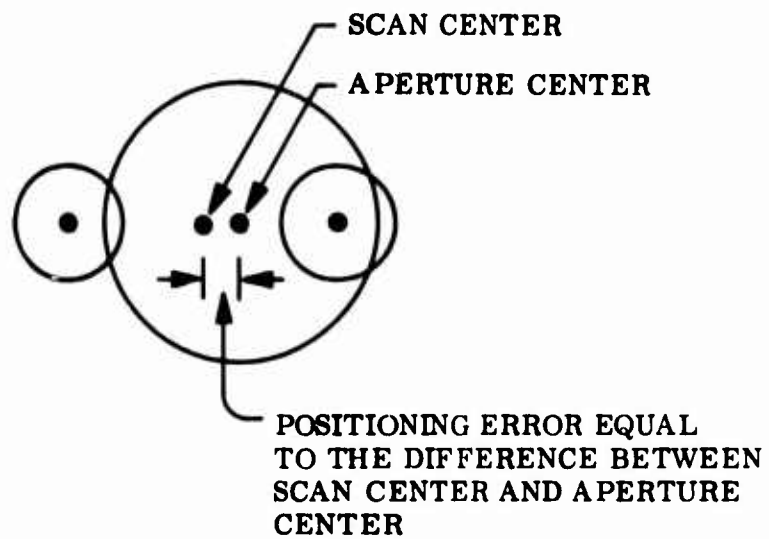
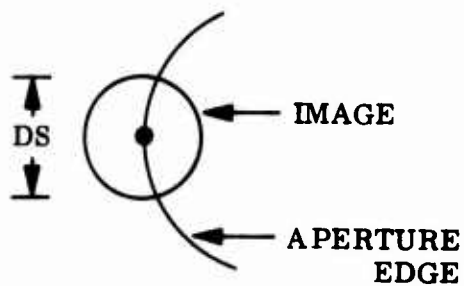


Figure 50 Tracking Error Generation

NO POSITIONING ERROR



WITH POSITIONING ERROR

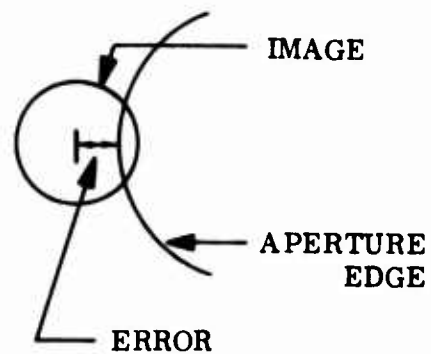


Figure 51 Model for Error Signal Generator

Since the model has uniform intensity, the following output current variation is obtained using Eq. (1),

$$\frac{(\pi) (W) (APW) (GD)}{(4) \frac{\pi (DS)^2}{4}} (X_e) (DS) = \Delta I \quad (4)$$

where

ΔI = amplitude output current

X_e = position error in inches

DS = electron image size

GD = gain of dynode chain

APW = effective photocathode sensitivity

W_i = total optical power on photocathode due to the image.

The more exact description for the current out of the anode is a sum of the sine wave due to positioning errors, an average d-c current level, d-c current due to background illumination of the photocathode and dark currents in the tube.

Putting this together, the total output current is obtained:

$$I_{\text{total}} = \left[\left(W_{\text{BKGD}} + \frac{W_i}{2} \right) APW + i_{\text{dark}} \right] GD + \left[\frac{W_i (APW) (X_e) (DS)}{(DS)^2} \right] \times \sin \omega_{\text{es}} t + \phi_{\theta}) GD \quad (5)$$

where

$i_{\text{dark}} = 2.6 \times 10^{-14}$ A for the tube and is quite variable from tube to tube. It will be ignored in most calculations as it is much smaller than the other currents

W_{BKGD} = Light power from background sources of illumination

ω_{es} = Scanning frequency in radians

The power in the background is given by

$$W_{BKGD} = (IFOV)^2 (\text{spectral radiance}) (\text{optical bandwidth}) (\text{lens area}) \quad (6)$$

where IFOV is the instantaneous field of view.

In this case, looking against sunlit clouds with a spectral radiance of $2.3 \times 10^{+4} \mu\text{W} - \text{cm}^{-2} - \text{steradian}^{-1} - \text{micron}^{-1}$, $2.5 \times 10^{-11} \text{W}$ is obtained which causes current through the aperture. This will cause about $8.0 \times 10^{-13} \text{A}$ input into the amplifier. The output currents, if $GD = 1 \times 10^6$, are as follows:

- Background - $8 \times 10^{-7} \text{A}$
- Good tracking signal, average current - $1 \times 10^{-5} \text{A}$
- Amplitude error current for 10 percent spot size positioning error - $3.2 \times 10^{-6} \text{A}$
- Dark current - $2.6 \times 10^{-8} \text{A}$

The expression for the sine wave current out of the tube is proportional to the tracking error signal. The error signal must be amplified and coherently detected to produce correction voltages to quadrature magnetic coils that correct the scan position. The tube output current passes through a shunt resistor R_L to produce an output voltage. It is amplified first in a low noise preamplifier, then by other a-c coupled amplifiers, and is presented to two coherent detectors operating in quadrature. The detectors are a chopper type of doubly balanced mixer. The phase of the input is alternately inverted at double the scan frequency. The output d-c signal level resulting from detecting a sine wave of amplitude A is

$$\frac{2}{\pi} A \cos(\theta - \phi) = \text{d-c output}$$

where $\theta - \phi$ is the phase difference between the error signal phase and the phase of the chopping signal. The $(2/\pi)$ factor is necessary to convert the sine wave amplitude to a d-c average voltage level, using this demodulation technique. In one detector, θ is 90 deg out of phase with the other. Thus in one detector an up-down error signal is generated and in the other, a left-right command. For the rest of the analysis only one axis will be considered since the analysis for the other axis is identical. Summarizing the total error detected by combining Eq. (4), the $2/\pi$ factor, load resistance, and d-c preamplifier gain gives:

$$\text{error voltage} = \frac{2W (\text{APW}) (GD) (R_L) (\text{GTPA}) (X_e)}{\pi (\text{DS})} \quad (7)$$

where

GTPA = the gain of the amplifiers and

R_L = the load resistor.

b. Noise Density

The sources of noise considered in this section will be the shot noise and the preamplifier input noise level. It will be shown that, if the dynode gain is high, the preamplifier noise can be dropped from the equation for this system. Shot noise at the photocathode is due to the noticeable variation in a d-c current because it is a flow of discrete particles rather than a continuous flow. The equation is well known and there is no need to derive it for this report.

It is thus

$$I_{rms} = \sqrt{e \, 2\Delta f \text{ (i total average) } (K)} \quad (8)$$

where

$$e = 1.6 \times 10^{-19} \frac{\text{coulomb}}{\text{electron}}$$

Δf = noise bandwidth in Hertz before detection

K = noise factor = 1.5

by adding into this expression the current as derived in Eq. (5), one obtains

$$I_{rms} = \sqrt{\left[\left(W_{BKGD} + \frac{W_i}{2} \right) APW \right] e \, 2\Delta f \, K} \quad (9)$$

At the output of the tube, the noise is multiplied by the gain of the dynodes, hence

$$I_{rms} \text{ (output)} = \left[\left(W_{BKGD} + \frac{W_i}{2} \right) (APW) e \, 2\Delta f \, K \right]^{1/2} GD$$

Like the position error signal at the output of the tube, this noise is amplified by the preamplifier. At this point the shot noise can be compared with the preamplifier noise.

In this system an R_L of 2 k Ω was used. The anode noise levels are presented in the following table for $\Delta f = 10^3$ Hz and $GD = 10^6$, and for typical optical power.

Table 23 . Anode Noise Levels

Neutral Density (Log Transmission)	Optical Power Level (W)	Calculated Anode Shot Noise (μ V)	Preamplifier Noise (μ V)
-4 (-40 dB)	4×10^{-10}	112	0.3
-7 (-70 dB)	4×10^{-13}	3.5	0.3

The preamplifier noise is more than a factor of ten below the shot noise. It can, therefore, safely be said that the system is shot-noise-limited on signal, and the preamplifier noise can be dropped from consideration. The shot noise is amplified and presented to the coherent detectors, with an rms value as follows:

$$V_{\text{rms}} = \sqrt{\left(W_{\text{BKGD}} + \frac{W_{\text{image}}}{2}\right) \text{APW} (e) (2\Delta f) K [(GD) (R_L) (GTPA)]} \quad (10)$$

The coherent detector will do two things to the broadband of noise presented to it. It will double the noise power in the frequency range near d-c and it will detect noise in the frequency regions around the odd harmonics of the chopping frequency which is 20 kHz. The amplitude of the detection is inversely proportional to the harmonic number. The rms amplitude, including the harmonics, must be corrected by the following factor:

$$\text{Correction to rms noise} = \sqrt{1 + \left(\frac{1}{3}\right)^2 + \left(\frac{1}{5}\right)^2 + \left(\frac{1}{7}\right)^2 + \text{etc.}}$$

Considering that the preamplifier bandwidth is 100 kHz, the harmonics beyond 5 are additionally attenuated. Working the result of these factors to the 15th harmonic yields

$$\text{Correction to rms noise} = \sqrt{1.178}$$

Add this factor to the power doubling and the total increase in noise due to the coherent detector is by a factor $\sqrt{1.178 \times 2}$.

The total rms noise voltage after detection becomes,

$$V_{\text{rms}} = 2(GD) (R_L) (GTPA) \sqrt{\left(W_{\text{BKGD}} + \frac{W_i}{2}\right) \text{APW} (e) (\Delta f) K (1.178)} \quad (11)$$

c. Tracking Control Loop Response

The error voltage and noise voltage in the tracking loop have been described. This section will consider the tracking accuracy and also the loops response to the noise input. The tracking loop block diagram is shown in Figure 52.

The sum of error voltages and noise is fed to an rc low-pass filter. It has a 1-Hz corner frequency, and can therefore, act as an integrator in the frequency range being considered. Following this integrator are an amplifier, a current driver, and a deflection coil. The cathode of the image dissector is the summing point in the loop. As the optical image moves on the face of the tube, the scan will no longer be centered on the image. The amplified and detected error voltage will drive a current in the coil to deflect the scan so that it will decrease the error, again becoming centered on the image.

The most useful output of the loop is an indication of the position of the optical image. Since the scan is deflected to follow the image, the image position can be measured by monitoring the coil deflection current. A resistor R_s placed in series with the coil, will generate the desired position measurement. The accuracy of the tracking loop, will first be calculated with the image position as input I and the center of the scan position as the output O .

$$\frac{GD}{1 + GH} = \frac{O}{I} = \frac{(\text{Error det}) (GC) (GT) (C)/(1 + ST)}{1 + (\text{Error det}) (GT) (GC) (C)/(1 + ST)}$$

where

G defines characteristics of the forward loop

H defines characteristics of the feedback loop

GT = tracking amplifier gain

GC = current driver gain

C = coil deflection sensitivity

ST = RC time constant of the simple lowpass filter

S = radian frequency

GDC = $(\text{Error det}) (GT) (GC) (C)$

Error det = result of Eq. 7

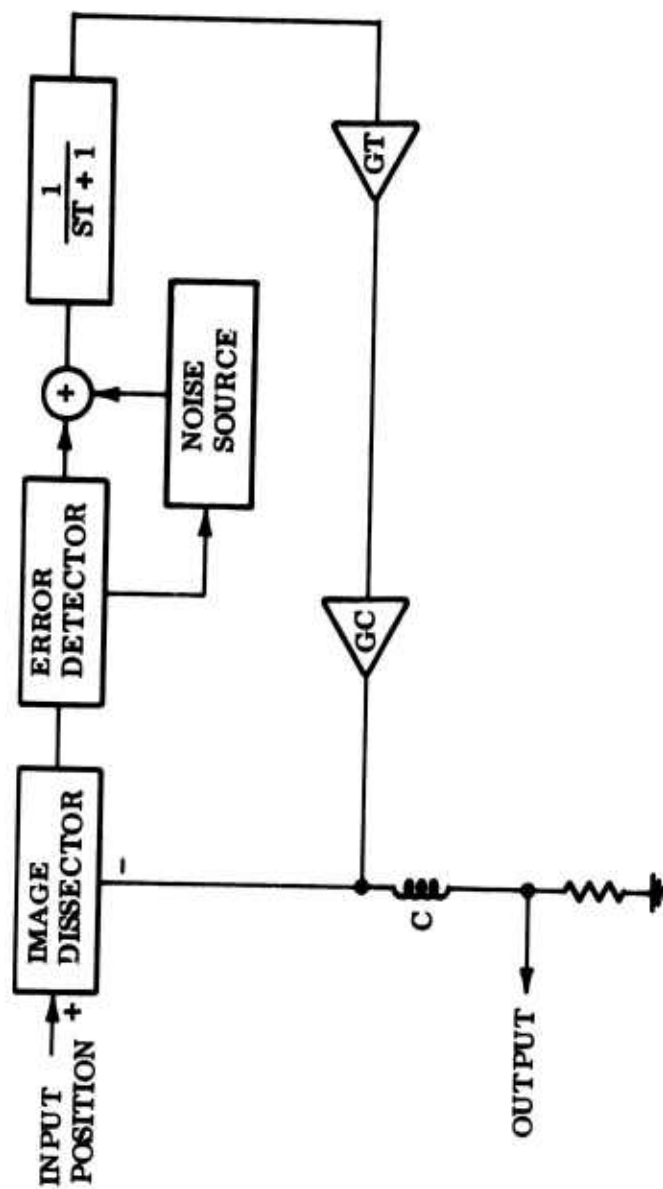


Figure 52 Tracking Loop Block Diagram

Continuing,

$$\frac{O}{I} = \frac{(GDC)}{ST + 1 + GDC} \quad (12)$$

$$\frac{O}{I} = \left(\frac{GDC}{GDC + 1} \right) \left(\frac{(GDC + 1)/T}{S + (GDC + 1)/T} \right)$$

The form of Eq. (12) is a standard form of a low pass filter. At frequencies below $(GDC + 1)/T$, the output of the loop is

$$\frac{O}{I} = \frac{GDC}{(GDC + 1)} \frac{(GDC + 1)/T}{(GDC + 1)/T} = \frac{GDC}{GDC + 1} \approx 1$$

The corner frequency of the loop is the frequency at which

$$S = \frac{(GDC + 1)}{T} = (TTR)^{-1}$$

where TTR is the dynamic time constant of the tracker. Due to overall system requirements, the GDC has been adjusted to result in a bandwidth of 1 kHz.

Using standard servo loop concepts, the position accuracy is equal to the position of the image, divided by the gain in the loop, at direct current. Likewise, the tracking error of an image that is moving at a velocity V_s is equal to the velocity divided by the bandwidth. Therefore, the position error PE due to the image being positioned away from the center by a distance P_i is as follows:

$$\frac{O}{I} = \frac{O}{P_i} = \left(\frac{GDC}{GDC + 1} \right) \left(\frac{(GDC + 1)}{(GDC + 1)} \right)$$

or

$$PE = P_i - O$$

$$PE = P_i - P_i \left(\frac{GDC}{(GDC + 1)} \right) = \frac{P_i}{GDC + 1} \quad (13)$$

In this application, the image will be very close to the central position. Therefore, the position error will be small. The velocity of the image O , V_i , will cause an error in the tracking of

$$VE = V_i (TTR) \quad (14)$$

where

TTR = tracker time constant = 1/bandwidth in radians

The response of the tracking loop to movement of the optical image has now been calibrated. It remains to calculate the effects of noise in the system, and the apparent movement of the image due to noise. Using servo loop analysis, the output O is due to a noise input I .

Thus:

$$\left(\frac{O}{I}\right)_{\text{noise}} = \frac{G}{1+GH} = \frac{(1/ST+1)(GT)(GC)(C)}{1+(1/ST+1)(GDC)}$$

or

$$\frac{O}{I} = \frac{(GT)(GC)(C)}{ST+1+(GDC)}$$

multiplying by T/T gives

$$\frac{O}{I} = \frac{(GT)(GC)(C)/T}{\frac{S+1+GDC}{T}}$$

But, since $\frac{GDC}{\text{error det}} = (GT)(GC)C$, substitution gives

$$\frac{O}{I} = \frac{((GDC)/\text{error det})/T}{S + \frac{1+GDC}{T}}$$

This can then be rearranged to produce

$$\frac{O}{I} = \frac{GDC/\text{error det}}{GDC+1} \times \frac{(GDC+1)/T}{S + (1+GDC)/T} \quad (15)$$

This transfer function is characterized by an amplifier followed by a lowpass filter with a corner at the chosen bandwidth $[(GDC+1)/T]$ of the tracking system. The output, due to a noise voltage input is

$$O_{\text{noise}} \approx \left[1/(\text{error det})\right] \times [\text{Noise voltage}] \times \frac{(GDC+1)/T}{S + (GDC+1)/T} \quad (16)$$

In Eq. (11), the noise rms voltage could not be calculated because the system bandwidth was not known. At this time, however, it is known that the bandwidth is $(GDC+1)/T$. The bandwidth needed, however, is the noise bandwidth; that is, it

implies a transfer function of unity gain up to the bandwidth frequency and infinite attenuation beyond that frequency. The circuit has unity gain to the bandwidth frequency (3-dB point) and drops at 6 dB/octave beyond that frequency. The correction for the system is to multiply the 3-dB-bandwidth by 1.571. Combining these factors, the rms apparent movement of the image is as follows:

$$P_{rms} = \frac{1 \text{ (Noise density)} \sqrt{BW(1.571)}}{(\text{error det})} \quad (17)$$

where

P_{rms} = apparent rms movement of the electron image

BW = 3-dB base bandwidth - $\frac{GDC + 1}{2\pi T}$ hertz

Combining equations (11), (12), and (17)

$$P_{rms} = \frac{\pi (DS) (2) (GD) (R_L) (GTPA)}{(W_i) (APW) (GD) (R_L) (GTPA) (2)} \times \quad (18)$$

$$\sqrt{W_{BKGD} + \frac{W_i}{2} (APW)(e)(K)(1.178)(BW)(1.571)}$$

Simplifying this equation gives

$$P_{rms} = \pi (DS) \sqrt{\frac{W_{BKGD} + W_i/2 \sqrt{BW} (6.66 \times 10^{-10})}{W_i^2 (APW)}} \quad (19)$$

The noise equivalent angle in space is simply

$$NEA = \frac{P_{rms}}{f}$$

Where f is the focal length of the optical system.

d. AGC and Aperture Size Corrections

This first cut at analyzing the tracking loop is now completed. For a final result, it is necessary to include two more factors:

- The effects of the AGC circuit incorporated within the tracker preamp.
- The effect of the aperture size on tracking performance.

In Eq. (19), the bandwidth term can be expanded to include the effect of the AGC circuit. The BW is given by

$$BW = \frac{GDC+1}{2\pi T} \approx \frac{GDC}{2\pi T}$$

Substituting for GDC from Eq. (7) and its definition results in

$$BW = \frac{1}{2\pi T} \frac{(GT) (GC) (C) (W_i) (APW) (GD) (R_L) (2) (GTPA)}{(\pi DS)} \quad (20)$$

The term in this equation that will be constantly changing is the optical image power, W_i . Because of this, the circuit bandwidth could be constantly changing. To eliminate the problem, a feedback gain control is built into the gain of the total preamplifier GTPA, that the product $(W_i) (GTPA)$ is constant. This is called an AGC loop.

The AGC threshold is the maximum voltage due to the image at the GTPA output if the amplifiers were d-c coupled. Depending on the particular AGC process, the physical voltages may be quite different. Equation (20) however, is affected only by the maximum voltage due to the image, the need for it being held at this effective threshold, and the requirement that it be unaffected by the physical implementation.

The AGC voltage is developed in a manner such that it is proportional to W_i . This voltage may be caused by the d-c current from the tube, or by a distinguishable modulation of the current from the image. This voltage is then monitored at the output of the GTPA amplifier, as shown in Figure 53, and the AGC loop holds the voltage constant at that point. This voltage is the threshold voltage.

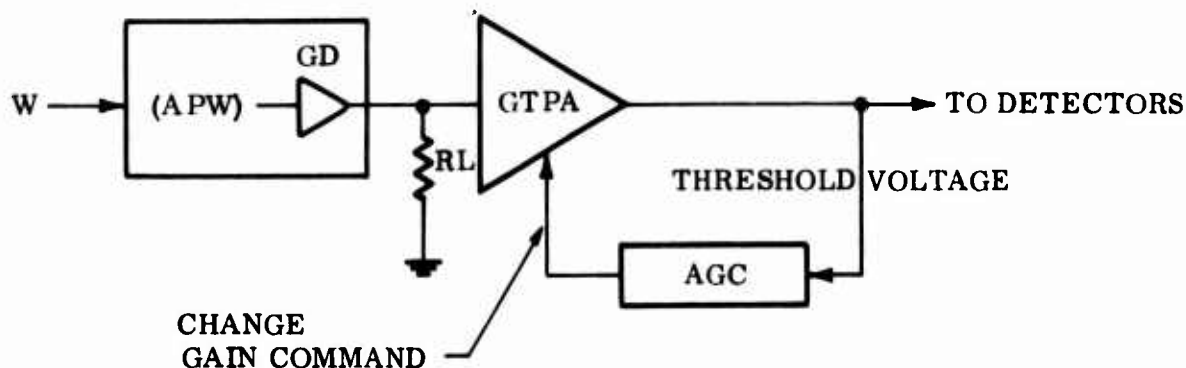


Figure 53. AGC Block Diagram

The equation is:

$$\text{Threshold Voltage} = (W_i)(APW)(GD)(R_L)(GTPA)$$

or

$$GTPA = \frac{(\text{AGC Threshold})}{(W_i)(APW)(GD)(R_L)}$$

Substituting the new expression for GTPA into the bandwidth equation gives

$$BW = \frac{(\text{AGC Threshold})(GT)(GC)(C)}{(T)(\pi^2)(DS)} \quad (21)$$

Having chosen the gains and thresholds such that the bandwidth is the desired value, the system will keep that bandwidth as long as the input power changes are within the dynamic range of the AGC loop. If the power becomes less than that which the loop can correct, the bandwidth will decrease proportionally with the power level - Eq. (20) - with GTPA at its maximum value. Likewise, the bandwidth will increase proportionally if the upper limit of the AGC dynamic range is exceeded - Eq. (20) - with GTPA at its minimum value. Within the range of the loop however, P_{rms} is

$$P_{rms} = (6.66 \times 10^{-10}) \left[\left(\frac{W_{BKGD} + W_i/2}{W_i^2 (APW)} \right) \left(\frac{(VAGC)(GT)(GC)(C)(DS)}{(T)} \right) \right]^{1/2} \quad (22)$$

where VAGC is the AGC threshold voltage.

Outside the range of the loop, the apparent movement of the image is

$$P_{rms} = 6.66 \times 10^{-10} \left[\left(\frac{W_{BKGD} + W_i/2}{W_i} \right) \left(\frac{(DS)(GD)(R_L)(GTPA)(GT)(GC)(C)}{T} \right) \right]^{1/2} \quad (23)$$

with

GTPA = maximum, below dynamic range

GTPA = minimum, above dynamic range

and where

P_{rms} Rms apparent movement of image on the photocathode

W_{BKGD} = Background light power passing through the color filter and through the scanning aperture

W_i = Light power in image of object being tracked

DS = Linear dimension of electron image of object

Before leaving the subject of the AGC, there are two aspects that deserve consideration. First, consider allowing the background current to also activate the AGC. In the present system, the P_{rms} is proportional to the square root of the background power level. By allowing background power to reduce the GTPA, in addition to the image power, the P_{rms} can be made partially or completely independent of the background power. Going through the equations quickly,

$$\left((K) (W_{BKGD}) + W_i \right) (GTPA) = \text{const.}$$

The bandwidth becomes

$$BW \propto \frac{W_i}{W_i + K (W_{BKGD})}$$

and

$$P_{rms} \propto \left[\frac{2 (W_{BKGD}) + W_i}{K (W_{BKGD}) + W_i} \right]^{1/2} \left[\frac{1}{W_i (APW)} \right]^{1/2}$$

where K is the factor that can be varied.

If $K = 2$, P_{rms} is independent of W_{BKGD} . The price one pays is that the bandwidth is decreased, by the factor $K (W_{BKGD})$.

$$BW \propto \frac{W_i}{W_i + K (W_{BKGD})}$$

If the tracker is tracking an image through a scintillating path, the velocity error VE of an image moving with velocity Vi from angular scintillation will increase by

$$VE = Vi/2\pi BW$$

Therefore, the total error of the tracking depends on the amount of angular scintillation, the image power, the background power, and the K factor chosen. The interrelationships depend on a thorough analysis of the complete environment of the tracker and are beyond the scope of this analysis.

Figure 54 and 55 show the typical relationship among these factors. Figure 54 shows the relationship between noise rms movement and background power level, at a fixed value of image power.

Similarly, the velocity error for a moving, or scintillating, target will be higher as the bandwidth is decreased. At a certain value of scintillation and W_i , we get the curves shown in Figure 55.

The total error is the square-root of the sum of the squares of these (random) velocity and noise errors. When there is a good model for the frequency versus amplitude response, and where assumptions can be made about the W_i and W_{BKGP} levels, the value of K can be chosen to minimize the pointing error at those operating points.

The second question to be considered, before leaving the AGC section, has to do with the particular level of the AGC threshold. Disregarding background for the moment, one can see from looking at Eq. (23), which is P_{rms} outside the AGC range,

$$P_{rms} = 6.66 \times 10^{-10} \left[\left(\frac{1}{2} \right) \frac{(DS) (GD) ({}^R L) (GTPA) (GT) (GC) (C)}{T} \right]^{1/2}$$

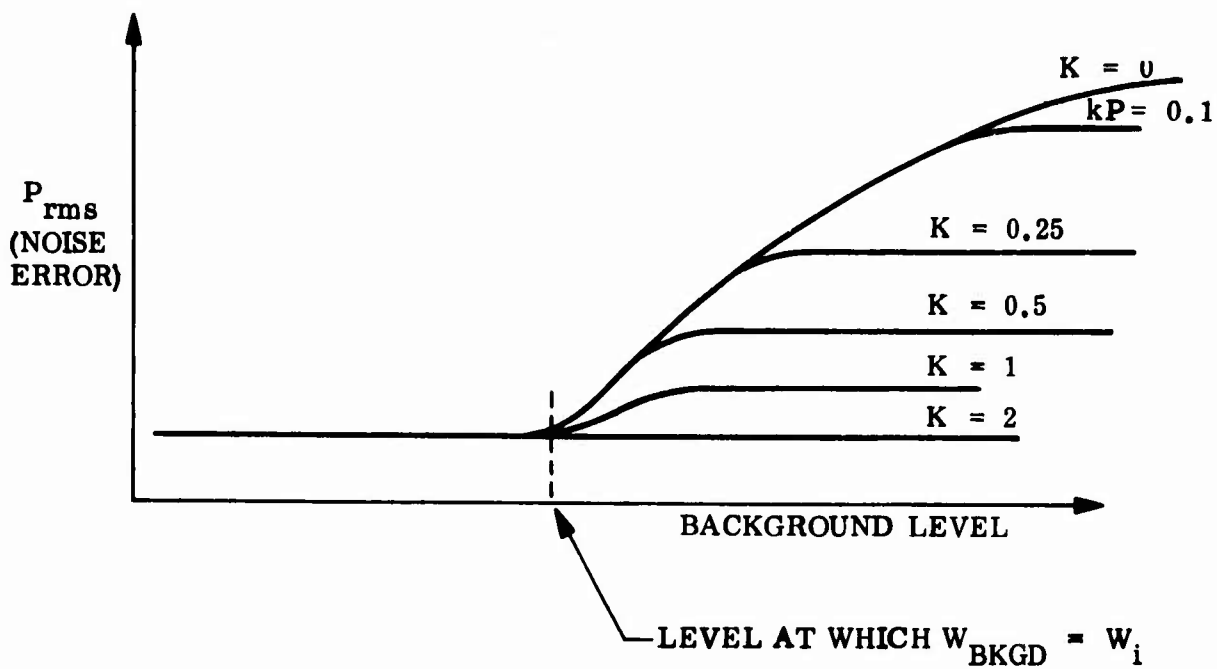


Figure 54 Noise Error as a Function of Background Power

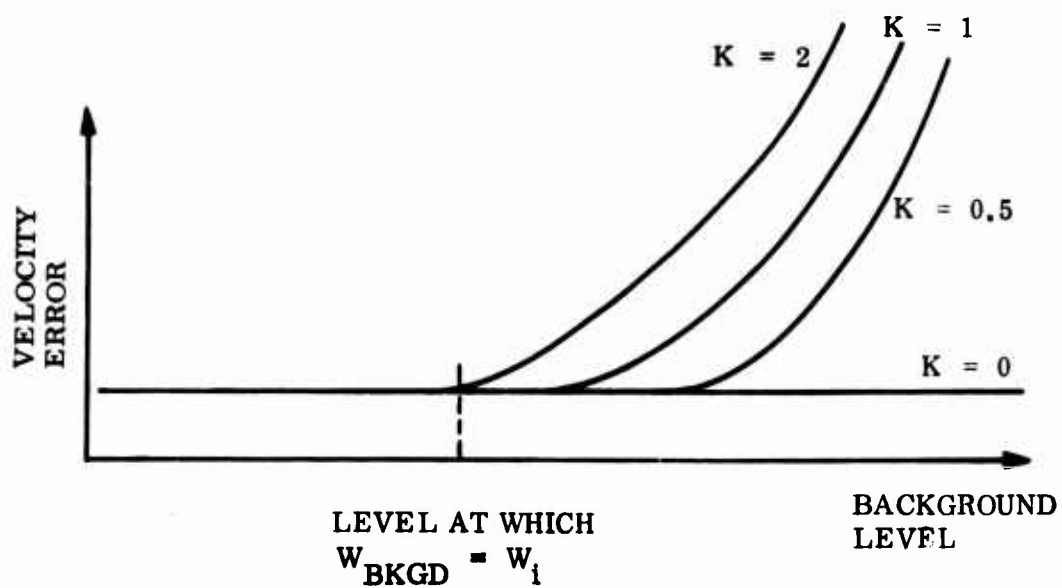


Figure 55 Velocity Error as a Function of Background Power

Thus the noise angle is independent of input power, and depends only on the gain of GTPA maximum. Since $(W_i) \times (GTPA)$ is directly related to the threshold level, it can be said that the P_{rms} depends on the W_i power level at which the AGC begins to control the gain of (GTPA), and the system bandwidth is held constant, i.e., 1 kHz. A graph of P_{rms} versus W_i illustrates the point in Figure 56. Velocity error as a function of W_i is shown in Figure 57.

Depending on the design of the system, the W_i that exceeds the AGC threshold can have various values. The P_{rms} for signals below any particular W_i threshold is constant.

The price one pays for having a high level of W_i threshold is that the system is operating at a reduced bandwidth for optical powers less than that level.

The total error is the square-root of the sum of the squares of these (random) errors. As before, the tradeoff cannot be completed for our system until a reliable frequency versus amplitude model for scintillation can give numbers to be calculated and compared. The W_i threshold for the system was set at $2.0 \times 10^{-13} W$.

e. Tracking Efficiency

In the analysis, up to Eq. (19), it was assumed that the scanning aperture is much bigger than the image size. There is good reason, however, for not designing a tracker with such parameters. It is true that the received background power is proportional to the area of the aperture, and that, by reducing the size of the aperture, this noise level can be reduced. However, as the aperture size is reduced, the tracking ability can be impaired. For example, the percentage of the image power is reduced by an excessively small aperture, and P_{rms} is increased. There is also a possibility that the tracking mechanism is less efficient with very small apertures. To evaluate the nature of the tradeoffs in this question, a gaussian-shaped spot and an aperture were modeled on a computer, and the effects on P_{rms} were calculated. The gaussian spot had the same half-power width, DS, as the Bessel function that describes the diffraction image, which was converted to an electron image at the aperture.

The calculation first described the image as two-dimensional with an intensity that varied in a gaussian manner as the distance from the center increased. An aperture was described, and through the Law of Cosines, it could be positioned at any radial distance from the center. To integrate the total intensity within the aperture, the computer calculated the intensity at each small segment of the aperture and then summed these values.

The increments that made up the aperture were one-tenth of the deviation of the gaussian distribution. These values of intensity through an aperture were subtracted from the

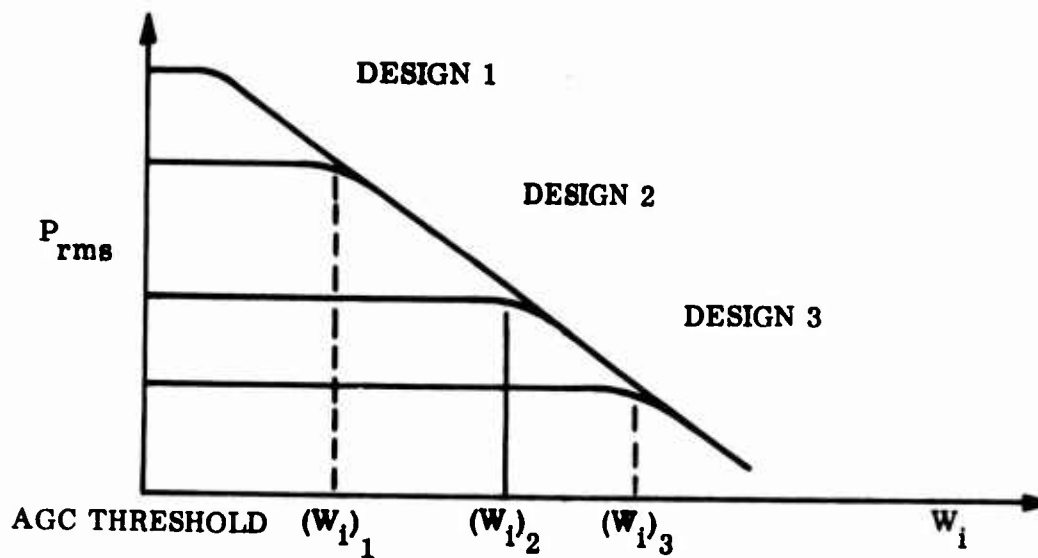


Figure 56 Noise Error as a Function of AGC Threshold

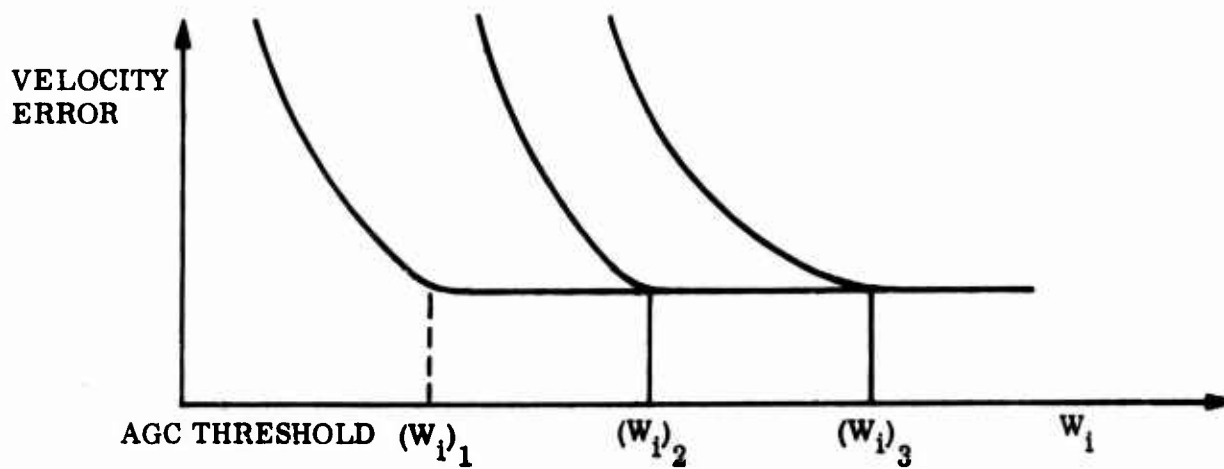


Figure 57 Velocity Error as a Function of AGC Threshold

intensity for an aperture that was displaced radially, by an amount of exactly one aperture diameter. This subtraction of aperture pairs was continued for all positions of the pair with respect to the image center.

A plot of these values versus position is the plot of the error detector output as a function of position. The family of curves is shown in Figure 58. The slope of this error detector curve acts like a correction of the d-c error volt/error as shown in Eq. (7). A plot of the computed function (the correction factor) is shown in Figure 59.

On receiving the curves from the computer, the question arises as to what is happening physically to the system to cause these curves. Therefore, a simple model was sought that would produce curves that match those generated by the computer. The closest match came from a calculation of the maximum intensity of an image that can pass through an aperture of the various sizes.

This match means that the major effect on tracking a Gaussian image is the reduction of the optical power as the aperture size is reduced. This physical model makes it much easier to modify the equations of the system. Every place where the optical power W_i appears, it should be replaced by

$$(\text{Correction factor}) \times W_i$$

(1) Background. The particular value of the ratio that one should use, depends on the effect of the aperture size on the background light level. This analysis assumes that other overall system considerations determine the optical system design, i.e., f-number and objective lens size. The background light will illuminate the photocathode surface of the tube. The amount of electron current that passes through the aperture then depends only on the area of the aperture. On the basis of these considerations the effects on P_{rms} can be calculated. Rewriting Eq. (22),

$$P_{rms} = (\text{const.}) \left(\frac{W_{BKGD} + W_i/2}{W_i^2} \right)^{1/2}$$

shows the relationship between W_{BKGD} and W_i . Figure 60 presents a family of curves showing the following:

- Vertical Axis – Log of the power terms in P_{rms} equation, with $\log = 0$ for the situation of larger aperture with no background.
- Horizontal Log of Aperture-Size/DS Ratio.
- Family of Curves for Background Power Level Indication – Ratio of curves for $W_{BKGD}/(W_i/2)$, when $DS = \text{Aperture}$, i.e., if ratio = 10 and with an aperture size equal to DS, there is 10 times as much current due to background as due to the half-image power.

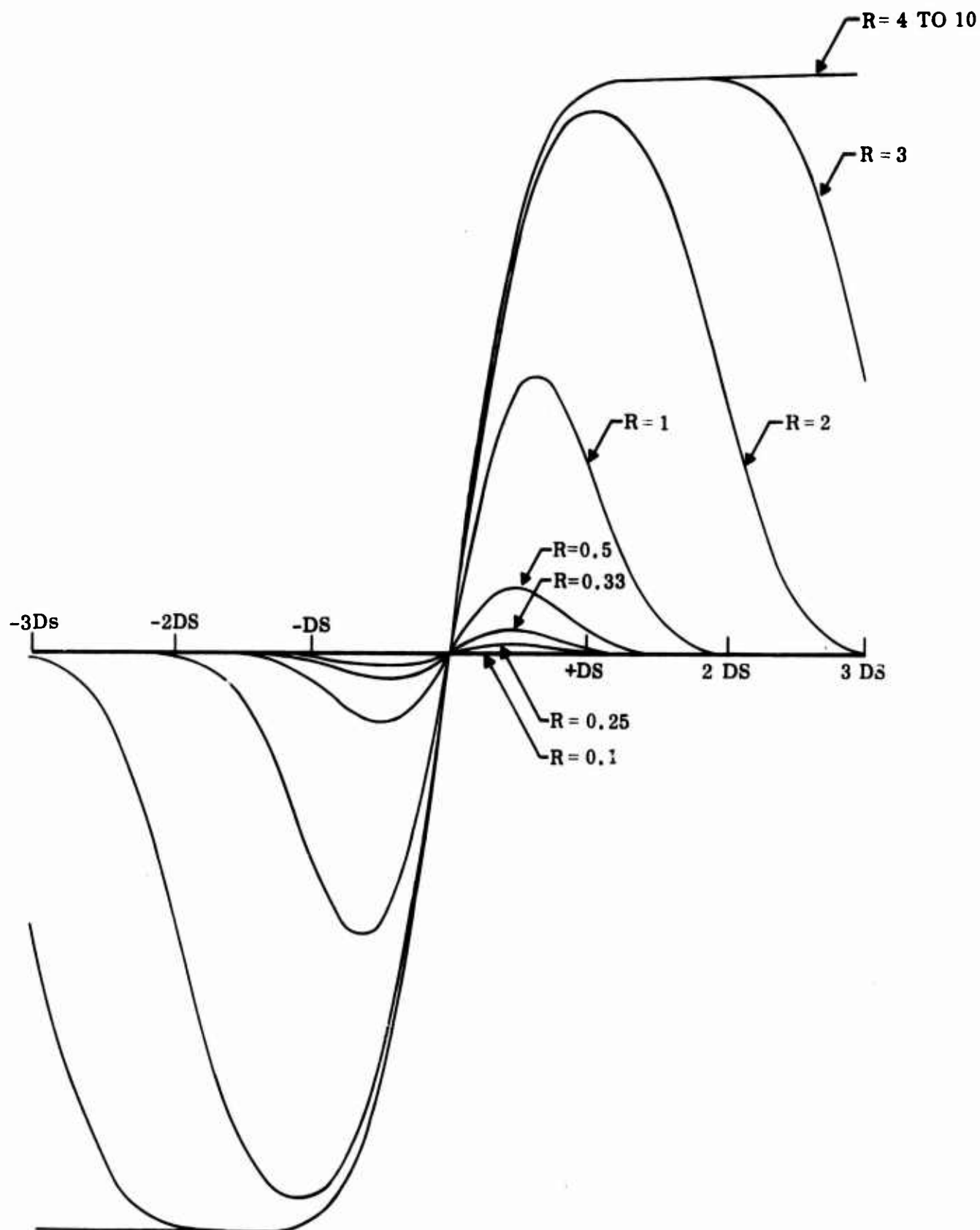


Figure 58 Error Signal as a Function of Position Error

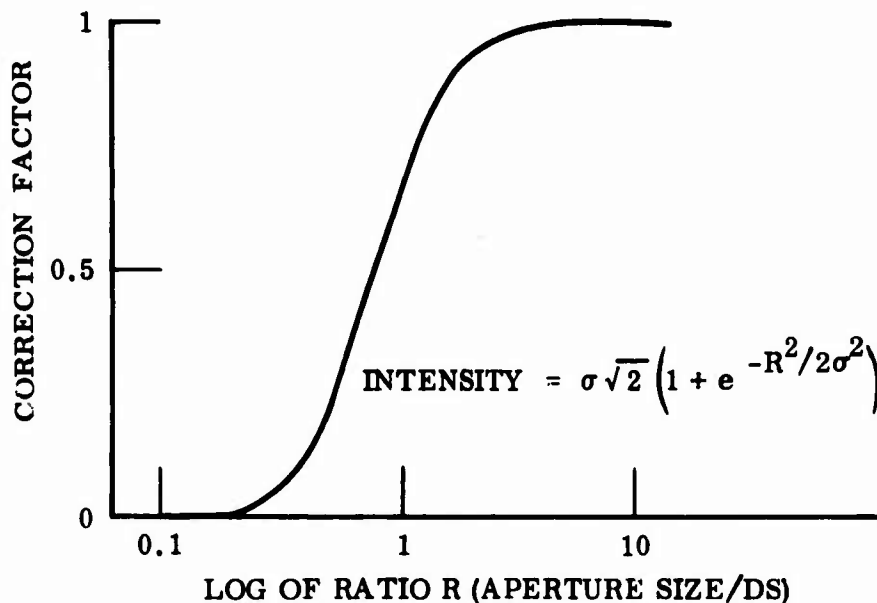


Figure 59 Correction Factor for Received Optical Power

The curves are the solution to the equation

$$P_{\text{rms}} = \sqrt{\frac{(\text{BKGD density}) (\pi R^2) + K W_i/2}{\text{computed error detector slope}}}$$

where

R = aperture radius

$K W_i/2$ = image power as a function of aperture size

Computed error detector slope is as shown in Figure 58 and almost equals $K W_i$.

The curves in Figure 60 show that, if the aperture is very small, the noise, P_{rms} , is high. This is because the tracker has trouble even detecting the image. If the aperture is too large, the background light can swamp the image current causing noise. However, one can see from these curves that, if one chooses an aperture equal to DS (the electronic spot size) under high background conditions the increase in noise is at a minimum and at low background levels P_{rms} is increased only by a factor of $\sqrt{2}$.

Summarizing this section, at an image-diameter-to-aperture-diameter-ratio of 1, the effects of background light can be greatly reduced with little effect on the system performance. If the background levels are still too high for proper tracking, one can resort to the techniques discussed in the AGC section.

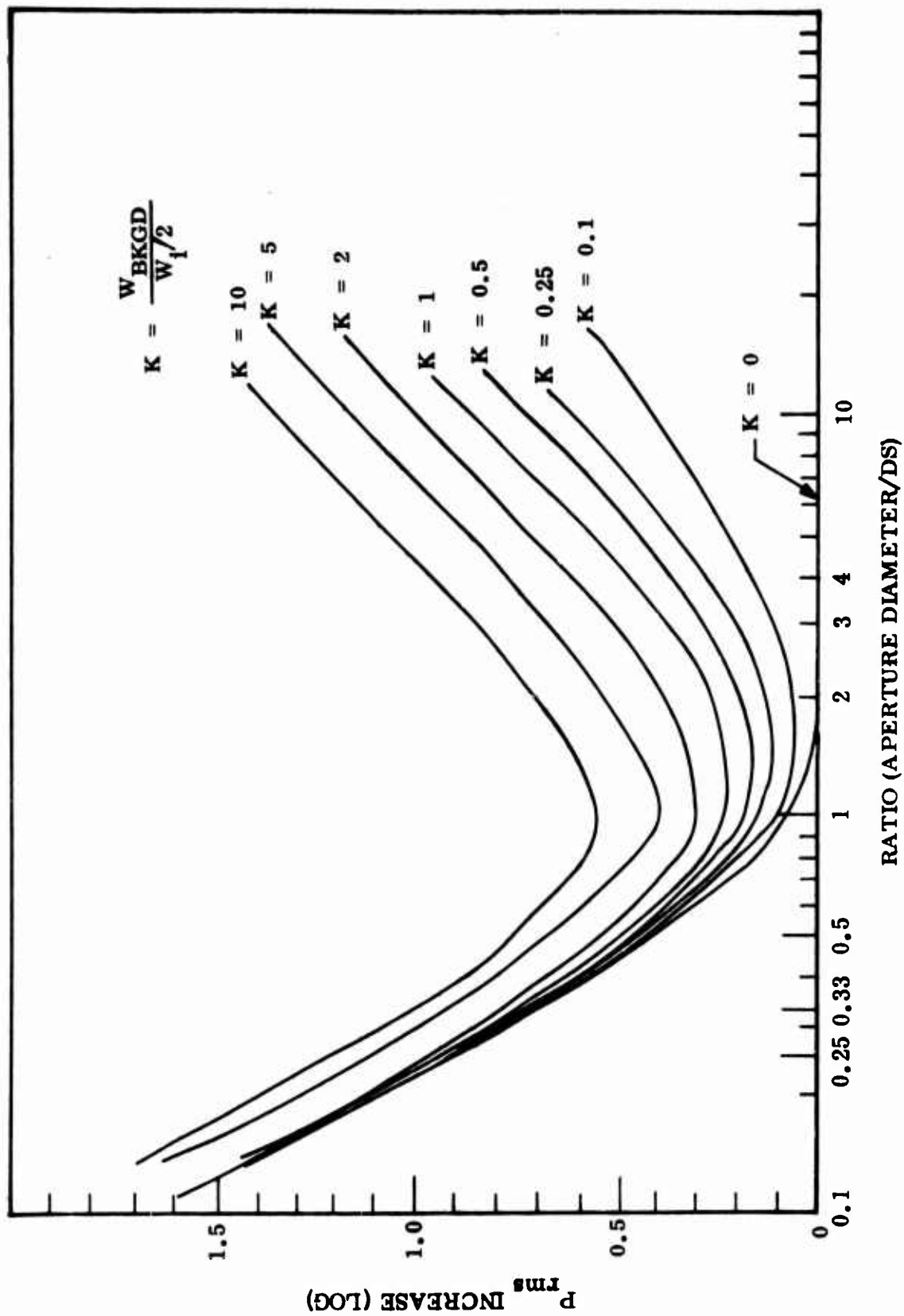


Figure 60 Relative P_{rms} Versus Ratio at Various Background Light Illumination Levels

3. BEAM STEERING SYSTEM PERFORMANCE AND NOISE

a. System Performance

The previous section discussed the tracker, which has an output voltage proportional to the distance of the image from a central point on the tube face. The task of the beam steering system is to rotate mirrors in the optical path until the image is centered exactly at the electrical center of the tube. It is unimportant where this electrical center is physically on the tube; it is important only that it does not move. Once the optical system is adjusted on the basis of this point, the function of the beam steering system is to keep the beacon laser's image centered on it.

A simplified block diagram is shown in Figure 61.

The tracker is the tracker of the previous section with an active filter and amplifier and with a lens. The total transfer function for this combination is 3,000 V/radian of shaft rotation, or 17,000 V/radian of space angular movement. Under normal conditions its frequency response is flat up to 1 kHz, 6 dB/octave to 4 kHz, and 30 dB/octave above that.

The first goal is to calculate and evaluate the transfer function of the total loop. The response of the mirror to a movement of the incoming image, for the simplified block diagram, is shown in Figure 61 with inputs and outputs indicated.

For the loop A, B, D, the transfer for an input, I_1 , to the output, O, is

$$\frac{O}{I_1} = \frac{G}{1 + GH} + \frac{A}{1 + ABD}$$

where

- G = generalized expression for the gain and frequency response of the forward part of a servo loop
- H = generalized expression for the gain and frequency response of the feedback part of a servo loop

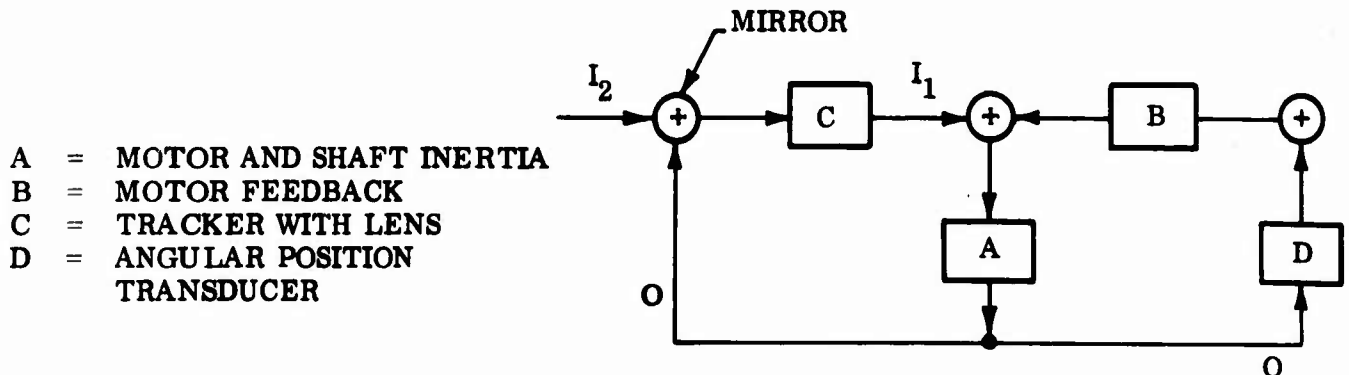


Figure 61. Beam Steerer Loop

Using this expression for the loop, we can solve for the outer, or total, loop:

$$\frac{O}{I_2} = \frac{C (O/I_1)}{1 + C (O/I_1)} = \frac{C}{(I_1/O) + C}$$

$$\frac{O}{I_2} = \frac{AC}{1 + ABD + AC} \quad (24)$$

The characteristics of the total loop can be described as follows (the operation has three regions):

Region Number	Gain Situation	Loop Frequency Response
1	$AC \gg ABD > 1$	Flat, unity gain
3-dB point	$ABD = CA > 1$	3-dB frequency point
2	$ABD \gg AC \text{ and } 1$	$1/S = 6 \text{ dB/octave};$ $C/BD = \text{gain}$
3	$1 \gg CA \text{ and } ABD$	$1/S^2 = 12 \text{ dB/octave},$ $CA = \text{gain}$

A Bode plot of the terms AC and ABD show the regions. First the components - AC and ABD - are presented (Figure 62), and then the total loop frequency response (Figure 63). A more detailed block diagram of the complete tracking loops is shown in Figure 64.

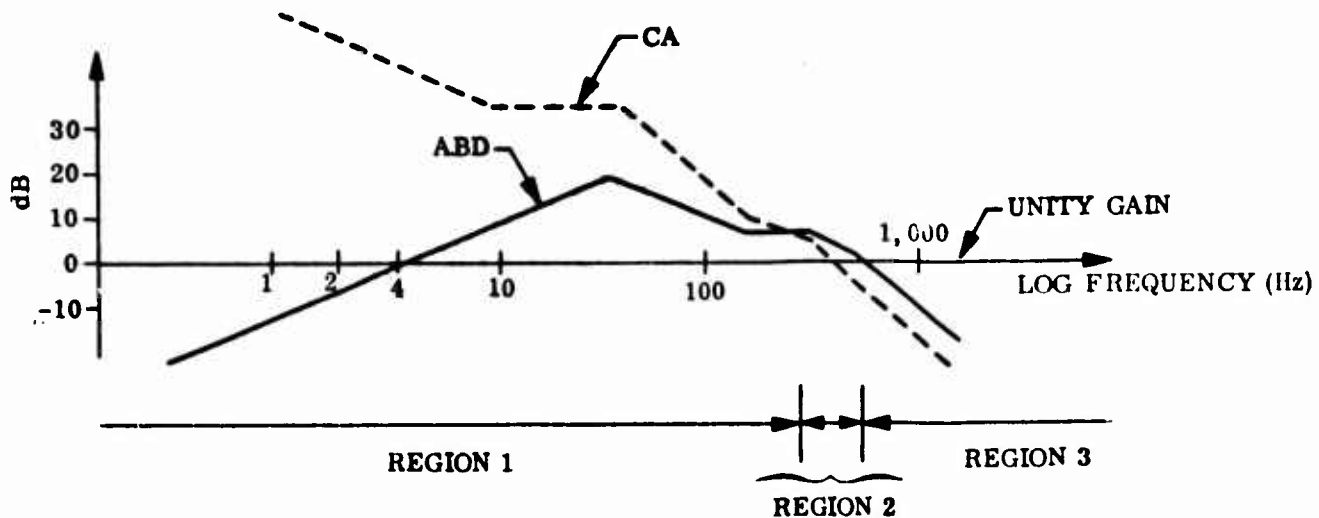


Figure 62 Bode Plot of Steering Loop

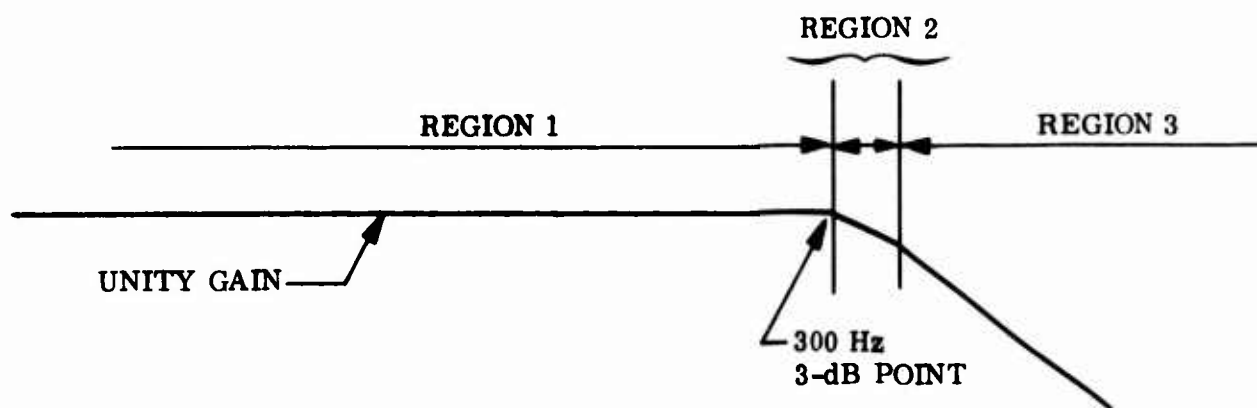


Figure 63 Steering Loop Response

Consider the beam steering loop by itself. From the curve of ABD in Figure 62, it can be seen that the beam steerer loop has unity gain or greater between 4 Hz and 500 Hz. Because of this, the overall transfer characteristic for the loop is determined by $1/BD$, as shown in Figure 65. The shape is $1/S$, including K_{H1} . The simplicity of this shape makes the overall tracker loop easy to implement.

At this point, some important interrelationship, of the overall tracking system parameters can be seen. First, the bandwidth of the overall system is determined by the point where $ABD = CA$. Therefore, if we have a bandwidth specification, the ratio of C/BD cannot change. Second, the region of reasonable and stable performance of the beam steering loop is determined by ABD. If the system is to be stable, ABD must equal 1 at a frequency above the BW specification. The minimum phase margin determines how high this frequency must be.

b. Noise

The next question is, what happens to the mirror shaft as a result of noise at the transducer. (The transducer is believed to be the largest source of noise outside the tracker, other than atmospheric or shot noise.)

The most correct way to model the position transducer is to show a pick-off or detector (D) and then a demodulator and amplifier (K_D). The noise is shown summing with the pick-off. This model shows clearly that, if one wants a less noisy transducer system with the same overall gain, one must find a detector that is inherently more sensitive in V/radian so that the gain, K_D , can be reduced. The noise coming out of K_D will, therefore, be less. The price for increased sensitivity, however, is a reduced dynamic range.

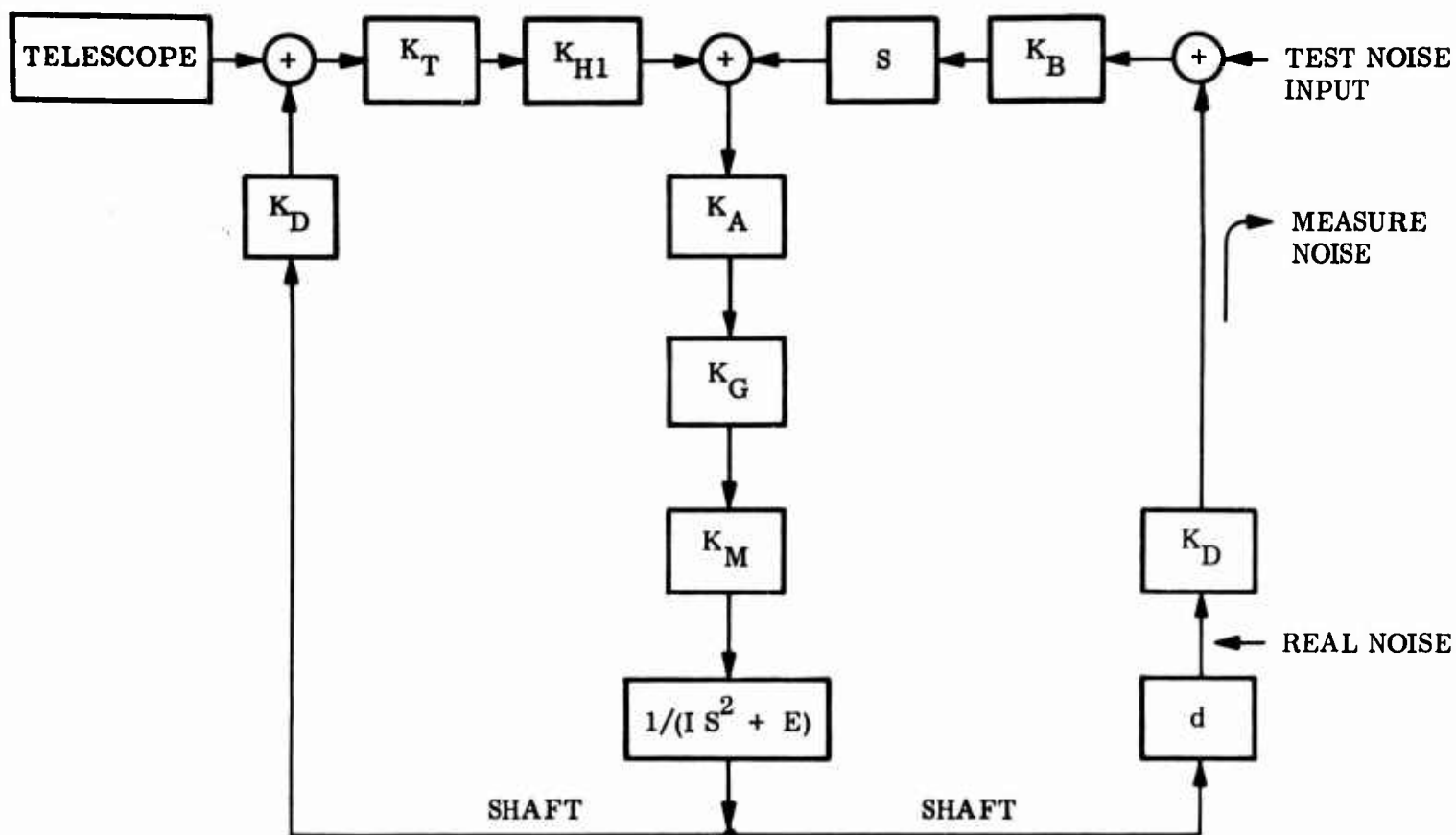
Assuming that one can not eliminate noise coming out, we must find the transfer function for a signal at that point, i.e., summed with the output of K_D (see Figure 64). Using the same technique as used before and starting from I_1 , in Figure 66,

$$\frac{O}{I_1} = A/(1 + AC)$$

Now, the total loop is shown by

$$\frac{O}{I_2} = \frac{B(I_1/O)}{1 + BD/I_1/O} = \frac{B}{O/I_1 + BD}$$

$$\frac{O}{I_2} = \frac{B}{\frac{1 + AC}{A} + BD} = \boxed{\frac{AB}{1 + AC + ABD}} \quad (2)$$



TEST NOISE
INPUT

MEASURE
NOISE

REAL NOISE

LEGEND

D	d	= transducer detector (V/radian)
	K_D	= transducer demodulator and amplifier (V/V) $dK_D = 6 \text{ V/radian}$
C	K_O	= optical angular gain of mirror $= 2 \frac{\text{radians of light}}{\text{radian of shaft}}$
	K_T	= tracker gain of image dissector $= \frac{17,000}{11.3} \frac{\text{V}}{\text{radian of light}}$
	$K_T K_O$	$= 3,000 \frac{\text{V}}{\text{radian of shaft}}$
	K_{H1}	= transfer function of low-frequency integrator $= 16.6 \frac{1 + S(0.015)}{1 + S(2.215)} \frac{\text{V}}{\text{V}}$
B	$(S)K_B$	= transfer function of differentiator section $= 7.65 \frac{8.2 \times 10^{-3} (S)}{1 + 3 \times 10^{-4} (S)} \frac{\text{V}}{\text{V}}$
A	K_A	= transfer function of compensator $= 0.515 \frac{1 + S(1.1 \times 10^{-3})}{1 + S(1.0 \times 10^{-4})} \frac{\text{V}}{\text{V}}$
	K_G	= transfer function of filter $= \frac{1}{1 + 5 \times 10^{-4} (S)} \frac{\text{V}}{\text{V}}$
	K_M	= current driver and motor gain $= 1.2 \text{ oz-in. /A} \times 2.33 \text{ A/V}$ $= 2.8 \text{ oz-in. /A}$
	$\frac{1}{IS^2 + E}$	= transfer function for shaft inertia and spring $I = 2.28 \times 10^{-4} \text{ oz-in. sec}^2/\text{Hz}$ $E = 14.7 \text{ oz-in. /radian}$ $\frac{K_M}{IS^2 + E} = \frac{2.8}{14.7 [1.55 \times 10^{-5} (S)^2 + 1]} \frac{\text{radians}}{\text{V}}$

Figure 64 Block Diagram of the Tracking
Loops

2

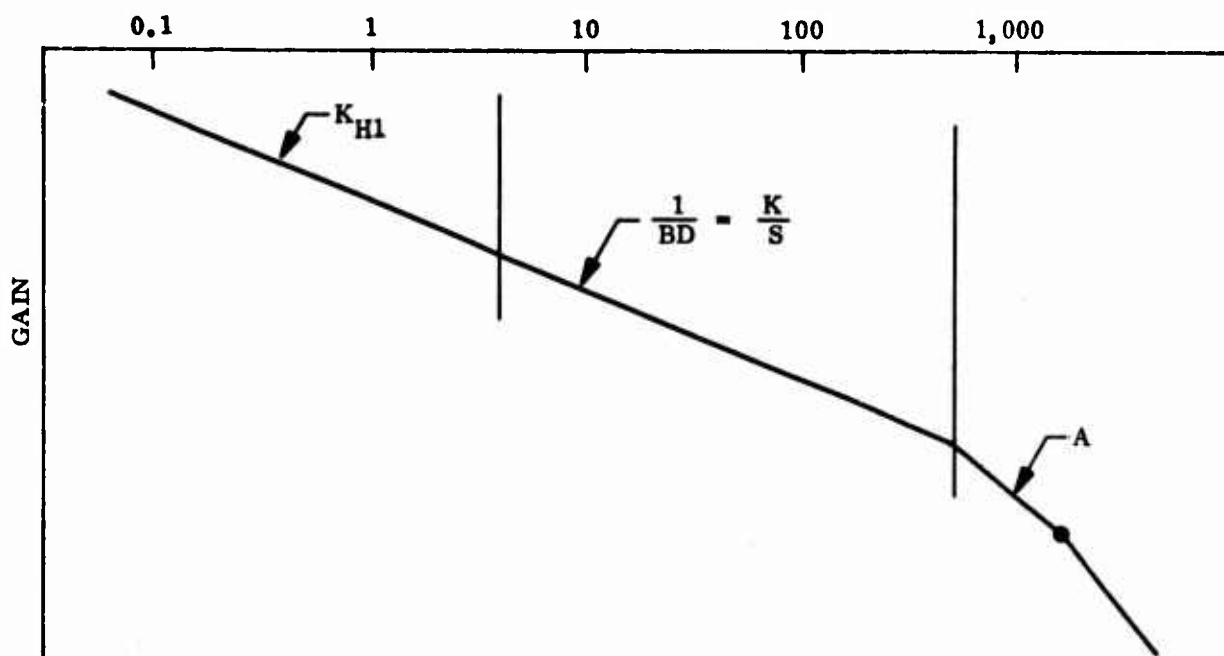


Figure 65 Beam Steerer Response

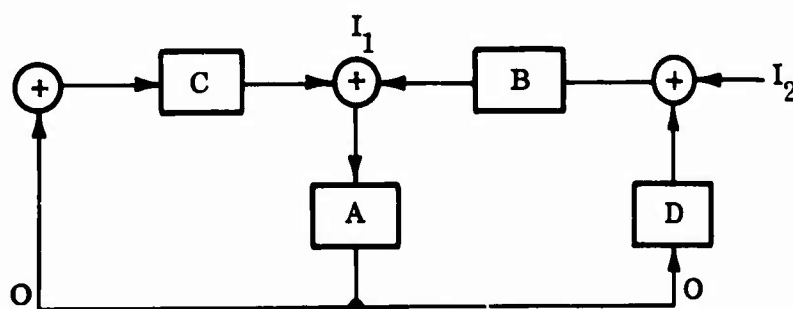


Figure 66 Block Diagram for Transfer Function of O/I_2

PRECEDING PAGE BLANK-NOT FILMED

There are the following regions:

Region 1	AC \gg ABD and 1	\longrightarrow	B/C
Region 2	ABD \gg AC and 1	\longrightarrow	1/D
Region 3	1 \gg AC and ABD	\longrightarrow	AB

Plots are the same as before; however, the transfer function and the regions are quite different. First the components AC and ABD are plotted as shown in Figure 67, and the total loop is as presented in Figure 68. The shape of this function agrees with data. The only difference is that the ABD = 1 point is at 400 Hz, instead of 500 Hz as shown on the graph.

Methods of reducing the noise could be tried, but, the specified overall bandwidth and the requirement of stability are determined by the factors ABD and C/BD, respectively.

Therefore, BD, the common term, must remain constant. To summarize: the requirements of dynamic range, overall bandwidth, and stability determine all parameters and thus the noise response of this system.

The last task is to evaluate how this noise transfer function couples white noise at the input, to the shaft output. The general equation for RMS noise is

$$\text{RMS } \bar{e}^2 = \frac{(kT)}{|H(f_0)|^2} \int_{-\infty}^{\infty} |H(f)|^2 df$$

where

$\frac{(kT)}{|H(f_0)|}$ = The function describing the noise density and amplitude

$|H(f)|^2$ describes the frequency function to be integrated

In our system, the noise will be assumed to be white. From data of the demodulator output, the white noise density is

$$"(kT)" = 1.381 \mu\text{V}/(\text{Hz})^{1/2}$$

The frequency function breaks into the following regions:

	Frequency
DC \longrightarrow 10 Hz	$Gk f^2$
10 \longrightarrow 160 Hz	$Gk f$
160 \longrightarrow 400 Hz	Gk
400 \longrightarrow ∞	$G/k f^2$

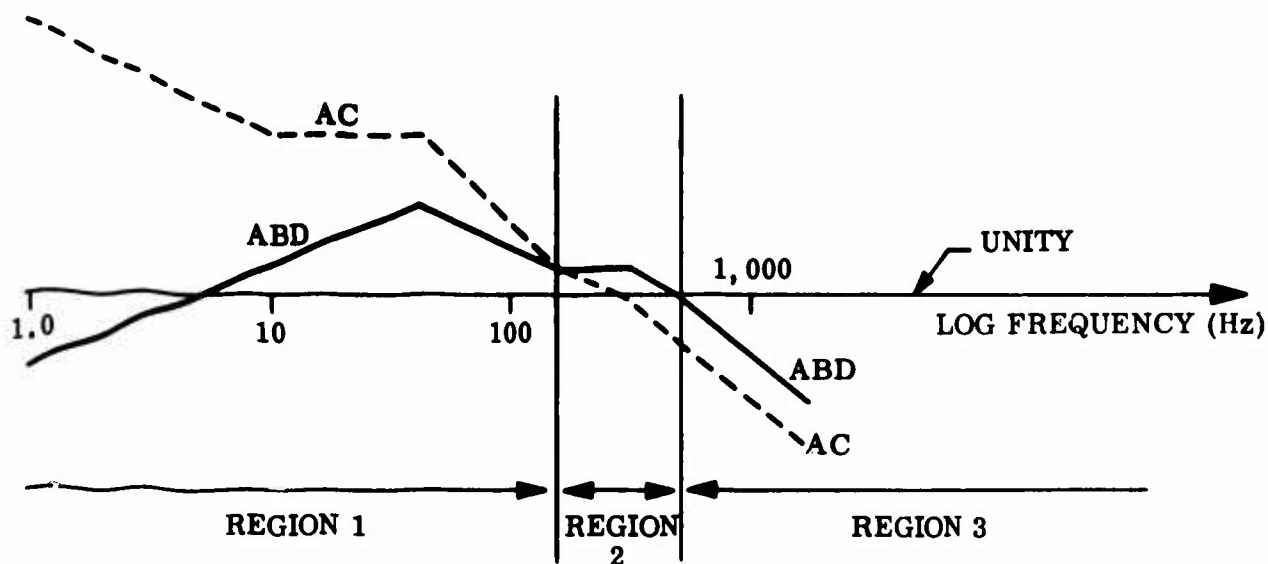


Figure 67 Bode Plot of Transfer Functions of Elements

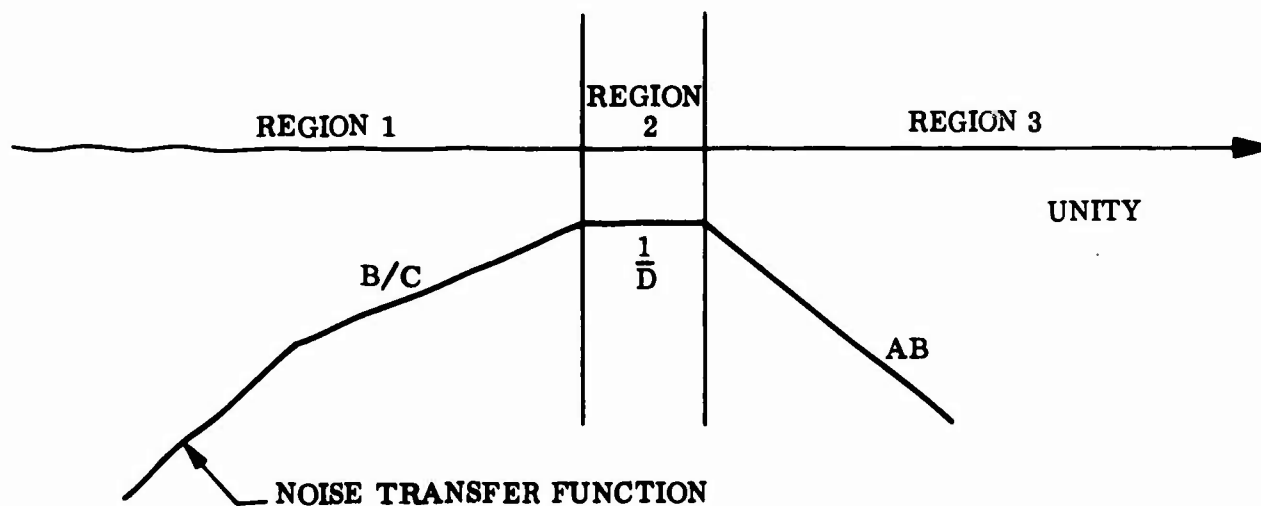


Figure 68 Bode Plot of Transfer Functions of O/I_2

where

G = dc gain level
k = level of transfer function
f = frequency

By doing the various integrals and square-rooting the sum of the squares, one can calculate the RMS noise level.

The total level thus calculated is 4.28 μ radians of RMS noise.

The equivalent noise angle in space due to the shaft noise is

$$\begin{aligned}\text{RMS} &= \frac{\text{mirror gain (noise on mirror)}}{\text{telescope magnification}} \\ &= \frac{4.28(z)}{11.3} = 0.76 \mu\text{radians in space.}\end{aligned}$$

The number agrees very well with the test data taken, which gave 0.7 μ radians in space.

This noise level is higher than can be tolerated in the brassboard system. As this analysis is being written, there are several design techniques that will reduce this noise by at least a factor of 40. A trade-off study will be performed, and the best technique will be incorporated in future systems.

4. SYSTEM ERRORS - MAGNETIC FIELDS

Earlier, Section VII stated that the position of the image on the tube face that is called center is unimportant, but that it must not move once the optical system is aligned on the basis of that position. One thing that can move this center is a variation in the earth's magnetic field with spacecraft motion. For this reason, the deflection coils and the tube assembly are surrounded by magnetic shields.

The shields used in the breadboard were tested to determine the leakage of an external field. Fields were impressed from all angles by rotating a Helmholtz coil around the tracker. At the worst angles, the tracker "center" moved 0.0001 in./Gauss. The change in the earth's magnetic field with spacecraft motion during the acquisition period (before the closed-loop corrections compensate) is several orders of magnitude less than 1 Gauss, so magnetic effects from the earth's field are insignificant.

5. SYSTEM ERRORS - PHOTOCATHODE GRANULARITY AND PHOTOCATHODE AGEING

The image dissector itself can be a source of errors in the system. First, consider the granularity of the photocathode. ITTG has taken data on the apparent magnitude of a star source as it is scanned across the face of the tube. The data reveal that in the

central region of the tube (region with half the radius of the tube face) the maximum changes in sensitivity are 10 percent from the nominal sensitivity.

The effect of this variation appears to be a reduction of overall gain of the system. If the image moves into the region of less sensitivity, its intensity will appear to have been reduced by 10 percent.

The AGC circuit in the system will make the proper adjustment in system gain, and the P_{rms} will increase a slight amount.

Ageing of the photocathode depends on the photoelectron density on the photocathode. According to testing by the tube manufacturer, at the current density from an input power of 6×10^{-10} W of red light, an S-25 surface will lose a factor of two in sensitivity in 75,000 hr of operation. Since the S-20 surface of our tubes is similar, ageing should not effectively change the performance of our system over the time that we will be operating.

REFERENCES

- 1 Lockheed Missiles & Space Company, Laser Communication Preliminary Subsystem Design for the Space Data Relay Subsystem, SAMSO TR 71-252, 19 Nov 1971, Volume II, Section 3
- 2 Ibid, Volume III, Appendix O, pages 43 - 48
- 3 Ibid, Volume III, Appendix O, pages 9 - 22

PRECEDING PAGE BLANK-NOT FILMED

DOCUMENT CONTROL DATA - R & D

(Security classification of title, body of abstract and indexing annotation must be entered when the overall report is classified)

1. ORIGINATING ACTIVITY (Corporate author) Lockheed Missiles & Space Co., Inc. Palo Alto Research Laboratory 3251 Hanover St., Palo Alto, CA 94304		2a. REPORT SECURITY CLASSIFICATION Unclassified	
		2b. GROUP	
3. REPORT TITLE Acquisition and Tracking Performance Evaluation			
4. DESCRIPTIVE NOTES (Type of report and inclusive dates) Final Report			
5. AUTHOR(S) (First name, middle initial, last name) C. E. McClellan, G. R. Chippendale, R. C. Ohlmann R. O. Waddoups, L. G. Horn, G. R. Hostetter			
6. REPORT DATE December 1972		7a. TOTAL NO. OF PAGES 159	7b. NO. OF REFS 3
8a. CONTRACT OR GRANT NO. AF33615-72-C-1941		9a. ORIGINATOR'S REPORT NUMBER(S) LMSC-D313251	
b. PROJECT NO.			
c.		9b. OTHER REPORT NO(S) (Any other numbers that may be assigned this report)	
d.		AFAL-TR-73-21	
10. DISTRIBUTION STATEMENT Distribution is limited to U.S. Government agencies only, by reason of inclusion of test and evaluation data; applied January 1973. Other requests for this document must be referred to AFAL/TEL, Wright-Patterson AFB, Ohio, 45433.			
11. SUPPLEMENTARY NOTES		12. SPONSORING MILITARY ACTIVITY Air Force Systems Command AFAL/TEL WPAFB, Ohio 45433	
13. ABSTRACT Experimental evaluation has been made of tracking and pointing performance of an optical communication system employing a separate laser for each of these functions. The optical beam diameters were scaled down to 7/8 in. from larger diameters which would be employed for an operational space communication system. The tracking system and pointing laser were mounted on an oscillating table in simulation of vehicle limit cycle motion. Measurements were made of the time for the image dissector tracker to acquire a target, the angular range over which this could be accomplished, and the probability of acquisition on each scan with a minimum (0-margin) signal. Measurements were also made of the effects on tracking and pointing accuracy of signal-to-noise ratio, automatic gain control performance, beam diameter, gimbal friction and inertia, servo loop characteristics, accelerations, and atmospheric turbulence. Experimental results confirmed theoretical predictions of performance and demonstrated the feasibility of tracking and pointing laser beams with accuracy suitable for practical communication systems in space.			

UNCLASSIFIED

Security Classification

14 KEY WORDS	LINK A		LINK B		LINK C	
	ROLE	WT	ROLE	WT	ROLE	WT
Acquisition Time						
Atmospheric Turbulence						
Optical Pointing						
Optical Target Acquisition						
Optical Tracker Analysis						
Optical Tracker Design						
Optical Tracking						
Shot-Noise Tracking Error						
Friction Tracking Error						
Acceleration Tracking Error						

UNCLASSIFIED

Security Classification